Nanocrystals for Photocatalysis and Imaging Applications

Part One: Manganese-doped CdS/ZnS Core/shell Quantum Dot Films as Photocatalysts for Organic Reactions

Part Two: Sequence-specific DNA-Gold Nanoparticles as High Mass Probes in Imaging Mass Cytometry

Brian Malile

A Dissertation

submitted to the Faculty of Graduate Studies

in Partial Fulfillment of the Requirements for the Degree of

Doctor of Philosophy

Department of Chemistry

York University

Toronto, Ontario

March 2023

Prologue

The field of nanotechnology is highly interdisciplinary. It is an area where physical sciences, life sciences, medicine, engineering, and biotechnology overlap, creating demand for a cross-functional approach to study nanomaterials and their applications. This versatility requires a range of experimental methods, instrumentation, and collaboration, making it a challenging but an exciting field to study.

The manipulation of materials at the nanoscale gives rise to properties previously not observed in their bulk counterparts. These features arise from size, shape, surface properties and composition enabling novel optoelectronic properties and photocatalytic activity. This versatility has led to the development of many innovative applications, including nanosensors for disease detection, nanoparticle-based drug delivery systems, high-performance energy storage devices, and environmental remediation methods.

This dissertation encompasses two projects which initially seem unrelated but, in many ways, coincide, specifically in the implementation of nanocrystals. One project investigates the photoreduction capabilities of manganese (II) doped cadmium sulfide quantum dots via a heterogeneous approach where doped quantum dots were applied as thin-film coatings of reaction vessels that exhibited superior performance to the commonly studied undoped equivalents. The other project utilized DNA-gold nanoparticle conjugates as high mass probes in Imaging Mass Cytometry, a novel imaging technique for single cell analysis developed by Fluidigm Inc. The industrial collaborative work addressed challenge of detecting low abundant biomarkers, which has been a limitation of imaging mass cytometry. Additionally, it shed light on the sequence specific uptake of DNA-gold nanoparticle conjugates.

Both projects harness the size-dependent properties of nanocrystals. First, in quantum dots, confinement effects alter the electronic structure in a way that favours the escape of electrons, a desirable feature in photocatalytic applications. In gold nanoparticles, the interaction of light with the surface electrons, not only creates an absorption profile that is absent in bulk, but it generates fluorescent quenching capabilities which can be exploited in imaging applications. Second, these optoelectronic properties allow for their study and evaluation in imaging and photocatalytic applications, where changes in the absorption and emission of the nanomaterial can infer information on their operation or degradation. Third, surface modification is an important approach that can tailor the nanomaterials' capabilities. Assembling a shell, which consists of a different semiconductor, on a quantum dot improves its photoluminescence and robustness. DNA functionalization adds a sequence-specific recognition factor to the nanoparticles and increases their colloidal stability. Surface modification terms like core/shell, and DNA functionalization are not only limited to quantum dots and gold nanoparticles but can be applied to nanomaterials of various sizes shapes and compositions and are a key aspect in this field. Although this work studies the implementation of nanocrystals in two distinct areas, the factors described above show the common ground in the highly interdisciplinary field of nanomaterials.

Abstract

Nanocrystals, contrary to the bulk counterparts, can exhibit size-dependent optical, electronic, magnetic, and catalytic properties. These materials can be tailored for specific applications including sensing, bioimaging, drug delivery, optoelectronics, and catalysis. This dissertation explores two types of nanocrystals, namely CdS-based quantum dots (QDs) and DNA-conjugated gold nanoparticles (DNA-AuNPs), as photocatalysts for reductive organic transformations and high mass probes for the emerging Imaging Mass Cytometry bioanalytical platform, respectively.

QDs are zero-dimensional semiconductor nanocrystals with attractive properties arising from quantum confinement effects. The tunable absorption and emission profiles make QDs desirable candidates in display technologies, lasing, and solar energy applications. On the other hand, non-radiative photophysical processes enhanced by quantum confinement in QDs are underutilised and often perceived as undesirable. One such process – Auger relaxation – can produce hot electrons with high reducing power and can be amplified further by doping the nanocrystal with Manganese (II). Part one of this thesis examines the photoreduction capabilities of Mn^{2+}-doped CdS/ZnS core/shell QDs (Mn:CdS/ZnS QDs). The doped QDs were implemented as photocatalytic coatings on reaction vessels, and several model organic reactions were evaluated including the 6-electron reduction of nitrobenzene to aniline that reached an overall internal quantum efficiency of ~3%. The findings demonstrate several-fold increase in the photoreduction efficiency of Mn:CdS/ZnS over undoped CdS/ZnS QDs, and the film set up allows for facile post-reaction workup and a range of solvent compatibility. Additionally, surface characterizations were performed to probe the changes and address the reusability of the QDs. Lastly, the initial implementation of QD coatings in flow reactors showed success. This work presents new

opportunities and diversifies the toolbox of heterogeneous photocatalysts for prospective use in organic reactions.

Imaging Mass Cytometry (IMC^{TM}) is a multiparametric imaging technique that utilizes metal-tagged antibodies as probes for investigating subcellular components via mass spectrometry. However, low-abundant cellular components can generate weak or no signals due to the small number of antibodies that bind to them. In the second part of this thesis, DNA-functionalized gold nanoparticles, each comprising >10 000 Au atoms, were examined as high mass probes for targeting low abundant microRNA. The interaction between the DNA strands on the AuNPs and microRNA-210, a biomarker for preeclampsia and hypertensive diseases, leads to the accumulation of DNA-AuNPs in cells as readily imaged with IMC. The results from IMC corroborated with traditional fluorescence-based methods, but with an enhanced sensitivity of a thousand-fold. This work is the first demonstration that DNA-AuNP can serve as high mass probes in IMC for detecting low-abundant nucleic acids.

Dedication

I dedicate this work to my first teacher, my grandfather, Myzafer Malile.

Acknowledgments

This part is for those without whom this work would not have been possible. Words cannot describe the impact Professor Jennifer Chen has had on my life. While this PhD is the last stint in my formal education, I joined her lab long ago, without any experience in materials chemistry. Under her guidance, I learned how to ask the right questions, how to push my limits. I learned how to learn. Her constant encouragement to attend conferences, workshops, and training sessions kept me motivated. Her patience, kindness, and empathy made the PhD a fulfilling journey.

I would like to thank Professor Christopher Caputo and Professor Thomas Baumgartner for their guidance throughout my project. Their insightful discussions and support always improved my work. I also thank the Professors Simon Trudel, and Katalin Hudak for offering their time and being part of the final hurdle.

Without lab mates, grad school can be daunting. Lucky for me, I had some good ones. I shared some wonderful times with Anthony, Sonu, Rithu, Yuwei, Bohan, and Karmvir attending conferences, watching Champions League games, and enjoying the occasional picnic.

My family's unwavering support during my studies removed any distractions from my path. I am forever grateful to them. Finally, I would like to thank Shakiba. Her support was a crucial part of my journey, especially in the last year.

Table of Contents

Prologue ii
Abstract iv
Dedications vi
Acknowledgments vii
Table of Contents viii
List of Figures xi
List of Tables xviii
List of Abbreviations xix
Chapter 1 - Introduction to Quantum Dots: Properties, Applications, and Synthesis 2
1.1 Quantum Confinement 3
1.2 Auger Processes in Undoped QDs 5
1.3 Manganese (II) Doped QDs 7
1.4 Applications of semiconductor nanocrystals in heterogeneous photocatalysis 10
1.5 Photoredox Catalysis 12
1.6 CdS Quantum Dots for Organic Transformation 13
1.7 Synthetic Considerations 15
1.7.1 Hot Injection Methods 15
1.7.2 Challenges with Doping 16
1.7.3 Successive Ionic Layer Adsorption and Reaction (SILAR) 17
1.7.4 Motivation and Outline 18
1.8 References 19
Chapter 2 – Mn (II)-doped CdS/ZnS Core/shell Quantum Dot Films Photocatalyze Reductive Organic Transformations With a Boost in Efficiency From Enhanced Auger Processes 24
2.1 Abstract 24
2.2 Introduction 25
2.3 Results and Discussion 27
2.3.1 Supported Mn-doped CdS/ZnS QD film as photocatalysts 27
2.3.2 Photoreduction of viologens 31
2.3.3 Photoreduction of meso-1,2- dibromo-1,2-diphenylethane 36
2.3.4 Reusability of Mn-doped QD film 42
2.3.5 Photoreduction of nitrobenzene 45

2.4 Conclusions 48
2.5 Experimental 49
2.6 References 55
2.7 Appendix 60
Chapter 3 – Doped-QD Coated Photocatalytic Flow Reactors, Challenges, and Future Directions 63
3.1 Background to Flow Reactors 63
3.2 Flow Reactor Coated with Mn-doped Quantum Dots 66
3.2.1 Experimental 66
3.2.2 Results and Discussion 66
3.3 Challenges and Limitations of Doped QDs as Photocatalysts 71
3.4 Future Directions 71
3.5 References 76
Chapter 4 – Introduction to Biomarkers, MicroRNAs (miRNA), Localized Surface Plasmon Resonance (LSPR), and Imaging Mass Cytometry (IMC) 79
4.1 Biomarkers 79
4.2 MicroRNA 80
4.3 Gold Nanoparticles 82
4.4 DNA-AuNP 83
4.5 Imaging Mass Cytometry 85
4.6 References 89
Chapter 5 - DNA-conjugated Gold Nanoparticles as High-mass Probes in Imaging Mass Cytometry 92
5.1 Abstract 92
5.2 Introduction 92
5.3 Results and Discussion 95
5.3.1 Uptake of AuNP and Detection by IMC 95
5.3.2 Multiparametric Imaging 99
5.3.2.1 Sequence-Specific Uptake and Trafficking of DNA-AuNP 100
5.3.3 Comparative Fluorescence Study 106
5.4 Conclusions and Future Outlook 109
5.5 Methods 110
5.6 References 115

5.7 Appendix 118
Chapter 6 - Challenges and Outlook on the Application of DNA-AuNP in Imaging Mass Cytometry 119
6.1 Limitations of IMC.....122
6.2 Challenges and outlook of DNA-AuNP in imaging mass cytometry 118
6.3 Future Outlook 124
6.4 References 126
Epilogue 127
List of publications 128

List of Figures

CHAPTER 1

Figure 1.1. Widening of the band gap and discretization of band energy levels resulting from quantum confinement effects. Reprinted with permission from reference 5……3

Figure 1.2. (A) Absorbance spectra of CdS QDs with increasing sizes. The energy of the first excitonic peak increases with decreasing size. The largest particle, 33 nm (red), has an absorption profile like the bulk material. (B) Dependence of the three lowest optical transitions ($1S_h1S_e$, $1P_h1P_e$, $1D_h1D_e$) on nanoparticle radius. Reprinted with permission from reference 15. Copyright 2021 American Chemical Society……5

Figure 1.3. Absorption and emission of a photon are the prominent processes occurring in the semiconductor nanocrystal. Kinetic energy transfer to an electron in the conduction band generates a hot electron. ……..…6

Figure 1.4. Tanabe-Sugano diagram for the d^5 manganese (II) ion in a tetrahedral ligand field depicting the lowest energy spin forbidden excited states. Orange arrow indicates the $^4T_1 \rightarrow {}^6A_1$ observed in the emission spectrum. Reprinted with permission from refence 36…….……8

Figure 1.5. (A) Energy transfer from the annihilation of an exciton to Mn^{2+} ion which radiatively relaxes to emit a photon. (B) Generation of a hot electron via Auger process. Non-radiative recombination of an electron and hole transfers its energy to a Mn^{2+}. The long-lived Mn^{2+} excited state then transfers that energy to a second electron in the conduction band, producing a “hot” electron…….9

Figure 1.6. Simplified ground state and excited state of $Ru(bpy)_3^{2+}$ and its electronic structure as an oxidant or reductant. Reprinted with permission from reference 57……. ……12

Figure 1.7. Various photoredox reactions catalyzed with CdSe QDs. Reprinted with permission from reference 56 ……...…14

Figure 1.8. A simplified schematic representation of sensitization of triplet state of the substrate via triplet-triplet energy transfer from the QDs. Interaction of functional groups of the precursors

with the surface of QDs provides an avenue of control on the selectivity of the hetero-coupled product. Reprinted with permission from reference 66……...…15

CHAPTER 2

Figure 2.1. Mn^{2+}-assisted Auger relaxation generates hot electrons that are be harvested for photoreduction reactions. The electron and hole transfer to the organic substrate and sacrificial donor (SD), respectively ……28

Figure 2.2. Photoluminescence spectra of during the passivation of Mn^{2+} doped CdS QDs (A) and undoped CdS QDs (B) with ZnS. Increasing number of layers of ZnS increases PL. Spectra collected under 440 nm excitation and with a 460-nm long pass filter……29

Figure 2.3. Characterizations of Mn^{2+}:CdS/ZnS QDs. (A) Absorbance (solid lines) and photoluminescence spectra (dashed lines) of doped Mn^{2+}:CdS/ZnS (red) and undoped CdS/ZnS (blue) QDs in toluene. (B) EPR spectrum of Mn^{2+}:CdS/ZnS with six lines resulting from energy splitting due to Mn^{2+} I=5/2. (C) PXRD of doped QDs (experimental in black, calculated in red, and residual difference in blue). Phase analysis results in 55 wt% wurtzite and 45 wt% zinc blende. (D) TEM images of Mn^{2+}:CdS/ZnS QDs……30

Figure 2.4. $^4T_1 \rightarrow {}^6A_1$ transition of the Mn^{2+} monitored at 580 nm showing the long-lived PL (black) as a double exponential fit (red) with components $\tau_1 = 0.141$ ms , and $\tau_2 = 1.91$ ms…….31

Figure 2.5. Energy levels of the valence and conduction bands of CdS QD[39] (black), the $^4T_1 \rightarrow {}^6A_1$ transition of the high spin Mn^{2+} in a tetrahedral geometry[30] (red), the oxidation potentials of sacrificial hole scavengers[40,41](purple) and reduction potentials of viologens[42] (blue), meso-1,1-dibromo-1,2-diphenylethane[43,44] (green) and nitrobenzene[45] (brown)……...32

Figure 2.6. Reduction of methyl viologen (MV^{2+}) to MV^{*+} by QDs. (A) UV-Vis spectral evolution over time showing the formation of the charged radical ($MV^{+\bullet}$) in the presence of doped QDs (bottom) and undoped QDs (top) under 440 nm irradiation with methanol as sacrificial electron donor. (B) Amount of $MV^{+\bullet}$ generated over the course of 55-min irradiation with doped (red) and undoped (black) QDs. Error bars are standard deviations. (C) Normalized photoluminescence (PL) intensity at 488 nm for the undoped QDs (black) and at 581 nm for the doped QDs (red) in the presence of MV^{2+} and methanol vs irradiation time……33

Figure 2.7. Photoluminescence intensity of doped (red) and undoped (black) QDs versus irradiation power at 440 nm. Deviation of PL intensity of the doped QDs from linear relationship at higher power suggests saturation of Mn^{2+} states and nonradiative Auger processes……...34

Figure 2.8. Normalized photoluminescence intensity at 488 nm and 581 nm for the undoped (black) and doped QDs (red), respectively, in water……...35

Figure 2.9. Control experiments with MV^{2+} in water show that both light and QDs are crucial for reaction to take place: (A) Spectra of solution without irradiation; and (B) spectra of solution without QDs upon blue light irradiation…….36

Figure 2.10. Debromination of DDE with doped QDs as photocatalyst in a biphasic system (H_2O/EtOAc)……..37

Figure 2.11. (A) UV-Vis spectra of the organic layer of the dehalogenation reaction of *meso*-1,2-dibromo-1,2-diphenylethane (DDE) in a biphasic system (H_2O/EtOAc), with heptyl viologen as an electron shuttle and methanol as a sacrificial agent under 395 nm irradiation, with (blue) and without methanol (red). Control reaction without irradiation shown in black. Spectrum of pure *trans*-stilbene shown illustrated with dashed lines. (B) ^{1}H NMR spectra for monitoring the reaction progress. An up-field shift in the doublets at 7.70-7.68 ppm to the doublets at 7.61-7.59 ppm shows the conversion of DDE to stilbene. NMR spectra of reactions 6, 3, 2 and 1 listed in Table 1 are shown as black, green, red, and blue trace in (B)……38

Figure 2.12. ^{1}H NMR spectra of the organic phase from the biphasic system for the reduction of DDE (in d-DMSO). Control experiment (brown, Entry 5) showed signals of DDE only, conferring the importance of heptyl viologen (HV^{2+}) as the electron shuttle between the two phases. A low concentration of HV^{2+} at 3 mol% (green, Entry 4) yielded 17 % conversion of DDE to stilbene with doped QDs, compared with 100% at 20 mol% of HV^{2+}……..…39

Figure 2.13. ^{1}H NMR spectra for monitoring the reduction of DDE in a monophasic system(in d-DMSO). Reactions with doped (purple, Entry 7) and undoped QDs (green, Entry 8) at a catalyst loading of 0.012 mol% where the doped QDs exhibited enhanced activity with only signals of stilbene detected. At a low catalyst loading (0.004 mol%), samples from both doped (red, Entry 9) and undoped (blue, Entry 10) showed incomplete reactions……...…41

Figure 2.14. (A) Percent conversion of DDE based on ^{1}H NMR data when coated vials were used back-to-back without any treatment. Each trial was 24-h of irradiation. Error bars are standard deviations of 3 replicates. (B) X-ray photoelectron spectra of Cd 3d in Mn:CdS/ZnS QD films before and (C) after the photoredox reaction of DDE. Experimental spectra shown in red and fitted curves in other colors with each doublet corresponding to spin-orbit coupling of $3d_{5/2}$ and $3d_{3/2}$…42

Figure 2.15. X-ray photoelectron spectra of S 2p of Mn:CdS/ZnS QD films before (A) and after (B) the photoredox reaction of DDE. Experimental spectra shown in red and fitted curves in other colors with each doublet corresponding to the spin-orbit coupling of $2p_{3/2}$ and $2p_{1/2}$……..45

Figure 2.16. Photoreduction of nitrobenzene (258 nm) to aniline (237 nm 280 nm) monitored by UV-Vis spectroscopy. (A & B) UV absorption spectra of the reaction solution photocatalyzed by doped (A) and undoped QDs (B) respectively. (C) Time dependence of absorbance of nitrobenzene at 258 nm for triplicate runs with doped (red) and undoped (black) QDs respectively. Error bars represent standard deviations…….46

Figure 2.17. ^{1}H NMR spectrum of post reaction solution depicting successful conversion of nitrobenzene to aniline in d-DMSO. Inset shows the ratio between integrated peaks…….47

Figure A1. Calibration curve for Mn, Cd, and Zn…….62

CHAPTER 3

Figure 3.1. (A) Light driven photochemical reaction. (B) Photochemical formation of electron donor-acceptor (EDA) complex. (C) Photoredox catalysis. (D) semiconductor assisted Photoredox catalysis. (E) Typical schematics of flow reactors. (F) Effect of distance on the irradiation intensity. Reprinted with permission from reference 3……..…..…64

Figure 3.2. Decarboxylative arylation adapted for flow conditions. Image adapted from reference 9. License link https://creativecommons.org/licenses/by-nc-nd/4.0/legalcode.....65

Figure 3.3. Mn-Doped CdS/ZnS coated pipette for use in a photocatalytic flow reactor under 395 nm illumination. Reaction mixture flowed at a rate of 2 mL/h through the QD-coated reaction chamber and collected in a 20 ml vial…….67

Figure 3.4. (A) UV-Vis spectra of aliquots collected from the reaction at a flow rate of 2 mL/h. (B) Average of three trials showing the peak intensities at 236 nm (grey squares) from aniline and 258 nm (red circles) for nitrobenzene. Datapoints in the 0-2 mL range show unreacted material present in the connection tubing……..…68

Figure 3.5. ^{1}H NMR spectrum of post reaction solution at a flow rate of 2 mL/h. Peaks at 6.47-6.52 ppm (c), 6.55-6.58 ppm (b), and 6.98-7.03 ppm (a) depict the presence of aniline. The broad peak downfield of aniline (~7.2 ppm) can be a combination of phenylhydroxylamine and nitrosobenzene…….. 69

Figure 3.6. (A) Reductive dehalogenation of phenacyl bromide. (B) Oxidative hydroxylation of arylboronic acids. (C) Radical addition of *Se*-phenyl *p*-tolueneselenosulfonate to alkyl vinyl ethers. Reprinted with permission from reference 13.……..….....72

Figure 3.7. Proposed mechanism for carbon-carbon cross coupling reaction where photoredox catalysis is used in tandem with the nickel catalytic cycle. Replacement of iridium photoredox cycle with the QD photoredox cycle can potentially increase the efficiency of the reaction. Reprinted with permission from reference 14……73

Figure 3.7. Translation of batch reaction to flow reactor via HTE. Reprinted with permission from reference 10. Licence link https://creativecommons.org/licenses/by-nc-nd/4.0/legalcode.....74

CHAPTER 4

Figure 4.1. Interaction with the electric field of light shifts the conduction electrons of the nanoparticle, giving rise to a dipole. The oscillation of this dipole results in intense colours. Reprinted with permission from reference 30……..…82

Figure 4.2. Illustration of nanoflare system developed by Mirkin *et al*. Hybridization of the recognition sequence on the AuNP with a dye labeled reporter sequence orients the dye close to the AuNP surface, quenching its fluorescence. Upon cell entry, the mRNA target displaces the reporter sequences restoring the fluorescence of the dye. Reprinted with permission from reference 38. Copyright 2009 American Chemical Society……...84

Figure 4.3. Priniple of operation of Imaging Mass Cytometry. (TOP)Lanthanide-labelled samples are ablated with a laser 1 mm in diameter. The plume of ions is ionized in an ICP torch then

analyzed with a time-of-flight mass analyzer. (BOTTOM) Each ablated spot corresponds to one image pixel and is generated by collecting the m/z signal over a 10 ms time window. Signals corresponding to various ions from the same ablated spot are then overlaid to generate multiplexed images. Reprinted with permission from reference 44……...……85

Figure 4.4. Diagram of the RNAscope assay mode of operation. (Step 1) Tissues or cells are fixed and permeabilized. (Step 2) Tissues or cells are incubated with RNA-sequence specific Z probes. (Step 3) Multiple signal amplification species are introduced comprising amplifiers, labels, and probes. (Step 4) Conventionally imaged with fluorescent microscope. Reprinted with permission from reference 49……...…87

CHAPTER 5

Figure 5.1. Different types of DNA-AuNP employed for IMC (Type I), fluorescence tracking (Type II) and Energy-Transfer-Based assay for miRNA-210 detection (Type III)……..…95

Figure 5.2. IMC images of cells incubated with increasing concentration of gold nanoparticles for 24 h: 0.001 nM (a, d); 0.01 nM (b, e); and 0.1 nM (c, f). Signals from Ir_{191}-labelled DNA intercalator (blue) and Au (red) are overlaid in a-c, and signals from Au alone are shown in d-f for clarity. Scale bar: 100 μm……...96

Figure 5.3. Fluorophore-tagged AuNP (red) with increasing concentrations in cells media. Fluorescence signal is observed at nanoparticle concentration of 1 nM. Little to no signal was observed at 0.1 and 0.5 nM of AuNP in growth media. Nuclei and late endosomes are shown in blue and green, respectively. Scale bar: 10 μm. Arrangement of oligonucleotides on the AuNP is depicted in Figure 5.1, Type II……97

Figure 5.4. Z-stack confocal microscopy images of cells incubated with 1 nM of Cy5-tagged AuNP: Signals of Cy5 displayed in red, late endosome in green, and DAPI in blue. The vertical distance between confocal planes is 1 μm. Scale bar: 10 μm……..…98

Figure 5.5. Multiparametric imaging with IMC: merged image of all signals (a); images of AuNP (b), pankeratin (c), late endosome (d), DNA (e), and Ki-67 (f). Scale bar: 100 μm……99

Figure 5.6. IMC images of cells incubated with AuNP-Probe or AuNP-Scramble under normoxic (a and c) and hypoxic (b and d) conditions: DNA (blue), pankeratin (green), and AuNP (red). Au

signal (red) is shown in e-h. Inset depicts representative outlines of nuclei (light blue) and cells (green) from segmentation. Scale bar: 100 μm……101

Figure 5.7. Quantification of Au signals from cells incubated with AuNP-Scramble and AuNP-Probe under normoxic (grey) and hypoxic (white) conditions: Au signals in whole cells (a), cytoplasm (b), and nuclei (c). Hypoxia was induced by incubating cells at 3% oxygen……..102

Figure 5.8. Representative images of all signals from IMC for samples with different conditions: signals of Au in red, late endosome in yellow, Ki-67 in cyan, pankeratin in green, and DNA in blue. The cellular markers show negligible variations in intensity. Scale bar: 100 μm…….103

Figure 5.9. Analysis of IMC signals corresponding to other biomarkers: a) pankeratin, b) DNA, c) Ki-67……104

Figure 6.10. Additional IMC images of AuNP-Scramble (a and b) and AuNP-Probe (c and d) under normoxic and hypoxic conditions, respectively. Hypoxia was induced by incubating cells in growth media with 100 μM $CoCl_2$. Nuclei is shown in blue and Au signal in red. Images e–h show only the gold signals for clarity. Scale bar: 100 μm……...104

Figure 5.11. Additional IMC studies of cells incubated with AuNP-Scramble and AuNP-Probe under normoxic (grey) and hypoxic (white) conditions. Au signals in cells are integrated and quantified. Hypoxia was induced by incubating cells in growth media with 100 μM $CoCl_2$…….105

Figure 5.12. A comparison of nanoparticle (type II DNA-AuNP, Scheme 1) uptake in normoxia vs. hypoxia using confocal fluorescence microscopy. Panels a and b show merged signals of nuclei (blue), lysosome (green), and Cy5-DNA-AuNP (red). Panels c and d show Cy5 signal that reports the location of AuNP. Scale bar: 10 μm……106

Figure 5.13. Relative miRNA-210 levels of cells under normoxic (white) and hypoxic conditions quantified by qRT-PCR. Hypoxia was induced by decreasing O_2 to 3% (blue) or adding $CoCl_2$ to growth media (striped). An upregulation of miRNA-210 of ~3-fold under hypoxia is observed compared to normoxia……..107

Figure 5.14. Energy-transfer-based nanoparticle assay for miRNA-210 analysis. Fluorescently-tagged AuNP-Scramble (a, b) and AuNP-Probe (c, d) were incubated with cells under normoxic and hypoxic conditions. Merged images showing nuclei (blue), lysosome (green) and AuNP-Cy3

(red, also shown separately in e-h). An increase in Cy3 signal is observed for cells with AuNP-Probe under hypoxia (3% O_2). Scale bar: 10 μm……...……108

Figure 5.15. Probing miRNA-210 levels using energy-transfer-based nanoparticle assay. The fluorescent signals of AuNP-Scramble-Cy3 and AuNP-Probe2-Cy3 under normoxia (blue) and hypoxia (stripe) obtained from confocal microscopy: in cells (a), in cytoplasm (b), and from the nucleus region (c). The binding of miRNA-210 to AuNP-Probe2-Cy3 leads to the release of Cy3-labelled DNA and an increase of ~2.5–3-fold in fluorescence intensity in hypoxic cells……..109

CHAPTER 6

Figure 6.1. Signals from two laser-ablated spots (blue and green) in the calibration tape over the course of 20 hours for typical metals used in multiparametric screening in IMC……..…120

Figure 6.2. Various categories and subcategories endocytosis in cells. Reprinted with permission from reference 9……...122

Figure 6.3. Internalization pathways of macrophage derived cells lines (blue) and Human cell lines (red) for surface functionalized gold nanorods. Reprinted with permission from reference 11….124

List of Tables

CHAPTER 2

Table 2.1. Summary of dehalogenation reaction of DDE: biphasic system (H_2O/EtOAc) with HV^{2+} as electron shuttle (Reactions 1-6); monophasic reduction in EtOAc (without HV^{2+}, Reactions 7-10). All reactions were irradiated for 24 h……..40

Table 2.2. Binding energies of Cd (3d) and S (2p) in Mn-doped CdS/ZnS core/shell films before and after photoredox reaction compared with literature…….43

Table 2.3. Atomic % composition obtained from XPS of crosslinked Mn:CdS/ZnS QD film before and after reaction. Signals of Indium come from the ITO substrates and that of Si come from MPTMS used to anchor the QDs on the substrate. A significant increase in In 3d signal was observed post reaction, suggesting the loss of QDs. Note that Mn signals overlapped with loss structures of other species and could not be fitted or quantified……44

Table A1: Elemental analysis of QDs with ICP-OES ..……..……62

List of Abbreviations

AuNP	gold nanoparticles
B.E.	binding energy
CB	conduction band
CD	cluster of differentiation (see appendix 5.7 for biomarker explanation)
CdS	cadmium sulfide
CdSe	cadmium selenide
cfNA	cell-free nucleic acid
CME	clarithin mediated endocytosis
Conc.	concentration
DDE	*meso*-1,1-dibromo-1,2-diphenylethane
DMSO	dimethyl sulfoxide
DNA-AuNP	DNA functionalized gold nanoparticles
dsDNA	double stranded DNA
EDA	electron donor-acceptor
EDTA	ethylenediaminetetraacetic acid
EPR	electron paramagnetic resonance
EtOAc	ethyl acetate
FRET	Förster resonance energy transfer
HCO_2^-	formate
HMDM	human monocyte-derived macrophages
HOMO	highest occupied molecular orbital
HTE	high-throughput experimentation
HUVEC	human umbilical vein endothelial cells
HV	heptyl viologen
ICP	inductively coupled plasma
ICP-OES	inductively coupled plasma – optical emission spectroscopy
IMC	imaging mass cytometry
IQE	internal quantum efficiency
ISC	intersystem crossing

ITO	indium tin oxide
Ki-67	Kiel-67(see appendix 5.7 for biomarker explanation)
LED	light emitting diode
LSPR	localized surface plasmon resonance
LUMO	lowest unoccupied molecular orbital
MALDI	matrix assisted laser deposition ionization
MeOH	methanol
miRNA	micro RNA
Mn:CdS	manganese-doped cadmium sulfide
Mn:CdS/ZnS	manganese-doped cadmium sulfide with zinc sulfide shell
mRNA	messenger RNA
MV	methyl viologen
NHE	normal hydrogen electrode
NMR	nuclear magnetic resonance
Pankeratin	Pan cytokeratin (see appendix 5.7 for biomarker explanation)
PL	photoluminescence
PXRD	powder x-ray diffraction
QDs	quantum dots
QLED	quantum light emitting diode
qRT-PCR	quantitative reverse transcription polymerase chain reaction
RAB7	Ras-associated binding (see appendix 5.7 for biomarker explanation)
RISC	RNA-induced silencing complex
SD	sacrificial donor
SET	single electron transfer
SILAR	successive ionic layer adsorption and reaction
ssDNA	single stranded DNA
TEM	transmission electron microscopy
TiO2	titanium dioxide
TOF	time of flight
UV	ultraviolet
UV-Vis	ultraviolet -visible

VB	valence band
XPS	x-ray photoelectron spectroscopy
ZnS	zinc sulfide

Part One: Manganese-doped CdS/ZnS Core/shell Quantum Dot Films as Photocatalysts for Organic Reactions

Chapter 1 – Introduction to Quantum Dots: Properties, Applications, and Synthesis

1. Quantum dots

Quantum dots (QDs) are a subclass of semiconductor nanocrystals. They are zero-dimensional nanomaterials, with typical diameters of 1-10 nm, that exhibit strong quantum confinement effects.[1] Quantum confinement produces a variety of properties in QDs that are not present in the bulk material. These effects include widening of the band gap, tunable valence and conduction band potentials, and efficient charge generation and migration. The confinement also generates discrete energy levels within the valence and conduction bands. Therefore, QDs possess properties of both molecules and bulk materials and are used in display technologies, solar cells, and bio-imaging techniques. The most widely studied QDs are II-VI semiconductors such as CdS, ZnS, CdSe, which can be produced with high quality and narrow size distributions via hot injection methods.[2] Additionally, their implementation in QLED TVs shows that large scale production of QDs for commercial applications can be established.

This chapter contains background information for part one of this dissertation. First, the fundamentals of quantum confinement and the unique properties of QDs, with an emphasis on Auger processes, are presented. Second, the concept of doping and its role on the photophysical processes in QDs are introduced. Third, applications of QDs in heterogeneous photocatalysis and their synthesis are presented. The chapter concludes with the motivation and outline of the research.

1.1 Quantum confinement

The spatial arrangement of atoms in a molecule or bulk crystal gives rise to distinct electronic states that govern the probabilities of optical transitions. An atom contains discrete energy states occupied by electrons, which upon excitation generate sharp absorption and emission lines[3] and are typically determined by the crystal structure and the identity of the atoms.[4,5] The three-dimensionally repeating unit cell creates a periodic potential which in turn gives rise to energy ranges of allowed electronic states (i.e. bands).[6] In a typical bulk semiconductor, the electronic states of the valence and conduction bands are separated by a band gap – an energy continuum where electronic states do not exist. When the dimensions of the material decrease to the nanoscale, quantum confinement effects generate atom-like band energies (Figure 1.1), and size tunable band gap.[7,8–10] The desirable properties of QDs are explored for use in display technologies,[11] bioimaging,[12] and photocatalysis.[13]

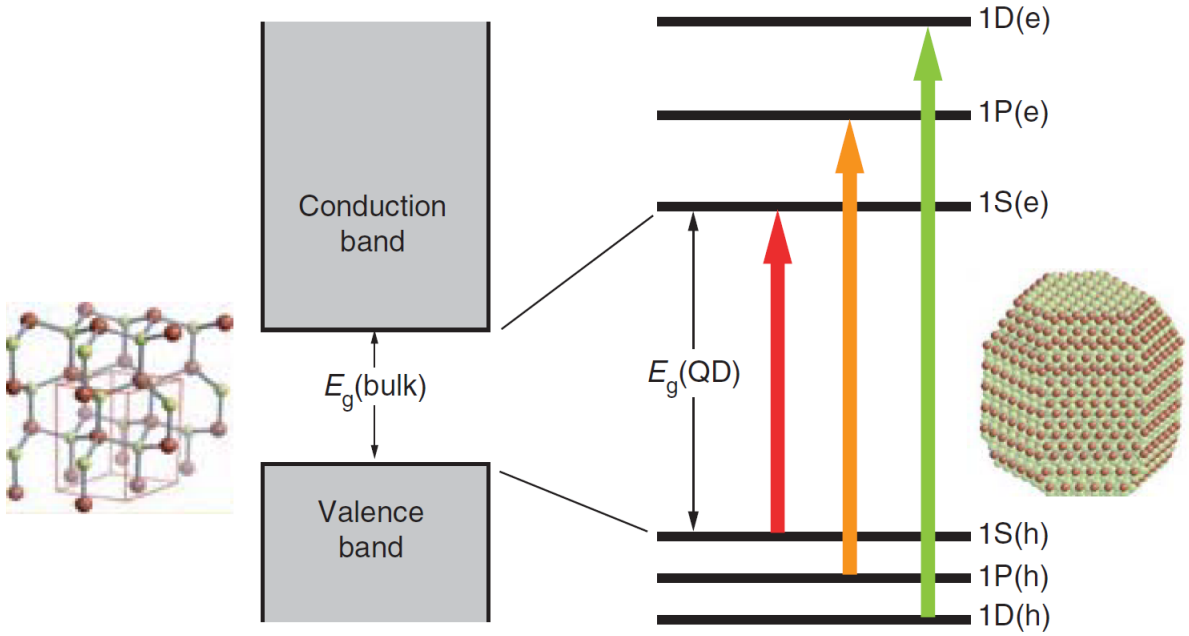

Figure 1.1. Widening of the band gap and discretization of band energy levels resulting from quantum confinement effects. Reprinted with permission from reference 5.

The most important parameter for understanding the interaction of electromagnetic radiation with a QD is the exciton Bohr radius (a_B) – the physical distance between an excited electron and the vacancy (i.e. hole) created upon absorption of a photon.[14] The Bohr radius varies with materials and indicates the physical limit where the quantum confinement starts affecting the electronic structure. The size ofQDs restricts the spatial separation of the excited electron and the hole below the Bohr radius, in turn creating a strong confinement regime.[14,15]Equation 1.1 shows the relationship between the band gap of QD (E_{QD}) with the bulk band gap energy ($E_{(bulk)}$), the nanocrystal radius in the strong confinement condition, and Coulombic interaction of the electron-hole pair.[15]

$$\boldsymbol{E_{(QD)} = E_{(bulk)} + \frac{\pi^2\hbar^2}{2m_{e,h}R^2} - 1.8\frac{e^2}{\varepsilon R}} \qquad \textbf{Equation 1.1}$$

The quantum confinement term (second term on the right side in Eq. 1.1) is related to the effective mass of the electron-hole pair ($m_{e,h}$), the particle radius (R), and the reduced Planck's constant ($\hbar$). The coulombic interaction term, $e^2/\varepsilon R$, depends on the dielectric constant (ε) and particle radius, with e being the elementary charge of the electron. Therefore, with decreasing particle size, the term describing the coulombic interaction becomes less dominant in the overall contribution to E_{QD}, while the exciton energy term increases due to its dependence on R^{-2}.[1,16]

In the absence of band mixing effects, the discrete quantized states in QDs can be characterized by the quantum numbers L and n.[17] Angular momentum, represented by L, defines the motion of charge carriers (electrons or holes) in the strong confinement regime while quantum number n, denotes the number of the states in the specific symmetry.[18] Conventionally, the energy states (1S,1P,1D etc.) are depicted with momentum indicated by a letter (L=0 → S, L=1→ P, L=2 → D) and n preceding L.[19] Figure 1.2 shows the experimentally observed quantum size effect on

absorption as described by Eqn. 1.1. Figure 1.2A presents the absorbance spectra of various QDs with increasing radius from 1.2 nm to 33 nm. The smaller particles with radius 1.2 nm (green trace) and 1.5 nm (blue trace) have absorption profiles with peaks corresponding to the individual transitions ($1S_h1S_e$, $1P_h1P_e$) in contrast to the 33-nm particle where only the first excitonic peak is observed.[1] Figure 1.2B shows the dependence of the three lowest transitions on particle radius. In line with the quantum confinement effect, as the size of the QDs decreases the energy gap between the optical transitions increases, in turn producing a blue shift in the excitonic peaks in the absorbance spectrum.[1,20]

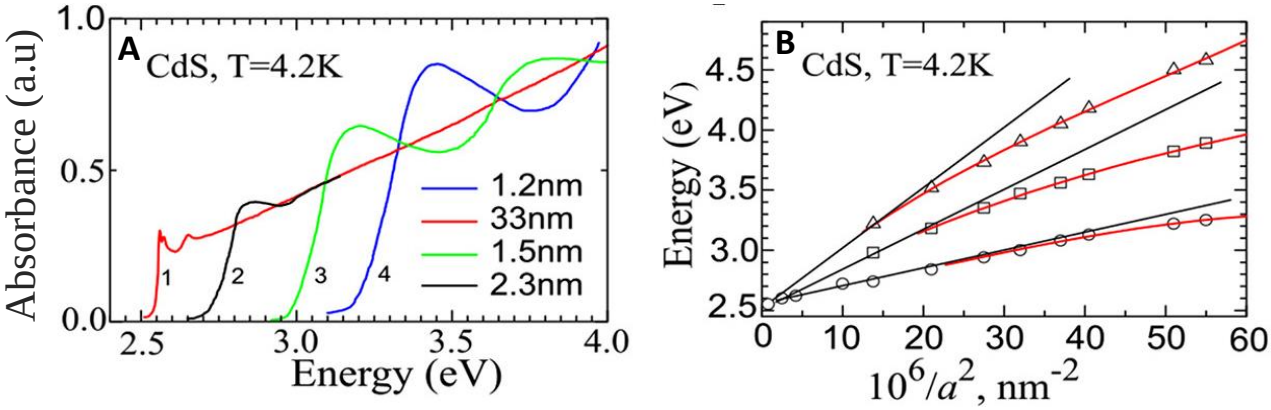

Figure 1.2. (A) Absorption spectra of CdS QDs with increasing sizes. The energy of the first excitonic peak increases with decreasing size. The largest particle, 33 nm (red), has an absorption profile like the bulk material. (B) Dependence of the three lowest optical transitions ($1S_h1S_e$, $1P_h1P_e$, $1D_h1D_e$) on nanoparticle radius. Reprinted with permission from reference 15. Copyright 2021 American Chemical Society.

1.2 Auger processes in undoped QDs

Upon absorption of light, the excited electron undergoes rapid thermal relaxation to the conduction band edge, which can radiatively recombine with the hole to yield photoluminescence. Alternatively, Auger relaxation or Auger recombination can occur. It is a nonradiative process where the energy from the recombination of the electron-hole pair (exciton) is not emitted as a

photon but is transferred to a third charge carrier (electron or hole), thereby further exciting it to elevated energy states.[7,21,22] Figure 1.3 depicts the absorption and emission process vs the non-radiative three-particle Auger relaxation. Auger energy transfer lifetimes range from 10s to 100s picoseconds but can be as low as 150 fs, and commonly vary with size and shape of QDs.[22] These lifetimes are significantly shorter than emission lifetimes (~ 10 ns), thus making the Auger process an important and competitive decay pathway.[23,24] In bulk semiconductors, Auger relaxation has low probability due to thermal and momentum conservation barriers.[16,23] Conversely, under the quantum confinement regime, the momentum conservation rules relax, thus enhancing Auger recombination rates in QDs.[25]

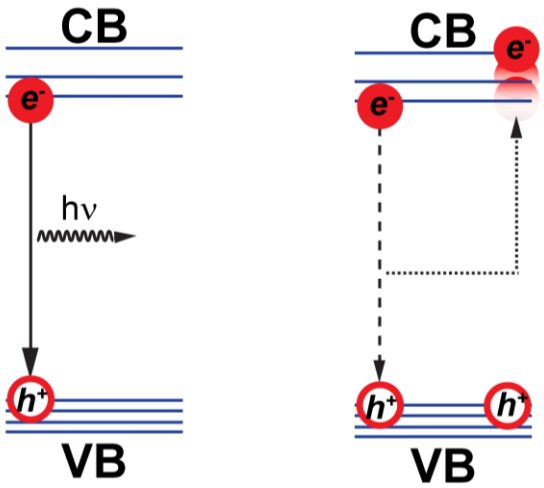

Figure 1.3. Absorption and emission of a photon are the prominent processes occurring in the semiconductor nanocrystal. Kinetic energy transfer to an electron in the conduction band generates a hot electron.

Internal carrier-carrier interactions in QDs facilitate processes such as multi-exciton stimulated emission and photon up conversion, which can be utilized for lasing technologies and solar energy harvesting applications respectively.[2,21,26] However, in QDs, multi-exciton emission is hindered by Auger relaxation. This competitive and non-radiative process generates electrons with enough energy to escape the nanocrystal leading to the darkening of the QDs.[7] Thus, Auger

relaxation is generally detrimental for lasing and solar energy applications; however, Auger-relaxation can yield hot electrons. These electrons have higher reducing power than the ones at the conduction band edge and can be invaluable for photocatalysis.[16,27] Therefore, methods to control the internal photophysical processes which promote Auger relaxation in QDs, including surface passivation or doping, are sought-after for specific applications.

1.3 Manganese (II) - doped QDs

The incorporation of impurities in materials to control their properties is an important aspect of many technologies. Generally, doping changes the properties of semiconductors[28] by creating defect states, altering energy levels, and by providing non-radiative pathways for charge carrier interactions. Paramagnetic dopants, such as Mn^{2+}, influence several processes in QDs including photoluminescence and Auger relaxation because of spin-carrier interactions.[27] With some robust synthetic methodologies already established, numerous fundamental studies on Mn-doped nanocrystals of various sizes and shapes, have been carried out.[14,29]

Doping QDs with Mn^{2+} ion introduces interband electronic states that directly affect the radiative and nonradiative photophysical processes. Ligand field theory describes the Mn^{2+} electronic structure in the CdS lattice.[30] As a substitutional impurity, a Mn^{2+} dopant replaces a Cd^{2+} ion in the tetrahedral geometry bonded to 4 sulfur atoms. The Mn^{2+} ion (d^5) has a ground state consisting of five unpaired electrons in half-filled *d* orbitals. It has an orbital angular momentum of 0, and hence exhibits a singlet ground state with 6-fold spin degeneracy, denoted with the term symbol ^6S. The first spin-flip excited state of the Mn^{2+} free ion is ^4G with an energy of ~ 3 eV above the ground state. In tetrahedral ligand field, the ground state ($^6A_1$) remains symmetric and the 5-fold degenerate 3d orbital splits into t_2 and *e* sets. The lowest energy transition is $^4T_1 \rightarrow {}^6A_1$

(~2.1 eV) and has the characteristic yellow-orange luminescence peak in the spectra of doped QDs.[31–33] Figure 1.4 shows the Tanabe-Sugano diagram splitting of the d^5 Mn^{2+} in a tetrahedral field: the lowest energy transition is depicted with the orange arrow (Figure 1.4). Typically, such transitions are spin forbidden with low probabilities. However, the selection rules can be overcome by spin-orbit coupling at the Mn^{2+} centre.[33–35] Mn-Mn exchange interactions overcome the spin forbiddeness of the $^4T_1 \rightarrow {}^6A_1$ transition as well.[34]

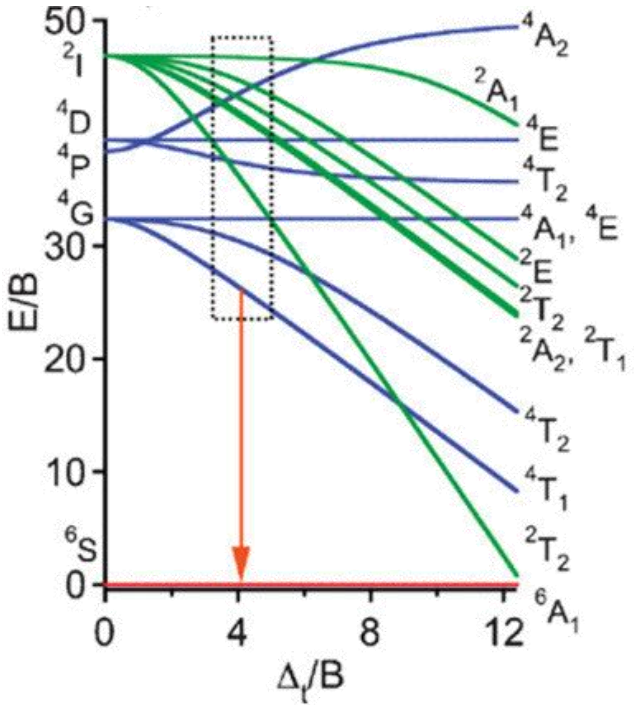

Figure 1.4. Tanabe-Sugano diagram for the d^5 manganese (II) ion in a tetrahedral ligand field depicting the lowest energy spin forbidden excited states. Orange arrow indicates the $^4T_1 \rightarrow {}^6A_1$ observed in the emission spectrum. Reprinted with permission from refence 36.

In Mn^{2+}-doped QDs, the generation of an exciton leads to a rapid transfer of the exciton energy to the dopant in sub-nanosecond timeframes.[37] The excited dopant can relax radiatively emitting a photon at ~2.1 eV, or the energy can be transferred to a second electron in the conduction band via the Auger process, thus generating a hot electron.[24,36] Figure 1.5A shows the radiative

pathway facilitated by the Mn^{2+} and Figure 1.5B shows the nonradiative pathway and the role of Mn^{2+} in the Auger process and the resultant hot electron.

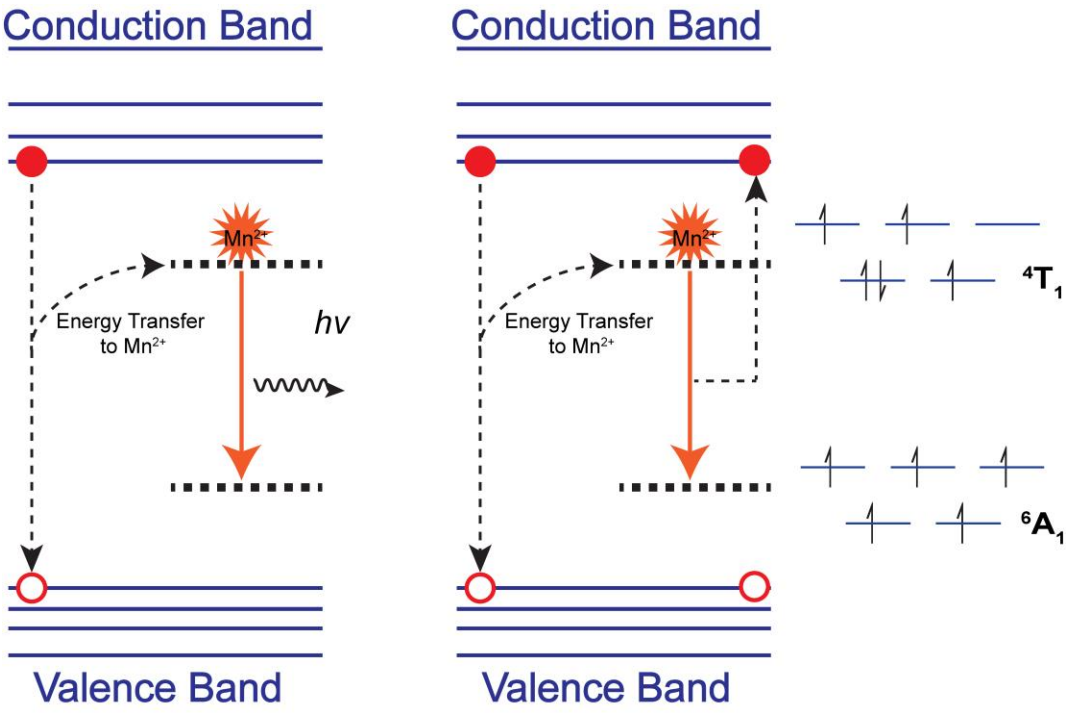

Figure 1.5. (A) Energy transfer from the annihilation of an exciton to Mn^{2+} ion which radiatively relaxes to emit a photon. (B) Generation of a hot electron via Auger process. Non-radiative recombination of an electron and hole transfers its energy to a Mn^{2+}. The long-lived Mn^{2+} excited state then transfers that energy to a second electron in the conduction band, producing a "hot" electron.

Typically, intraband cooling of hot carriers - a subpicosecond to picosecond process - hinders the extraction of a hot electron from the semiconductor. Magnetic doping of the QDs overcomes intraband cooling by facilitating extremely fast rates of spin-exchange interactions that result in an overall uphill energy transfer.[39] Klimov *et al.* reported that energy transfer from the absorption of a photon to the $^4T_1$ state of the Mn^{2+} occurs in a 140 fs timeframe (Figure 1.5 A).[27] Similarly, the energy transfer from the exited Mn^{2+} ion to an electron in the conduction band occurs on a 150 fs timeframe with a rate of 14 eV/ps (Figure 1.5B). Compared with the intraband cooling rate of ~2 eV/ps, the rate of energy gain attributed to the Mn-facilitated Auger process is ~7-fold

higher.[27] Therefore, Mn-doped QDs have an increased probability of producing hot electrons which have greater reduction power conduction band electrons. The existence of hot electrons in Mn-doped QDs has been probed via spectroelectrochemical studies and photon-to-current conversion devices. Gamelin *et al*. showed that, under illumination, Mn-doped QDs produced significantly larger photocurrents (~57 A/W) than the undoped dots (~3 A/W).[40] Son *et al*. demonstrated the application of colloidal doped QDs in water splitting and H_2 production where the doped QDs outperformed their undoped counterparts because of the highly reducing hot electrons.[41] It can be expected that such photogenerated hot electrons are poised to enhance the efficiencies of various light-driven processes including photocatalysis and photoredox reactions.

1.4 Applications of semiconductor nanocrystals in heterogeneous photocatalysis

Photocatalysis involves the harnessing of light energy using catalytic amounts of light-absorbing species such as metal complexes, organic dyes, and inorganic materials to drive chemical reactions.[42–44] Heterogeneous photocatalysis consists of a light-driven catalytic process that occurs on the surface of a material.[45] The semiconductor serves as a light harvesting material that, upon absorption of a photon with energy greater than its band gap, promotes an electron to the conduction band leaving a positively charged vacancy in the valence band. The photoexcited material is thermodynamically unstable.[45,46] The photogenerated charge carriers eventually recombine radiatively or non-radiatively to restore the material's thermodynamic stability. Therefore, spatial charge separation of the electron and hole to surface sites for redox purposes is crucial in photocatalytic applications and requires careful engineering of the size, shape, and composition of semiconductors.[47]

Titanium dioxide is one of the most studied inorganic materials as a heterogenous photocatalyst due to its stability, abundance, and nontoxicity. It has been widely implemented in environmental purification,[48] H_2 production,[49] artificial photosynthesis,[50] CO_2 reduction,[51] and solar cells.[52] However, implementation of TiO_2 for organic transformation remains limited. First, the wide band gap (3.2 eV) makes titanium dioxide incompatible for organic photocatalysis because most organic compounds absorb UV light as well.[51,53] This issue may be overcome by doping the TiO_2 with metal ions and shifting the absorption profile to the visible region.[54] Second, the lifetime of the photogenerated charge carriers in TiO_2 lies in the 10-100 ns range. Short lifetimes decrease the probability of the diffusion of charge carriers to the surface of the material in turn decreasing its redox capability. Third, the photoreduction capabilities of TiO_2 nanoparticles diminish significantly when immobilized on a substrate.[55] This limitation can hinder the scope of application of TiO_2 nanoparticles as heterogeneous photocatalysts. While efforts have been made to address these challenges, the application of TiO_2 has remained in the areas of water decontamination processes.

In contrast, the unique optoelectronic properties of metal-chalcogenide semiconducting QDs make them great candidates as light harvesters for photocatalytic applications.[17,26] QDs such as CdS, ZnS, CdSe were studied for water splitting reactions and CO_2 reduction.[30] Recently, the research has shifted towards applying them to complex organic reactions, such as single electron transfer reaction (SET), oxidative bond coupling (C-C, S-S, C-N), selective bond oxidation (N-H, CH_3), and functional group reduction (-NO_2, C=O,).[56] An important trait of QDs is their tunable band gap, which can be tailored to produce charge carriers with specific redox potentials.[7,16]

1.5 Photoredox catalysis

In conventional photoredox catalysis, light-absorbing species such as ruthenium and iridium polypyridyl complexes function as an oxidant and reductant when irradiated with visible light. Upon absorption of a photon, an electron from the t_{2g} nonbonding orbital in the metal centre is promoted to the π^* orbital of the ligand. In ruthenium and iridium poly-pyridyl complexes, metal

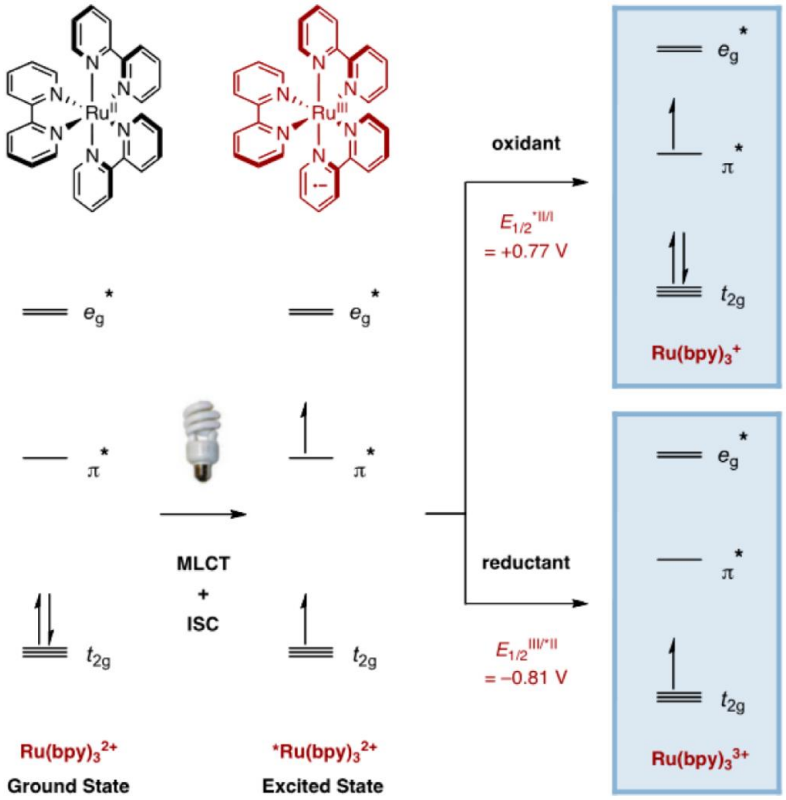

Figure 1.6. Simplified ground state and excited state of Ru(bpy)$_3^{2+}$ and its electronic structure as an oxidant or reductant. Reprinted with permission from reference 57.

to ligand charge transfer occurs rapidly after excitation generating a singlet excited state. Intersystem crossing produces a long-lived triplet state (Figure 1.6).[57] The resulting configuration of the photocatalyst possesses a high energy electron in the π^* and a vacancy in the metal centre and allows the photocatalyst to function as oxidant and reductants simultaneously under mild conditions. It can donate a high energy electron from the π^* of the ligand or accept an electron in

the low energy orbital of the metal.[58,59] Regardless of whether oxidation or reduction occurs first, there is a strong thermodynamic driving force for the complex to return to the original oxidation state. Thus, these organometallic complexes are capable of catalyzing redox neutral reactions. Also, they exhibit long photo-exited state lifetimes, absorption in the visible region, and powerful redox potentials.[60,61] Originally they were employed for generating radical intermediates to form C-C bonds. Recently, more useful applications have emerged, including cycloadditions, alpha alkylation of aldehydes, and dehalogenation of alkyl halides. [57,62,63]

The transition-metal complexes are versatile photoredox catalysts in redox neutral reactions, and single electron transfer processes. However, the drawbacks of iridium and ruthenium complexes include their high costs, toxicity, and the need to tailor the ligands for specific reactions – a process that introduces additional synthetic steps and increases the probability of material loss. Importantly, transition-metal catalyzed photoredox reactions occur under homogenous conditions. The separation of the photocatalyst from the reaction mixture adds post-reaction workup steps. Nanomaterials such as CdS quantum dots, applied as a heterogeneous system, can provide cost-effective and practical alternatives to transition-metal complexes in photoredox catalysis.[9]

1.6 CdS quantum dots for organic transformation

QDs are easily modifiable nanomaterials, with light-absorption capabilities over a wide range of frequencies, that can overcome some of the limitations of ruthenium and iridium complexes. Because of the high surface to volume ratio most of the atoms reside on the surface of the QDs thereby increasing the interaction of the charge carriers with the molecules in the reaction mixture. The large number of atoms in the QDs (~10 000 atoms) makes these nanocrystals a

heterogenous catalyst where each QD serves as mini reactor facilitating hundreds of redox events simultaneously.[8,64] Although bare QDs lack remarkable photocatalytic activity, passivating the surface with a ligand or a shell with a material that has a wider band gap can address this issue.[65] A handful of examples of CdS and CdSe QDs for photoredox catalysis of organic reactions have been demonstrated. Figure 1.7 shows various reactions where CdSe QDs replace $Ir(ppy)_2(dtbbpy)^{3+}$ or $Ru(bpy)_3Cl_2$. All but reaction D (reductive dehalogenation) involve bond formation. The results show that 3-nm CdSe QDs at a loading of ~ 0.005 mol% outperformed $Ir(ppy)_2(dtbbpy)^{3+}$ and $Ru(bpy)_3^{2+}$, but not $Ir(ppy)_3$.[56]

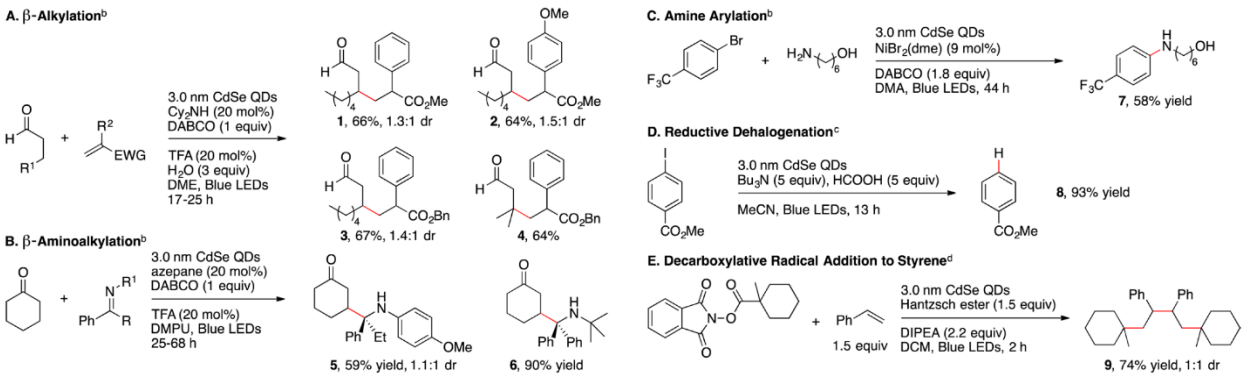

Figure 1.7. Various photoredox reactions catalyzed with CdSe QD. Reprinted with permission from reference 57.

Another work shows that the interaction of molecules with the surface of QDs can be exploited to promote stereoselectivity in organic reactions. Weiss *et al.* used CdSe QDs as photocatalysts and reusable scaffolds simultaneously for the homo- and hetero-intermolecular 2+2 cycloadditions. This reaction constructs tetra-substituted cyclobutanes which serve as starting materials in medicinal chemistry. Figure 1.8 shows orientation of reactants on the surface facilitated by the carboxylic groups, exciton formation in the QDs, and the energy transfer to the triplet state of the organic reactants.[66,67] The results showed great diastereoselectivity and regioselectivity and surpassed previous methods. Additionally, by controlling the size of the QDs

they were able match the redox potential of the excited electron in the QDs and match it with the triplet states of the organic molecules. These results are promising, however, the performance of QDs can be further improved by introducing dopants to increase the reduction potential of the electrons in QDs. This can be achieved via Auger relaxation process, as discussed in Section 1.3, in Mn-doped CdS.

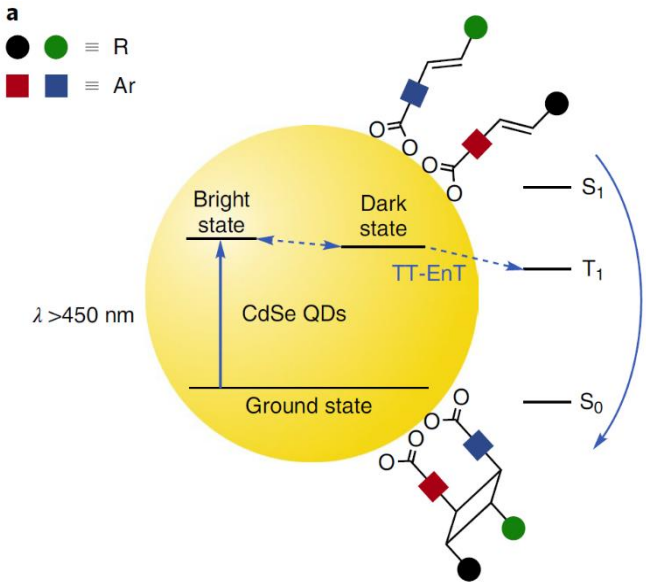

Figure 1.8. A simplified schematic representation of sensitization of triplet state of the substrate via triplet-triplet energy transfer from the QDs. Interaction of functional groups of the precursors with the surface of QDs provides an avenue of control on the selectivity of the hetero-coupled products. Reprinted with permission from reference 66.

1.7 Synthetic considerations

1.7.1 Hot injection methods

A typical synthesis of colloidal QDs involves injecting precursors that decompose at high temperatures to yield a burst of nucleation events followed by nanocrystal growth.[68] The hot injection technique ensures rapid mixing of precursor solutions while preferentially binding surfactants attach to the surface of the nanocrystals and provide control over extent of size and

shape of QDs. Initially developed for the synthesis of CdSe QDs, hot injection methods have been adapted for various nanomaterials and produce highly monodispersed particles.[69] These techniques facilitate the independent control over nucleation and growth of QDs, leading to highly monodispersed batches.

The size of the QDs is directly linked to the concentration of nuclei formed; the greater the numbers of initial nuclei the smaller the final size QD and vice versa. Surfactants and long-chained primary amines provide stabilization during the high-temperature growth. Finally, nanocrystal growth depends heavily on temperature; CdS QDs have a threshold growth temperature of 265 ^{O}C, below which the nanocrystal growth decreases drastically.[70] The developments of precursor libraries and optimizations on nucleation and growth conditions have led to a rapid production of spectrally pure new structures of semiconductor nanocrystals.

1.7.2 Challenges with doping

Not all impurities work as dopants. The concentration of dopants in the reaction mixture is typically ten times less than the host material. These conditions result in 1% or less in dopant concentration in the synthesized QDs.[23] Therefore, it is crucial to not only find the right dopants, but also to fully characterize the QDs and analyze the extent of doping. First, for successful doping, the dopant should have "good solubility" in the host material. Mn^{2+} and Co^{2+} have been effectively incorporated in CdS and CdSe QDs while attempts of doping QDs with Ag and Au ions have proven unsuccessful.[19] Second, the size of the dopant plays a key role in the doping process. Finally, the surfactants and precursor molecules should not inhibit the initial interaction of the dopant with the surface of the growing nanocrystals. Failure to consider the aforementioned factors can lead to self purification processes in the host material, which expel the dopant from the nanocrystal, or result in a lack of overall adsorption of dopant to the QDs during growth. Various

methods can be used to characterize the extent of doping. The successful incorporation of the Mn^{2+} yields a redshifted emission peak (~581 nm) from the typical excitonic emission. Another powerful technique is electron paramagnetic resonance spectroscopy (EPR). It probes the magnetic ions and shows the effect of local environment on the spins of electrons. It establishes whether the dopant is fully incorporated in the crystal or reside on the surface of the QDs.[71] Additionally, trace metal ion analysis by inductively coupled plasma – optical mission spectroscopy (ICP-OES) is often carried out to determine the concentration of dopant in the host material after digestion.

1.7.3 Successive ionic layer adsorption and reaction (SILAR)

Surface passivation can improve the optoelectronic properties of QDs. Although precursor molecules and surface stabilizing ligands in the reaction mixture provide some surface stabilization, they can detach during washing and purification of the QDs in turn exposing surface defects such as vacancies and dangling bonds. [72] These defects result in the formation of trap states that inhibit normal emission processes by providing alternative pathways of thermal relaxation,[20] which are detrimental for generations of charge carriers. While surface passivation with additional ligands such as oleylamine and trioctylphosphine oxide might temporarily eliminate surface trap states, a more robust passivation is necessary to allow for reusability of the QDs.

Successive ionic layer adsorption and reaction (SILAR) is a method that allows for the growth of a shell on the nanocrystal one monolayer at a time.[72] Alternating anionic and cationic precursors, added to a solution containing the core QDs, passivate the surface and eliminate trap states. Zinc sulfide (ZnS) is a great candidate for surface passivation due to its thermal and chemical stability.[72] It has a larger band gap (~3.66 eV) than the CdS core (3.1 eV). ZnS does not participate in absorption and emission processes when irradiated with visible light and it confines

the charge carries in the core.[73] A precise control of the shell growth condition yields high quality QDs. However, a thick ZnS shell can dampen the quantum confinement effects and hinder the extraction of hot electrons. Finally, the shell thickness should not inhibit the escape of the hot electrons generated from the Auger process in the core. Previous studies reported that a shell of 2.5 to 5 monolayers[30] yields a well-passivated surface and an uninhibited Auger process.[74]

1.7.4 Motivation and outline

In Part I of this dissertation, we present the application of hot electrons generated via Mn-assisted Auger relaxation in doped QDs for photoreductive organic transformations. While Mn-doped QDs have been utilised in lasing and solar energy technologies, their role as heterogeneous photocatalysis remains largely unexplored. Chapter 2 summarizes the synthesis, characterization, and implementation of Mn^{2+} doped CdS/ZnS core/shell QDs as photocatalysts for proof-of-concept organic reactions. Chapter 3 presents the initial work on utilizing the QD photocatalyst film in a flow reactor setup with the potential of increased efficiency and scaleup; it is concluded with discussions on future directions and outlook. The work presented herein demonstrates the potential of doped QDs to rival undoped QDs and transition metal complexes in the field of organic photoredox catalysis.

1.8 References

1. Efros, A. L. & Brus, L. E. Nanocrystal Quantum Dots: From Discovery to Modern Development. *ACS Nano* vol. 15 6192–6210 (2021).
2. Bera, D., Qian, L., Tseng, T. K. & Holloway, P. H. Quantum dots and their multimodal applications: A review. *Materials (Basel).* **3**, 2260–2345 (2010).
3. Yang, X. & Wang, D. Photocatalysis: From Fundamental Principles to Materials and Applications. *ACS Appl. Energy Mater.* **1**, 6657–6693 (2018).
4. Lu, H. *et al.* Transforming energy using quantum dots. *Energy Environ. Sci.* **13**, 1347–1376 (2020).
5. Klimov, V. I. Multicarrier Interactions in Semiconductor Nanocrystals in Relation to the Phenomena of Auger Recombination and Carrier Multiplication. *Annu. Rev. Condens. Matter Phys.* **5**, 285–316 (2014).
6. Zhao, W. W., Wang, J., Zhu, Y. C., Xu, J. J. & Chen, H. Y. Quantum Dots: Electrochemiluminescent and Photoelectrochemical Bioanalysis. *Anal. Chem.* **87** 9520–9531 (2015).
7. Klimov, V. I. Spectral and dynamical properties of multiexcitons in semiconductor nanocrystals. *Annu. Rev. Phys. Chem.* **58**, 635–673 (2007).
8. Efros, A. L. *et al.* Evaluating the potential of using quantum dots for monitoring electrical signals in neurons. *Nature Nanotechnology* vol. 13 278–288 (2018).
9. Efros, A. L. Quantum dots realize their potential. *Nature* **575**, 604–605 (2019).
10. Beaulac, R., Ochsenbein, S. T. & Gamelin, D. R. *Colloidal transition-metal-doped quantum dots*. *Nanocrystal Quantum Dots, Second Edition* (2017) doi:10.1201/9781420079272.
11. Shu, Y. *et al.* Quantum Dots for Display Applications. *Angew. Chemie Int. Ed.* **59**, 22312–22323 (2020).
12. Giepmans, B. N. G., Adams, S. R., Ellisman, M. H. & Tsien, R. Y. The fluorescent toolbox for assessing protein location and function. *Science.* **312**, 217–224 (2006).
13. Banin, U. *et al.* Nanotechnology for catalysis and solar energy conversion. *Nanotechnology* **32**, 42003 (2020).
14. Mikulec, F. V. *et al.* Organometallic synthesis and spectroscopic characterization of manganese-doped CdSe nanocrystals. *J. Am. Chem. Soc.* **122**, 2532–2540 (2000).
15. Gaponenko, S. V. (Sergey V. . *Optical properties of semiconductor nanocrystals*. (Cambridge University Press, 1998).
16. Lim, J., Park, Y. S. & Klimov, V. I. Optical gain in colloidal quantum dots achieved with direct-current electrical pumping. *Nat. Mater.* **17**, 42–48 (2018).
17. Nozik, A. J. *Quantum dot solar cells*. *Physica E* vol. 14 www.elsevier.com/locate/physe

(2002).

18. Nozik, A. J. *Physical Chemistry of Semiconductor-Liquid Interfaces Ru 1diger Memming**. (1996).

19. Dabbousi, B. O. *et al.* (CdSe)ZnS core-shell quantum dots: Synthesis and characterization of a size series of highly luminescent nanocrystallites. *J. Phys. Chem. B* **101**, 9463–9475 (1997).

20. Mullaugh, K. M. & Luther, G. W. Spectroscopic determination of the size of cadmium sulfide nanoparticles formed under environmentally relevant conditions. *J. Environ. Monit.* **12**, 890–897 (2010).

21. Singhal, P. & Ghosh, H. N. Hot Charge Carriers in Quantum Dots: Generation, Relaxation, Extraction, and Applications. *ChemNanoMat* vol. 5 985–999 (2019).

22. Wang, L. W., Califano, M., Zunger, A. & Franceschetti, A. Pseudopotential Theory of Auger Processes in CdSe Quantum Dots. *Phys. Rev. Lett.* **91**, (2003).

23. Nag, A., Chakraborty, S. & Sarma, D. D. To dope Mn2+ in a semiconducting nanocrystal. *J. Am. Chem. Soc.* **130**, 10605–10611 (2008).

24. White, M. A., Weaver, A. L., Beaulac, R. & Gamelin, D. R. Electrochemically controlled Auger quenching of Mn2+ photoluminescence in doped semiconductor nanocrystals. *ACS Nano* **5**, 4158–4168 (2011).

25. Beaulac, R., Archer, P. I., Ochsenbein, S. T. & Gamelin, D. R. Mn2+-doped CdSe quantum dots: New inorganic materials for spin-electronics and spin-photonics. *Adv. Funct. Mater.* **18**, 3873–3891 (2008).

26. Banin, U. *et al.* Nanotechnology for catalysis and solar energy conversion. *Nanotechnology* vol. 32 (2020).

27. Singh, R., Liu, W., Lim, J., Robel, I. & Klimov, V. I. Hot-electron dynamics in quantum dots manipulated by spin-exchange Auger interactions. *Nat. Nanotechnol.* **14**, 1035–1041 (2019).

28. Norris, D. J., Efros, A. L. & Erwin, S. C. *Doped Nanocrystals*. http://science.sciencemag.org/ (2001).

29. Archer, P. I., Santangelo, S. A. & Gamelin, D. R. Inorganic cluster syntheses of TM2+-doped quantum dots (CdSe, CdS, CdSe/CdS): Physical property dependence on dopant locale. *J. Am. Chem. Soc.* **129**, 9808–9818 (2007).

30. Daniel Bryan, J. & Gamelin, D. R. *Doped Semiconductor Nanocrystals: Synthesis, Characterization, Physical Properties, and Applications Progress in Inorganic Chemistry*. vol. 54 (2005).

31. Fainblat, R. *et al.* Valence-band mixing effects in the upper-excited-state magneto-optical responses of colloidal Mn^{2+}-doped CdSe quantum dots. *ACS Nano* **8**, 12669–12675 (2014).

32. Bhargava, R. N., Gallagher, D., Hong, X. & Nurmikko, A. Optical properties of

manganese-doped nanocrystals of ZnS. *Phys. Rev. Lett.* **72**, 416–419 (1994).

33. Archer, P. I., Santangelo, S. A. & Gamelin, D. R. Direct observation of sp-d exchange interactions in colloidal Mn $^{2+}$ - And Co^{2+} -doped CdSe quantum dots. *Nano Lett.* **7**, 1037–1043 (2007).

34. Beaulac, R., Schneider, L., Archer, P. I., Bacher, G. & Gamelin, D. R. Light-induced spontaneous magnetization in doped colloidal quantum dots. *Science (80-.).* **325**, 973–976 (2009).

35. Barrows, C. J., Fainblat, R. & Gamelin, D. R. Excitonic Zeeman splittings in colloidal CdSe quantum dots doped with single magnetic impurities. *J. Mater. Chem. C* **5**, 5232–5238 (2017).

36. Beaulac, R., Archer, P. I., Ochsenbein, S. T. & Gamelin, D. R. Mn2+-doped CdSe quantum dots: New inorganic materials for spin-electronics and spin-photonics. *Adv. Funct. Mater.* **18**, 3873–3891 (2008).

37. Chen, H. Y., Chen, T. Y. & Son, D. H. Measurement of energy transfer time in colloidal Mn-doped semiconductor nanocrystals. *J. Phys. Chem. C* **114**, 4418–4423 (2010).

38. Xie, W. & Schlücker, S. Hot electron-induced reduction of small molecules on photorecycling metal surfaces. *Nat. Commun.* **6**, 1–6 (2015).

39. Livache, C. *et al.* High-efficiency photoemission from magnetically doped quantum dots driven by multi-step spin-exchange Auger ionization. *Nat. Photonics* **16**, 433–440 (2022).

40. Barrows, C. J. *et al.* Electrical Detection of Quantum Dot Hot Electrons Generated via a Mn2+-Enhanced Auger Process. *J. Phys. Chem. Lett.* **8**, 126–130 (2017).

41. Chen, H. Y. *et al.* Hot electrons from consecutive exciton - Mn energy transfer in Mn-doped semiconductor nanocrystals. *J. Phys. Chem. C* **115**, 11407–11412 (2011).

42. Shaw, M. H., Twilton, J. & MacMillan, D. W. C. Photoredox Catalysis in Organic Chemistry. *Journal of Organic Chemistry* vol. 81 6898–6926 (2016).

43. Wang, D. Y., Yin, Y. Y., Feng, C. W., Rukhsana & Shen, Y. M. Advances in homogeneous photocatalytic organic synthesis with colloidal quantum dots. *Catalysts* **11**, 1–14 (2021).

44. Marzo, L., Pagire, S. K., Reiser, O. & König, B. Photokatalyse mit sichtbarem Licht: Welche Bedeutung hat sie für die organische Synthese? *Angew. Chemie* **130**, 10188–10228 (2018).

45. Lettieri, S., Pavone, M., Fioravanti, A., Santamaria Amato, L. & Maddalena, P. Charge Carrier Processes and Optical Properties in TiO(2) and TiO(2)-Based Heterojunction Photocatalysts: A Review. *Mater. (Basel, Switzerland)* **14**, (2021).

46. Clarizia, L. *et al.* Effect of surface properties of copper-modified commercial titanium dioxide photocatalysts on hydrogen production through photoreforming of alcohols. *Int. J. Hydrogen Energy* **42**, 28349–28362 (2017).

47. Fujishima, A., Zhang, X. & Tryk, D. A. TiO2 photocatalysis and related surface

phenomena. *Surf. Sci. Rep.* **63**, 515–582 (2008).

48. Lazar, M. A., Varghese, S. & Nair, S. S. Photocatalytic Water Treatment by Titanium Dioxide: Recent Updates. *Catalysts* vol. 2 572–601 (2012).

49. Wang, Q. & Domen, K. Particulate Photocatalysts for Light-Driven Water Splitting: Mechanisms, Challenges, and Design Strategies. *Chem. Rev.* **120**, 919–985 (2020).

50. Ma, Y. *et al.* Titanium Dioxide-Based Nanomaterials for Photocatalytic Fuel Generations. *Chem. Rev.* **114**, 9987–10043 (2014).

51. Ijaz, M. & Zafar, M. Titanium dioxide nanostructures as efficient photocatalyst: Progress, challenges and perspective. *Int. J. Energy Res.* **45**, 3569–3589 (2021).

52. Thelakkat, M., Schmitz, C. & Schmidt, H.-W. Fully Vapor-Deposited Thin-Layer Titanium Dioxide Solar Cells. *Adv. Mater.* **14**, 577–581 (2002).

53. Habisreutinger, S. N., Schmidt-Mende, L. & Stolarczyk, J. K. Photocatalytic Reduction of CO2 on TiO2 and Other Semiconductors. *Angew. Chemie Int. Ed.* **52**, 7372–7408 (2013).

54. Yang, M.-C., Yang, T.-S. & Wong, M.-S. Nitrogen-doped titanium oxide films as visible light photocatalyst by vapor deposition. *Thin Solid Films* **469**–**470**, 1–5 (2004).

55. Dong, H. *et al.* An overview on limitations of TiO2-based particles for photocatalytic degradation of organic pollutants and the corresponding countermeasures. *Water Res.* **79**, 128–146 (2015).

56. Caputo, J. A. *et al.* General and Efficient C-C Bond Forming Photoredox Catalysis with Semiconductor Quantum Dots. *J. Am. Chem. Soc.* **139**, 4250–4253 (2017).

57. Prier, C. K., Rankic, D. A. & MacMillan, D. W. C. Visible light photoredox catalysis with transition metal complexes: Applications in organic synthesis. *Chemical Reviews* vol. 113 5322–5363 (2013).

58. Pitre, S. P., McTiernan, C. D. & Scaiano, J. C. Understanding the Kinetics and Spectroscopy of Photoredox Catalysis and Transition-Metal-Free Alternatives. *Acc. Chem. Res.* **49**, 1320–1330 (2016).

59. Hofbeck, T. & Yersin, H. The Triplet State of fac-Ir(ppy)3. *Inorg. Chem.* **49**, 9290–9299 (2010).

60. Skubi, K. L., Blum, T. R. & Yoon, T. P. Dual Catalysis Strategies in Photochemical Synthesis. *Chem. Rev.* **116**, 10035–10074 (2016).

61. Reckenthäler, M. & Griesbeck, A. G. Photoredox Catalysis for Organic Syntheses. *Adv. Synth. Catal.* **355**, 2727–2744 (2013).

62. Shaw, M. H., Twilton, J. & MacMillan, D. W. C. Photoredox Catalysis in Organic Chemistry. *J. Org. Chem.* **81**, 6898–6926 (2016).

63. Eplý, F. T. Photoredox Catalysis by [Ru (bpy) 3] 2 + to Trigger Transformations of Organic Molecules Using Visible-light photocatalysis and its 20th Century Roots.**76**, 859–917 (2011).

64. Efros, A. L. *et al.* Evaluating the potential of using quantum dots for monitoring electrical signals in neurons. *Nat. Nanotechnol.* **13**, 278–288 (2018).

65. Gao, Y.-J. *et al.* Exceptional Catalytic Nature of Quantum Dots for Photocatalytic Hydrogen Evolution without External Cocatalysts. *Adv. Funct. Mater.* **28**, 1801769 (2018).

66. Jiang, Y., Wang, C., Rogers, C. R., Kodaimati, M. S. & Weiss, E. A. Regio- and diastereoselective intermolecular [2+2] cycloadditions photocatalysed by quantum dots. *Nat. Chem.* **11**, 1034–1040 (2019).

67. Jiang, Y. & Weiss, E. A. Colloidal Quantum Dots as Photocatalysts for Triplet Excited State Reactions of Organic Molecules. *J. Am. Chem. Soc.* **142**, 15219–15229 (2020).

68. Mikulec, F. V. *et al.* Organometallic synthesis and spectroscopic characterization of manganese-doped CdSe nanocrystals. *J. Am. Chem. Soc.* **122**, 2532–2540 (2000).

69. Yang, Y., Chen, O., Angerhofer, A. & Cao, Y. C. On doping CdS/ZnS core/shell nanocrystals with Mn. *J. Am. Chem. Soc.* **130**, 15649–15661 (2008).

70. Landry, M. L., Morrell, T. E., Karagounis, T. K., Hsia, C. H. & Wang, C. Y. Simple syntheses of CdSe quantum dots. *J. Chem. Educ.* **91**, 274–279 (2014).

71. Hills, M. E., Harris, D. C. & Lowe-Ma, C. K. Zinc aluminum sulfide: Electron paramagnetic resonance spectroscopy and infrared transmittance. *J. Phys. Chem. Solids* **48**, 501–507 (1987).

72. Li, J. J. *et al.* Large-scale synthesis of nearly monodisperse CdSe/CdS core/shell nanocrystals using air-stable reagents via successive ion layer adsorption and reaction. *J. Am. Chem. Soc.* **125**, 12567–12575 (2003).

73. Yu, W. W. & Peng, X. Formation of high-quality CdS and other II-VI semiconductor nanocrystals in noncoordinating solvents: Tunable reactivity of monomers. *Angew. Chemie - Int. Ed.* **41**, 2368–2371 (2002).

74. Grimaldi, G. *et al.* Spectroscopic Evidence for the Contribution of Holes to the Bleach of Cd-Chalcogenide Quantum Dots. *Nano Lett.* **19**, 3002–3010 (2019).

Chapter 2 - Mn(II)-doped CdS/ZnS Core/shell Quantum Dot Films Photocatalyze Reductive Organic Transformations With a Boost in Efficiency From Enhanced Auger Processes

(This chapter is adapted from Brian Malile, Rana Sodhi, and Jennifer I. L. Chen. *J. Mater. Chem. A* **10**, 25319–25328 (2022). Reproduced from Ref. 1 with permission from the Royal Society of Chemistry.)

(All experiments in this chapter were performed by Brian Malile, with the exception of XPS which was performed by Dr. Rana Sodhi.)

2.1 Abstract

We investigated the reduction of organic compounds photocatalyzed by Mn^{2+}-doped CdS/ZnS quantum dot (Mn:CdS/ZnS QD) films. The incorporation of Mn^{2+} ion into the CdS nanocrystals as a dopant promotes Auger cross-relaxation, a phenomenon that yields hot electrons with high reducing power. Using QD-coated vessels or substrates, we examined several model organic reactions to establish the versatility and superior performance of Mn:CdS/ZnS QDs over undoped CdS QDs. First, Mn:CdS/ZnS QDs exhibited a 3.4-fold increase in the photoreduction of methyl viologen compared with CdS QDs. Second, the viologen can subsequently be utilized as electron shuttle in biphasic reactions, such as the photoreduction of meso-stilbene dibromide, allowing for flexible design where reactants were separate from the photocatalysts. Third, Mn:CdS/ZnS QDs photocatalyzed the 6-electron reduction of nitrobenzene to aniline with an overall internal quantum efficiency of ~3 %. Impressively, the photoreduction of nitrobenzene was complete in 15 min by doped QDs vs >48 h for undoped QD – an enhancement of >190-fold. Moreover, we investigated the recyclability of the Mn:CdS/ZnS film and detected changes in the surface species, indicating some oxidation of the film upon its use as photocatalyst. Different from previous works, the QD films and coatings facilitate the rapid separation of catalysts from solution and significantly reduce

post-reaction workups. Our work demonstrates a drastic improvement in the efficiency of CdS QD-based photocatalysis that may find broad implications in photoredox reactions.

2.2 Introduction

Semiconducting nanocrystals with sizes smaller than the exciton Bohr radius, known as quantum dots (QDs), are emerging catalysts for photoredox reactions.[2] These reactions are traditionally performed using expensive iridium and ruthenium complexes. Contrary to molecular catalysts, QDs exhibit desirable properties such as tunable reduction and oxidation potentials, long-lived excited states, and broad absorption spectra,[3–5] which can be achieved by controlling the size and surface chemistry. Importantly, an individual QD can provide numerous reaction sites and facilitate multielectron reduction processes,[6] and QD catalyst loadings down to 0.0001 mol% have yielded promising turnover numbers.[7] Previous work on photocatalysis with QDs have mainly focused on CdS for hydrogen production,[8] small molecule activation,[9] C-C bond coupling,[10] and functional group reduction.[11] On the other hand, challenges for retaining stable and efficient QDs for photocatalytic reactions remain; there is a need to optimize sacrificial agents, shorten reaction times, and reduce surface recombination of charge carriers.[12] Besides size control, the introduction of dopants into QDs can lead to new or enhanced photophysical properties. For example, Mn^{2+}-doping in QDs lead to enhanced Auger processes that generate hot electrons with increased reductive power.

Auger cross-relaxation is a nonradiative event where the energy from the annihilation of an exciton transfers to a second electron in the conduction band (CB), making it a hot electron.[13] The probability of this process is enhanced in QDs compared with bulk material because quantum confinement promotes the interaction between charge carriers and conservation rules on

momentum are relaxed such that only energy needs to be conserved.[13,14] Auger cross-relaxation is further enhanced in Mn-doped QDs because the Mn^{2+} ion serves as an intermediate, highly localized energy storage site. Mn^{2+} has a long-lived excited state (~millisecond for $^4T_1$, the lowest excited state in a tetrahedral weak ligand field) that increases the probability of Auger-type energy transfer from Mn^* to a conduction band electron.[15,16] Notably, in Mn-doped QDs, hot electrons having ~2.1 eV excess energy can be generated under light intensity comparable to the solar irradiation, where the exciton-to-Mn energy transfer from the first photon absorption can be given to an electron created by a second photon absorption. The spin-exchange interactions between the magnetic dopant (Mn^{2+}) and host material (CdS) dramatically enhance the Auger process such that the Mn^{2+}-assisted energy transfer to conduction band electrons outcompetes the intraband cooling, in turn increasing the number of hot carriers.[17,18] The properties of the hot electrons were investigated photoelectrochemically and in solid-state device studies. Injected electrons quenched the Mn^{2+} photoluminescence and the resultant hot electrons crossed blocking layers having empty states higher in energy than the conduction band of the QD semiconductor .[15,16,19] The hot electrons from Mn-doped QDs, are much higher in energy than those from plasmonic nanoparticles, even approaching the vacuum level.[18,20] Therefore, harnessing hot electrons from Mn-doped QDs may facilitate reactions previously unfeasible under mild conditions. On the other hand, the use of hot electrons from Mn-doped QDs for chemical transformation has focused on solar-related applications[21] such as water splitting[22,23] and CO_2 reduction.[24] It has been found that Mn-doped QDs exhibited up to 7-fold enhancements compared with undoped dots for H_2 production[25], and that electron transfer from Mn-doped QDs can occur at a long range yielding different selectivity and product yields.[26] Motivated by an increasing interest in developing QDs as efficient

heterogeneous catalysts, we set out to investigate Mn-doped QDs as photocatalysts for organic transformations, which has not been reported to date.

Herein, we investigated Mn^{2+}-doped CdS/ZnS core/shell QDs (denoted as Mn:CdS/ZnS or doped QDs) as photoredox catalysts for model organic reactions. We examined three reactions and compared the performance of doped QDs with the undoped (CdS) QDs: 1) photoreduction of methyl viologen; 2) dehalogenation of meso-1,2-dibromo-1,2-diphenylethane; and 3) photoreduction of nitrobenzene to aniline. Different from existing works of QD-catalyzed organic transformations, we implemented the QDs as films and coatings directly on the reaction vessels. The film setup permits the facile removal and recycling of the QD photocatalysts from the reaction mixture and their use in various types of solvents. In addition to demonstrating the superior photocatalytic capabilities of Mn:CdS/ZnS QDs, we show that the film setup enables efficient post-reaction workup without laborious purification to separate the catalysts, thereby overcoming the drawback of colloidal-based suspensions. Our work opens the door for the wider exploration of Mn-doped QDs for use in synthetic and process chemistry where catalyst-coated reaction vessels may be of interest.

2.3 Results and Discussion

2.3.1 Supported Mn-doped CdS/ZnS QD film as photocatalysts

Figure 2.1 illustrates the QD-coated system (left), the photophysical processes that generate the hot electrons upon light excitation (centre), and the reactions examined (right). Blue light irradiation creates an exciton, the energy of which rapidly transfers to the Mn^{2+} ion resulting in the $^4T_1$ excited state.[27] Because of the long-lived excited Mn^{2+} state, non-radiative Auger cross-relaxation occurs with high probability when additional conduction electrons are present, leading

to hot electron generation.[15] The cross-linked QDs in a film further promotes the Auger process due to the interparticle shuttling of the excited electrons prior to radiative relaxation.[28] The photogenerated electrons were exploited for three model reactions (Figure 2.1, right) to elucidate the reducing capabilities of the doped vs undoped QDs.

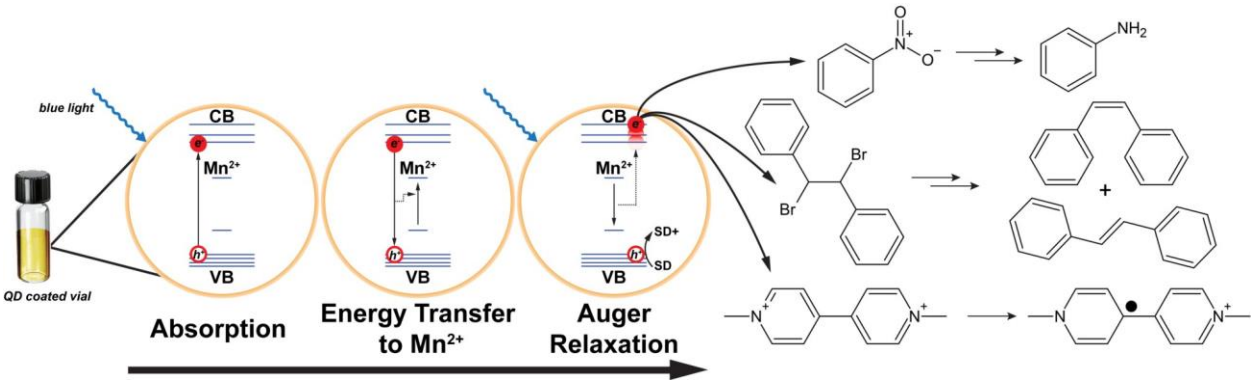

Figure 2.1. Mn^{2+}-assisted Auger relaxation generates hot electrons that are be harvested for photoreduction reactions. The electron and hole transfer to the organic substrate and sacrificial donor (SD), respectively.

To study heterogeneous photocatalytic reactions, we incorporated Mn:CdS/ZnS core/shell QDs as films on glass to simplify the post-reaction recovery of photocatalysts by eliminating the need to separate the QDs via multiple rounds of centrifugation. The Mn:CdS/ZnS QDs were synthesized by a previously established hot-injection method[15] and subsequently capped with 2-monolayers of ZnS shell and terminated with a Zn^{2+} layer. The undoped CdS/ZnS QDs were synthesized similarly without the Mn precursor. We installed a thin ZnS shell to passivate surface trap states[29] while allowing carriers to tunnel through. Without ZnS shell, the energy transfer to the Mn^{2+} ion in the doped QDs was impeded by nonradiative recombination pathways of the trap states. Figure 2.2 shows PL spectra of as-synthesized doped and undoped CdS core QDs with increasing number of monolayers of ZnS shell. The increase in PL of the QDs with increasing number of ZnS layers suggests successful passivation.

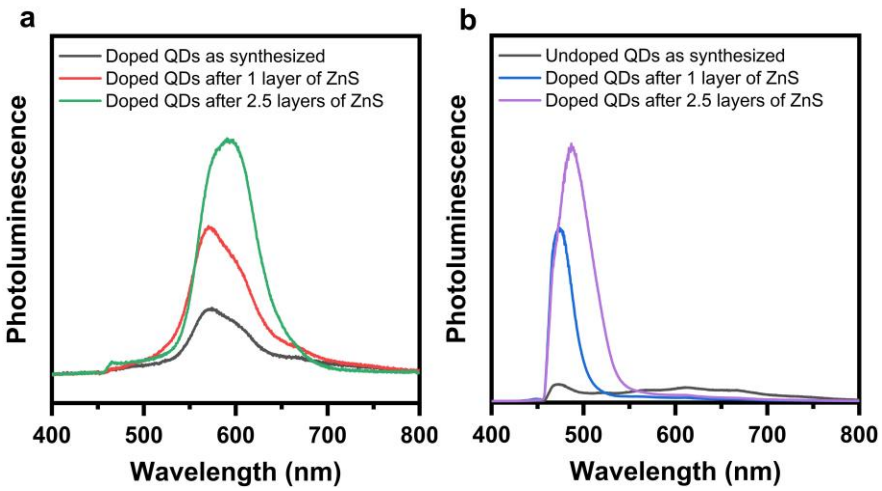

Figure 2.2. Photoluminescence spectra of during the passivation of Mn^{2+} doped CdS QDs (A) and undoped CdS QDs (B) with ZnS. Increasing number of layers of ZnS increases PL. Spectra collected under 440 nm excitation and with a 460-nm long pass filter.

The purified QDs were immobilized on glass vessels (e.g., slides or vials) via evaporation-assisted deposition and then cross-linked with heptanediamine to yield mechanically stable films. The molar ratio of Mn to Cd was determined to be 0.0171±0.0002:1 by Inductively Coupled Plasma Optical Emission Spectroscopy (ICP-OES, see Appendix A2). Figure 2.3 summarizes the characterizations of Mn:CdS/ZnS QDs confirming the successful incorporation of Mn^{2+}. Figure 2.3A shows the absorbance and photoluminescence (PL) spectra of the doped and undoped QDs. The doped and undoped QDs have near identical absorption spectra indicating similar nanocrystal size, however, their PL properties differ. The undoped QDs display the excitonic emission at 488 nm compared with the doped QDs which exhibit PL at 581 nm. The new PL at 581 nm with a lifetime of 1.9 ms (Figure 2.4) corresponds to the $^4T_1 \rightarrow {}^6A_1$ transition of the Mn^{2+} dopant in a tetrahedral ligand field, which is lower in energy compared to the free-ion energy transition ($^4G \rightarrow {}^6S$) of Mn^{2+} due to the ligand field splitting of 3d orbitals into t_2 and e terms.[30] The quenching of the excitonic emission in doped QDs provides evidence of the incorporation of Mn^{2+} into the CdS lattice. The doping of Mn^{2+} in the QDs was further confirmed by Electron Paramagnetic

Resonance (EPR) spectroscopy (Figure 2.3B). The presence of six strong lines corresponds to the hyperfine nuclear coupling to Mn^{2+} (I=5/2), and the hyperfine splitting parameter A calculated from the EPR spectrum (65.1×10^{-4} cm^{-1}) is in line with Mn^{2+} in bulk CdS in a tetrahedral geometry.[31,32] In contrast, a surface Mn^{2+} ion has a much higher hyperfine splitting parameter.[33] Figure 2.3C shows the powder X-ray diffraction (PXRD) spectrum of the doped QDs (black

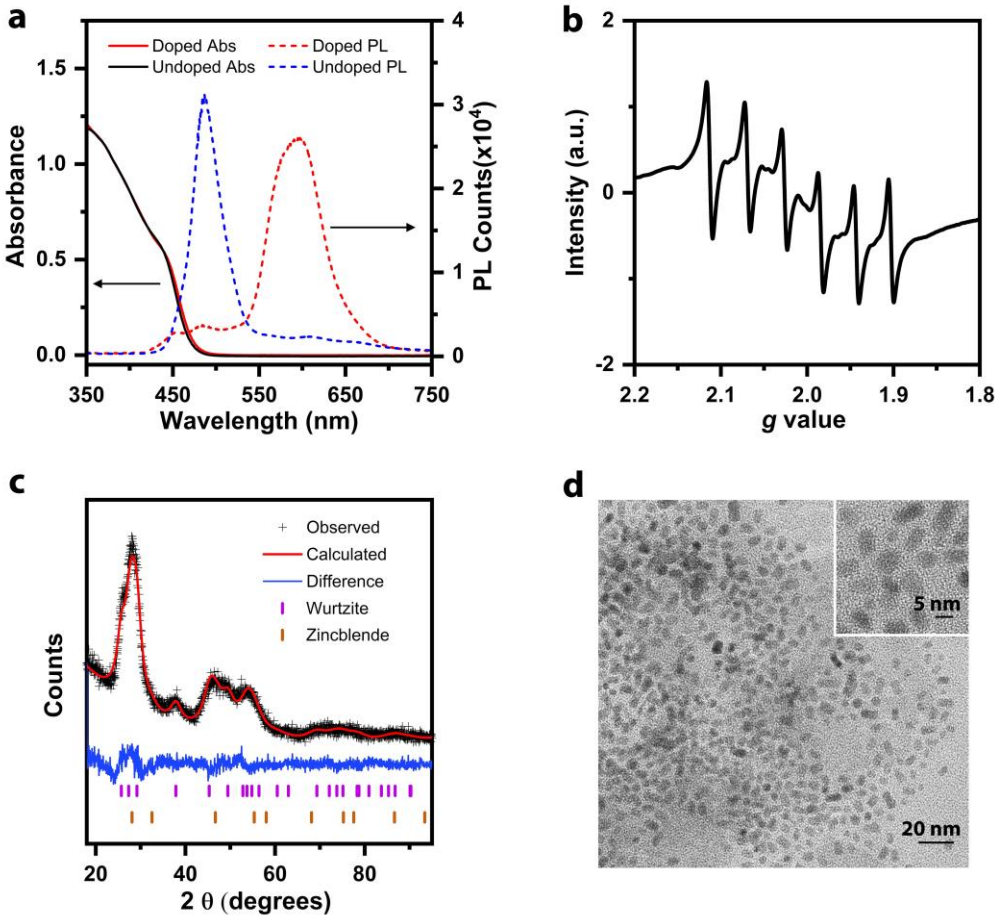

Figure 2.3. Characterizations of Mn^{2+}:CdS/ZnS QDs. (A) Absorbance (solid lines) and photoluminescence spectra (dashed lines) of doped Mn^{2+}:CdS/ZnS (red) and undoped CdS/ZnS (blue) QDs in toluene. (B) EPR spectrum of Mn^{2+}:CdS/ZnS with six lines resulting from energy splitting due to Mn^{2+} I=5/2. (C) PXRD of doped QDs (experimental in black, calculated in red, and residual difference in blue). Phase analysis results in 55 wt% wurtzite and 45 wt% zinc blende. (D) TEM images of Mn^{2+}:CdS/ZnS QDs.

symbols) and the fit from Rietveld refinement (red line) indicating 45 wt% zinc blende and 55 wt% wurtzite phases.[34,35] The average QD size as imaged by TEM (Figure 2.3D) is 5.6 ± 0.6 nm. The overall composition and size agree with the core/shell structure of the QDs, where the core Mn:CdS (wurtzite) is 4.5 nm in diameter based on excitonic absorption,[36] and the ZnS shell (zinc blende) is theoretically 0.7 nm in thickness (see Appendix A1). The elongated structure observed

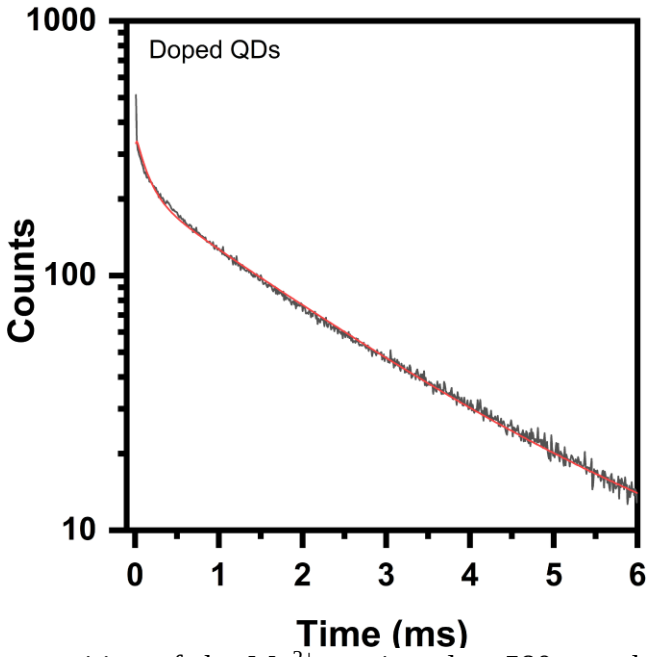

Figure 2.4. $^4T_1 \rightarrow {}^6A_1$ transition of the Mn^{2+} monitored at 580 nm showing the long-lived PL (black) as a double exponential fit (red) with components $\tau_1 = 0.141$ ms , and $\tau_2 = 1.91$ ms.

in the TEM images were reported previously and suggested to result from the experimental conditions during shell growth. Stacking faults, specifically during the addition of the zinc precursor, lead to preferential elongation along the [002] direction.[37,38]

2.3.2 Photoreduction of viologens

We first investigated the photoreduction of methyl viologen (MV^{2+}) by the doped and undoped QDs. QD films on glass slides were placed in a 500 µM aqueous solution of methyl viologen. We determined the amount of QDs in the film by redispersing the uncross-linked QDs

in toluene and measuring the solution absorbance. Methyl viologen is an electron acceptor and has a reduction potential of -0.446 V vs NHE, which is below the conduction band energy of the QDs (see Figure 2.5). A single electron reduction of MV^{2+} leads to the singly charged radical $MV^{+\bullet}$, which absorbs at 396 and 605 nm. The appearance of the blue color in the viologen solution comes solely from the reduced species, contrary to a previous study that employed methylene blue,[46] where a decrease in the absorbance can arise from photoreduction as well as oxidative decomposition of the dye. Figure 2.6A shows the evolution of absorption spectra of the viologen

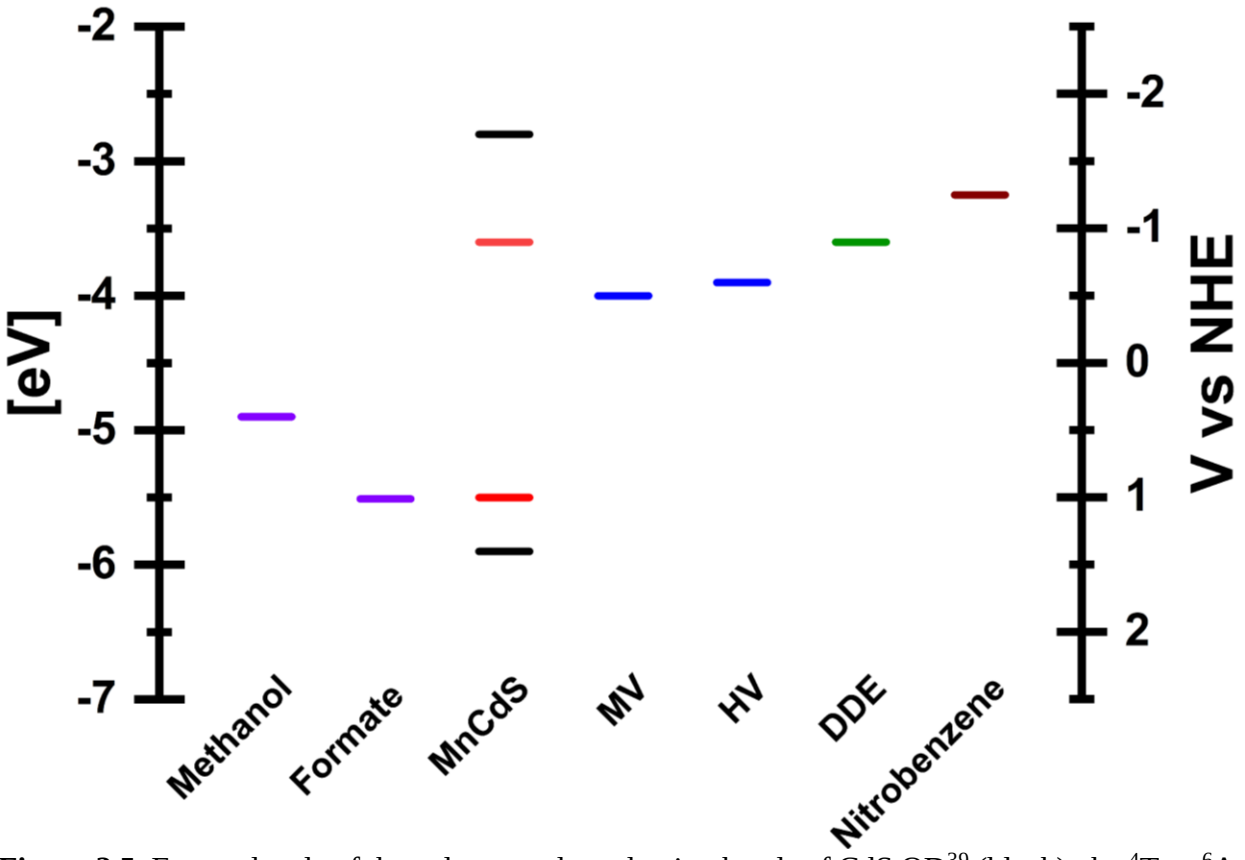

Figure 2.5. Energy levels of the valence and conduction bands of CdS QD[39] (black), the $^4T_1 \rightarrow {}^6A_1$ transition of the high spin Mn^{2+} in a tetrahedral geometry[30] (red), the oxidation potentials of sacrificial hole scavengers[40,41] (purple) and reduction potentials of viologens[42] (blue), meso-1,1-dibromo-1,2-diphenylethane[43,44] (green) and nitrobenzene[45] (brown).

upon irradiation at 440 nm in the presence of doped vs undoped QD films with MeOH as the sacrificial electron donor. The absorption of the viologen radial does not overlap with the incident irradiation at 440 nm and thus has no effect on the absorbance of QDs. In heterogenous photocatalysis, the escape of charge carriers during the photoredox process deteriorates subsequent absorption and emission events, hence the presence of a sacrificial agent is crucial.[22,47] Figure 2.6B summarizes the temporal concentration of $MV^{+\bullet}$ based on the absorbance and molar absorption coefficient at 396 nm for three trials. By considering the reaction as pseudo-first order, we obtained rate constants of $1.12x10^{-3}$ and $3.31x10^{-4}$ s^{-1} for doped and undoped QDs, respectively. This corresponds to a 3.4-fold enhancement on the rate of photoreduction of MV^{2+} by doped QDs vs undoped QDs. We note that the excitation intensity we employed (85 mW/cm^2) was above the threshold at which the PL intensity of Mn^{2+} deviates from linear dependence on power (Figure 2.7).

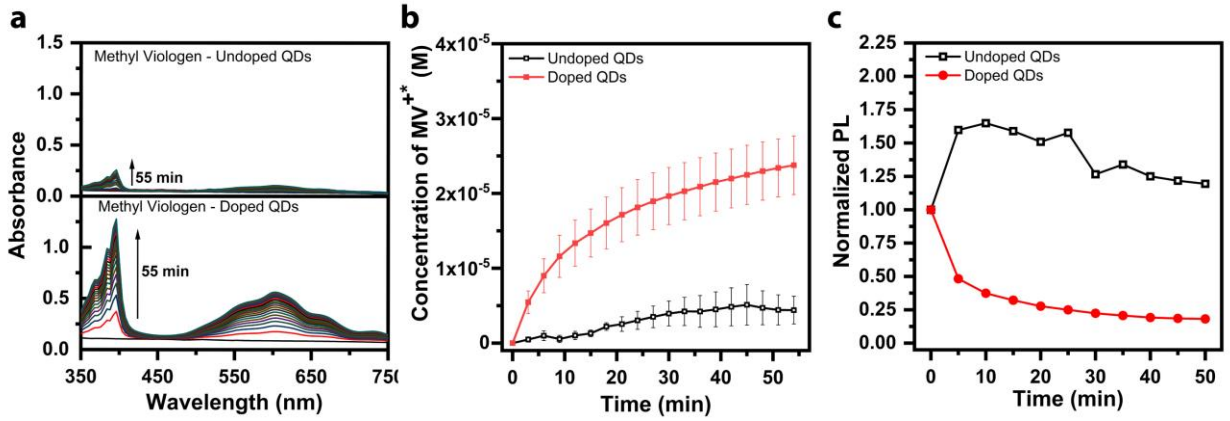

Figure 2.6. Reduction of methyl viologen (MV^{2+}) to MV^{*+} by QDs. (A) UV-Vis spectral evolution over time showing the formation of the charged radical ($MV^{+\bullet}$) in the presence of doped QDs (bottom) and undoped QDs (top) under 440 nm irradiation with methanol as sacrificial electron donor. (B) Amount of $MV^{+\bullet}$ generated over the course of 55-min irradiation with doped (red) and undoped (black) QDs. Error bars are standard deviations. (C) Normalized photoluminescence (PL) intensity at 488 nm for the undoped QDs (black) and at 581 nm for the doped QDs (red) in the presence of MV^{2+} and methanol vs irradiation time.

At this irradiation intensity, each QD was excited by 7400 photons per second, with 1 exciton produced per 0.36 ms (see Appendix A1). Thus, Mn^{2+} states were saturated and Auger cross-relaxation was feasible.[16] We determined an internal quantum efficiency (IQE) of 2.9 % for the doped QDs for the photoreduction of MV^{2+}. Additionally, we monitored the changes in the PL intensity of the doped and undoped QDs in the presence of MV^{2+}. Figure 2.6C shows a small decay in the PL of the undoped QDs (after an initial rise due to photoannealing), compared with an exponential-like decay (up to 75% attenuation) for the doped QDs. The significant bleach in the PL of the doped QDs in the presence of MV^{2+} corroborates the consumption of the photogenerated electrons and the efficient transfer of hot electrons from Mn:CdS/ZnS QDs. On the other hand, we observed a negligible decrease of PL of the undoped QDs and only a small PL decay for the doped

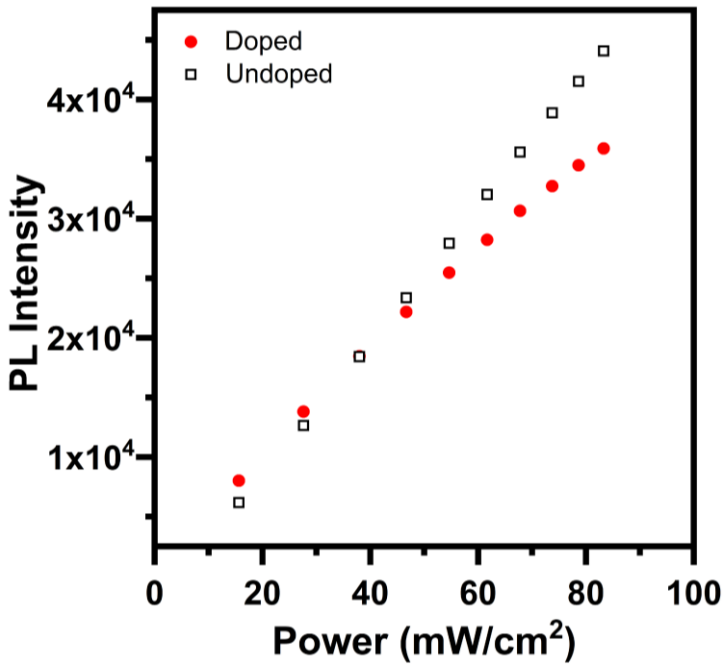

Figure 2.7. Photoluminescence intensity of doped (red) and undoped (black) QDs versus irradiation power at 440 nm. Deviation of PL intensity of the doped QDs from linear relationship at higher power suggests saturation of Mn^{2+} states and nonradiative Auger processes.

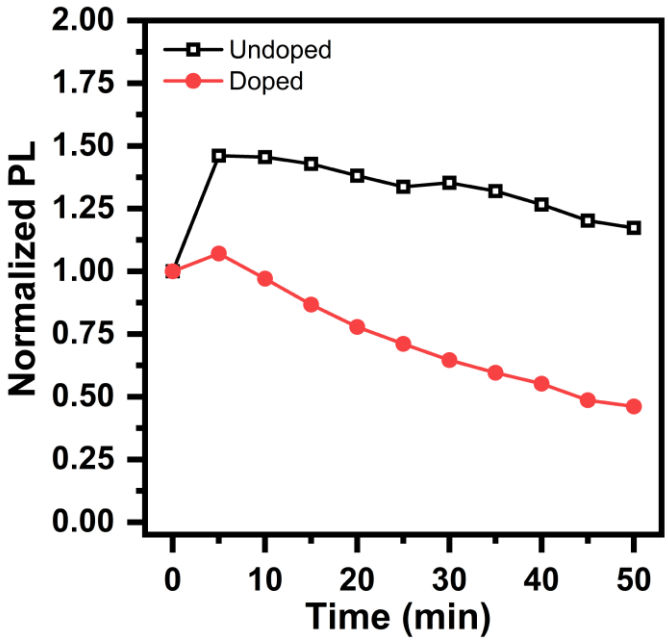

Figure 2.8. Normalized photoluminescence intensity at 488 nm and 581 nm for the undoped (black) and doped QDs (red), respectively, in water.

QDs without MV^{2+} in water (Figure 2.8). Doped QDs still exhibited a small PL decay in the absence of MV^{2+} because water is a weak electron acceptor and has been shown to be reduced to H_2 by the hot electrons of doped QDs.[25] The negligible change in the PL of the undoped dots with or without MV^{2+} indicates inefficient transfer of photoexcited electrons due to short exciton lifetime even though energetically there is no barrier. Control experiments, including in the absence of light or in the absence of QDs, showed no reaction of the MV^{2+} (Figure 2.9). Besides the direct photoreduction of MV^{2+} by hot electrons in Mn:CdS/ZnS QDs, other reactive pathways involving MeOH are possible because oxidation of methanol by holes yields radicals ($\bullet CH_2OH$ and $\bullet CO_2^-$) and H_2,[48,49] which can also reduce MV^{2+}. The results nevertheless demonstrate the enhanced photoreduction capability of Mn:CdS/ZnS, in line with previous reports.[25]

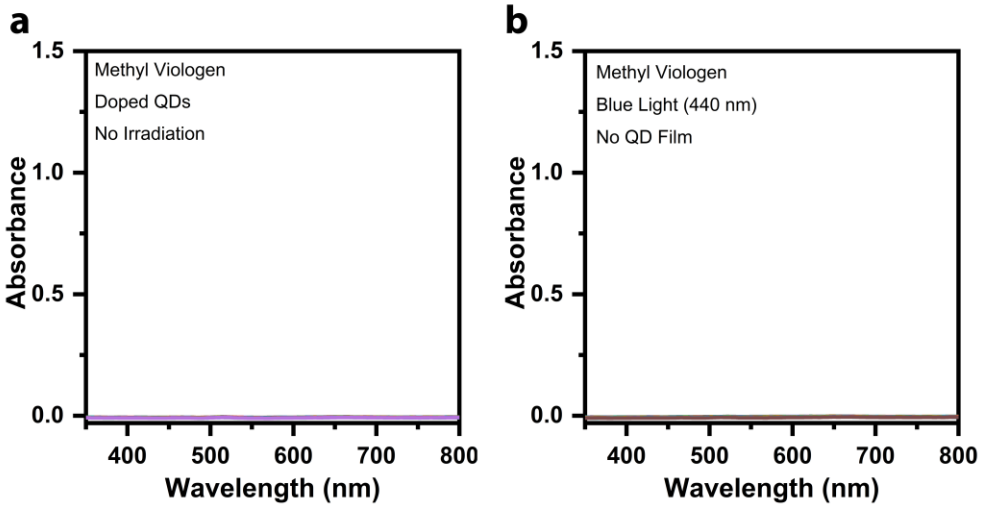

Figure 2.9. Control experiments with MV^{2+} in water show that both light and QDs are crucial for reaction to take place: (A) Spectra of solution without irradiation; and (B) spectra of solution without QDs upon blue light irradiation.

2.3.3 Photoreduction of meso-1,2- dibromo-1,2-diphenylethane

Viologens are electron transfer agents with stable redox-active states and tunable nitrogen substituents. Various viologens, with octyl and heptyl substituents, undergo a change in solubility upon a single electron reduction and can act as electron shuttles between aqueous and nonaqueous phases,[50] Hence, we next explored a biphasic system incorporating heptyl viologen as the electron shuttle. The ability to separate the reactant from the photocatalyst, as in a biphasic system with a well characterised electron shuttle, can overcome the detrimental adsorption and accumulation of reactants on the reactive sites of the QDs. We show the versatility of the QD films in biphasic systems with the dehalogenation of meso-1,2-dibromo-1,2-diphenylethane (DDE). Figure 2.10 shows the reaction mechanism for the dehalogenation reaction where the QDs replace the conventional Ru photocatalysts,[51–53] The catalytic cycle starts with the photoexcitation of QDs and the reduction of heptyl viologen (HV^{2+}) in the aqueous phase (step 1). Upon single electron reduction, the hydrophobicity of the heptyl viologen increases leading to its phase-transfer to the

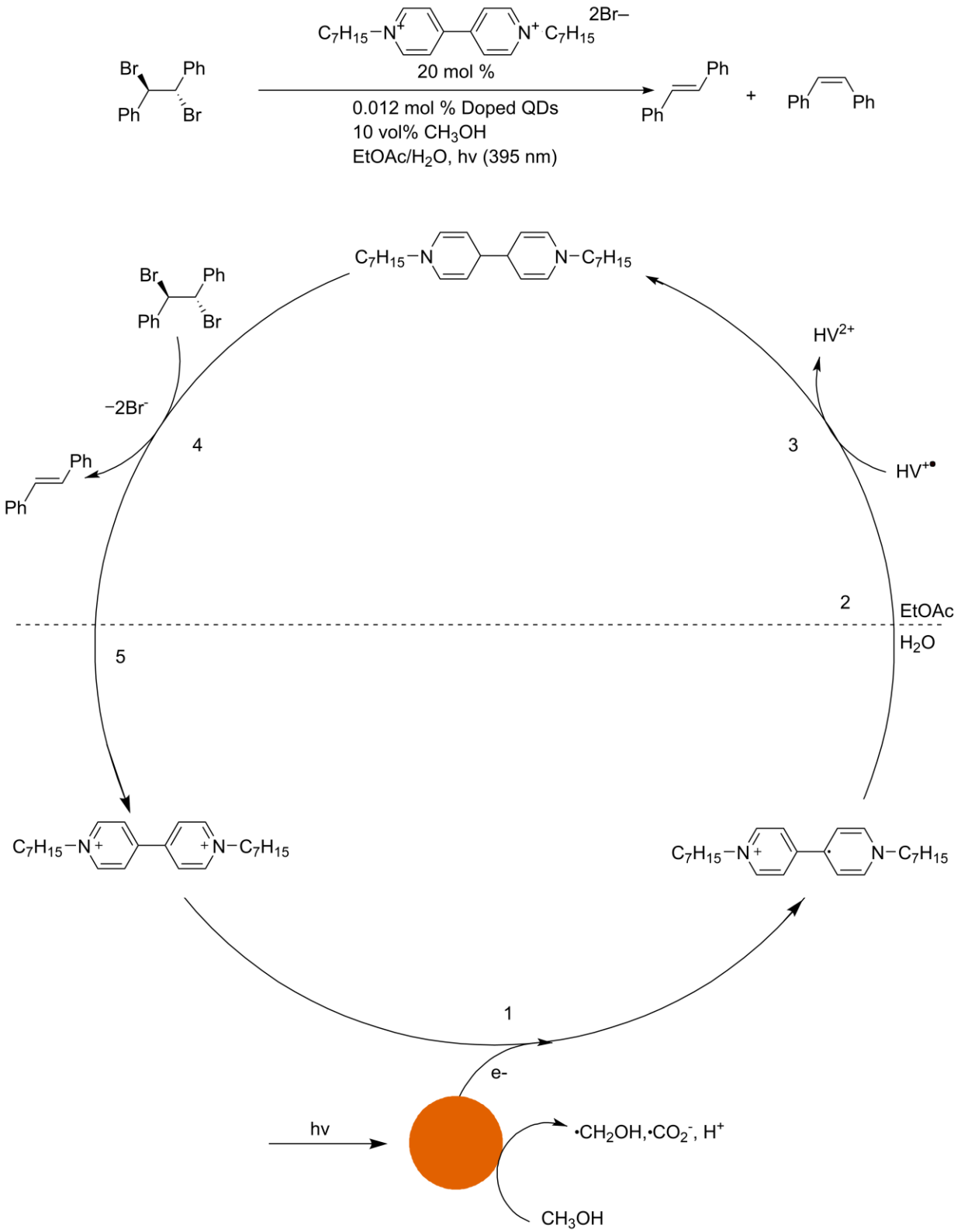

Figure 2.10. Debromination of DDE with doped QDs as photocatalyst in a biphasic system (H_2O/EtOAc).

ethyl acetate layer (step 2). Disproportionation (step 3) then produces a doubly reduced viologen (HV^0) and HV^{2+} from two singly reduced charged radicals (HV^{*+}). HV^0 eliminates the vicinal bromides in a two-electron reduction route forming *trans*-stilbene or *cis*-stilbene (step 4) and HV^{2+} is recycled back to the aqueous phase (step 5).

The biphasic dehalogenation reaction of DDE can be monitored via UV-vis spectroscopy. Figure 2.11A shows the UV-vis spectra of the organic layer from a sample containing doped QD film (in the aqueous phase) irradiated at 395 nm (150 mW/cm^2) for 24 h, with and without methanol (blue and red, respectively) versus that of a control in the dark (black). The vanishing peak of the reactant at 260 nm and the evolution of a broad peak with a maximum at 294 nm

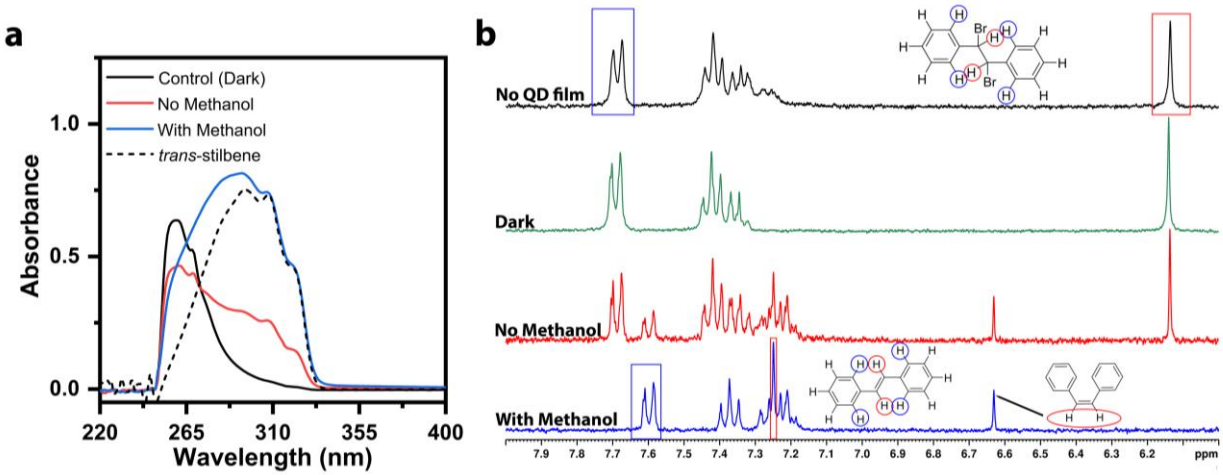

Figure 2.11. (A) UV-Vis spectra of the organic layer of the dehalogenation reaction of *meso*-1,2-dibromo-1,2-diphenylethane (DDE) in a biphasic system (H_2O/EtOAc), with heptyl viologen as an electron shuttle and methanol as a sacrificial agent under 395 nm irradiation, with (blue) and without methanol (red). Control reaction without irradiation shown in black. Spectrum of pure *trans*-stilbene shown illustrated with dashed lines. (B) ^{1}H NMR spectra for monitoring the reaction progress. An up-field shift in the doublets at 7.70-7.68 ppm to the doublets at 7.61-7.59 ppm shows the conversion of DDE to stilbene. NMR spectra of reactions 6, 3, 2 and 1 listed in Table 1 are shown as black, green, red, and blue trace in (B).

indicates the formation of stilbene where the redshift of the product peak results from the expanded conjugation upon dehalogenation. The broad peak width, compared to the reference spectrum of pure *trans*- stilbene (dashed line) suggests the presence of the cis-isomer as well. *Trans and cis*-stilbene exhibit absorption peaks at 294 nm and 276 nm, respectively. To isolate the product for Nuclear Magnetic Resonance (NMR) spectroscopy, the organic layer was simply separated, washed with water, and dried. Figure 2.11B shows the ^{1}H NMR spectra of the samples obtained from the various conditions. Control experiments (black and green curves corresponding to no QD film and in the dark, respectively) showed the signals of the starting material, including a singlet at 6.14 ppm. The doublet arising from the *ortho* hydrogens in the phenyl/aromatic rings of the reactant is at 7.68 ppm and shifts up-field to 7.59 ppm for the product stilbene. Signals from the

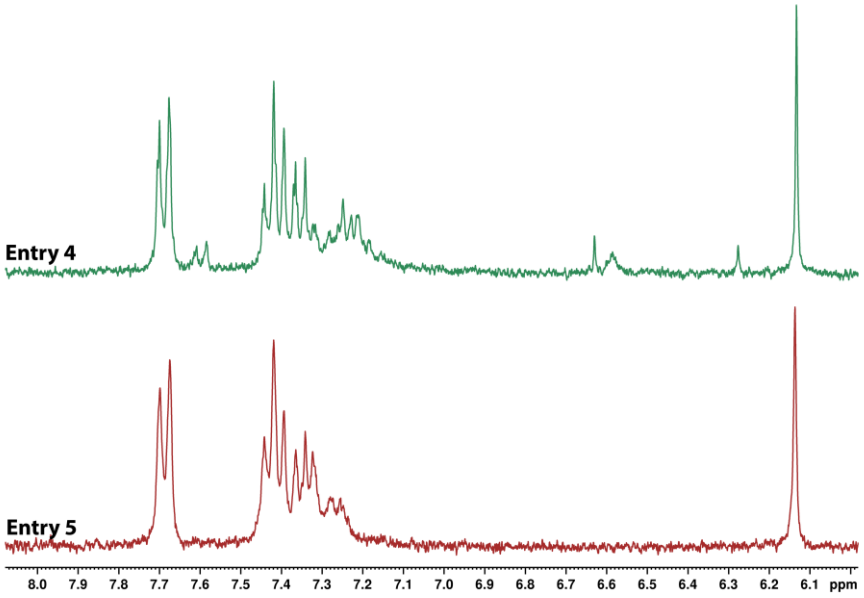

Figure 2.12. ^{1}H NMR spectra of the organic phase from the biphasic system for the reduction of DDE (in d-DMSO). Control experiment (brown, Entry 5) showed signals of DDE only, conferring the importance of heptyl viologen (HV^{2+}) as the electron shuttle between the two phases. A low concentration of HV^{2+} at 3 mol% (green, Entry 4) yielded 17 % conversion of DDE to stilbene with doped QDs, compared with 100% at 20 mol% of HV^{2+}.

meta and the *para*-protons in the aromatic rings of stilbene are in the range of 7.39-7.19 ppm, and the olefin protons show up as a singlet at 7.24 ppm and 6.63 ppm for the *trans*- and *cis*-isomers, respectively. Reactions catalyzed by the QDs showed ^{1}H NMR signals of both isomers. We monitored the conversion efficiency of the reaction via the integrated intensities of the doublets of the ortho-hydrogens (at 7.68 ppm for DDE and 7.59 ppm for stilbene). We achieved a conversion of 32% by the doped QDs without methanol, compared with a complete conversion of DDE to stilbene with 10 vol% of methanol. The progress of the reaction monitored by ^{1}H NMR is in line with the UV-Vis observations and confirms that MeOH serves as an efficient sacrificial electron donor. Table 2.11 summarizes various reaction conditions and % of conversion photocatalyzed by doped or undoped QDs, where the conversion refers to the combined total of *trans*- and *cis*-stilbene. A control experiment without viologen (reaction 5) showed 0 % conversion (Figure 2.12) and lowering the amount of HV^{2+} from 20 to 3 mol% (reaction 4, Figure 2.12) significantly reduced

Table 2.1. Summary of dehalogenation reaction of DDE: biphasic system (H_2O/EtOAc) with HV^{2+} as electron shuttle (Reactions 1-6); monophasic reduction in EtOAc (without HV^{2+}, Reactions 7-10). All reactions were irradiated for 24 h.

Entry	DDE (μmol)	QDs	QDs (nmol)	QDs (mol%)	HV^{2+} (mol%)	Methanol (vol%)	%[1,2] Conversion
1	4	Doped	0.49	0.012	20	10	100
2	4	Doped	0.49	0.012	20	0	32
3 (dark)	4	Doped	0.49	0.012	20	10	0
4	4	Doped	0.49	0.012	3	10	17
5	4	Doped	0.49	0.012	0	10	0
6	4	None	0	0	20	10	0
7	4	Doped	0.49	0.012	0	10	100
8	4	Undoped	0.49	0.012	0	10	70
9	12	Doped	0.49	0.004	0	25	70
10	12	Undoped	0.49	0.004	0	25	45

1 – Includes *cis* and *trans* isomers
2 - % conversion determined by integrating doublets of products (7.61-7.59 ppm) and dividing by the sum of the areas of doublets of products and reactants (7.70-7.68 ppm)

the yield, indicating the important role of HV in shuttling the electrons between the two phases. We observed variable isomeric ratios between replicate runs, which may arise from rotational conformers[54] of the radical intermediate in the step-wise two-electron reduction mechanism as we did not detect photoisomerization of *trans*-stilbene under the irradiation condition nor changes to the isolated product upon further irradiation. For the reaction photocatalyzed by doped QD with 10% MeOH (reaction 1, at a scale of 1 mL of 4 mM DDE), we determined an approximate yield of 60% using the standard addition method by ^{1}H NMR spectroscopy.

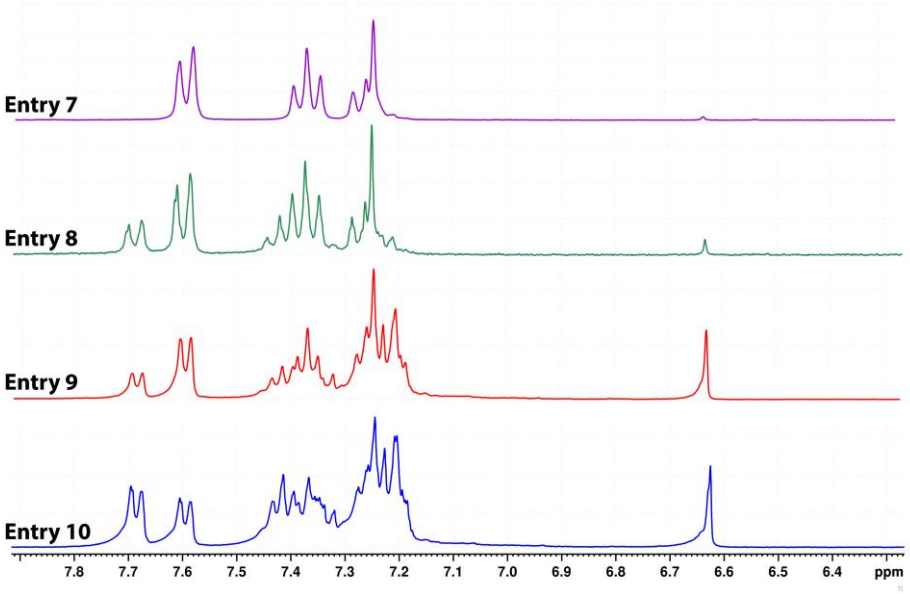

Figure 2.13. ^{1}H NMR spectra for monitoring the reduction of DDE in a monophasic system(in d-DMSO). Reactions with doped (purple, Entry 7) and undoped QDs (green, Entry 8) at a catalyst loading of 0.012 mol% where the doped QDs exhibited enhanced activity with only signals of stilbene detected. At a low catalyst loading (0.004 mol%), samples from both doped (red, Entry 9) and undoped (blue, Entry 10) showed incomplete reactions.

The energy levels in Figure 2.5 show that the LUMO of DDE is lower than the conduction band of CdS QD. Hence, the reaction can also be photocatalyzed directly by excited electrons of the QDs. Reactions 7-10 in Table 1 examined the conversion of DDE to stilbene in a single phase (i.e., EtOAc with MeOH) without the electron shuttle. We tested different reaction conditions to

compare the photocatalytic activity of doped vs undoped QDs. An enhanced conversion again was observed for Mn:CdS/ZnS vs CdS QDs, and 100 % conversion was achieved with 0.012 mol% of doped QDs (based on ^{1}H NMR data, Figure 2.13). The results showed the consistent enhanced performance of the doped QDs versus their undoped counterparts, in aqueous and nonaqueous solvents, allowing for flexible reaction design and workups.

2.3.4 Reusability of Mn-doped QD film

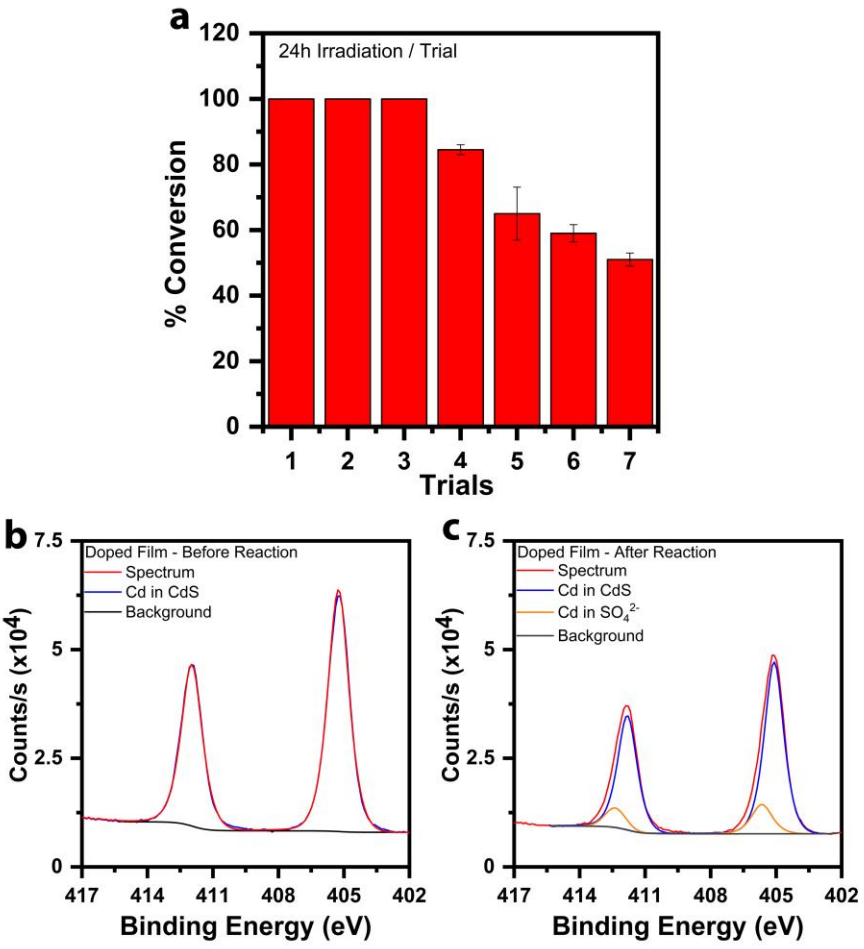

Figure 2.14. (A) Percent conversion of DDE based on ^{1}H NMR data when coated vials were used back-to-back without any treatment. Each trial was 24-h of irradiation. Error bars are standard deviations of 3 replicates. (B) X-ray photoelectron spectra of Cd 3d in Mn:CdS/ZnS QD films before and (C) after the photoredox reaction of DDE. Experimental spectra shown in red and fitted curves in other colors with each doublet corresponding to spin-orbit coupling of $3d_{5/2}$ and $3d_{3/2}$.

Next, we investigated the reusability of the QD films by carrying out back-to-back reactions over 7 days, without any treatment. Figure 2.14A shows that Mn:CdS/ZnS-coated vials yielded 100% conversion of DDE to stilbene in the first three runs (each 24 h); however, a decline of conversion to 84% - 55% was observed when the film was reused 4-7 times. We attribute the decrease in performance to several factors, including some detachment of the QDs from the walls of the vial and changes to the surface of the QDs due to the redox activities.[55] The latter has been noted in the literature, where surface ligands can detach, or surface trap states related to photogenerated electrons and holes can accumulate over time. The presence of trap states leads to non-radiative recombination of excitons and therefore negatively impacts the absorption, emission, and Auger processes.[56,57] We carried out X-ray photoelectron spectroscopy (XPS) on the films before and after reaction to examine the changes to the QDs. Table 2.2 summarizes the findings of the XPS. Initially, the binding energy (B. E.) of Cd 3*d* correspond to only CdS (405.1 eV); however an additional species, likely $CdSO_4$, was detected at B. E. of 405.4 eV[59] after the dehalogenation reaction (Figure 2.14B, C). The data is in line with the S 2*p* signal where the fraction of sulfate increased after reaction (from 8.9 % to 15.3 %, Figure 2.15). Previous work reported that surface

Table 2.2. Binding energies of Cd (3d) and S (2p) in Mn-doped CdS/ZnS core/shell films before and after photoredox reaction compared with literature.

Before Reaction				After Reaction				Literature
Element/ Transition	B. E. (eV)	Conc. (at %) [a]	Peak Assignment	Element /Transition	B. E. (eV)	Conc. (at %) [a]	Peak Assignment	B. E. (eV)
Cd $3d_{5/2}$	405.06	100	Cd in CdS	Cd $3d_{5/2}$	405.09	84.6	Cd in CdS	405.0[58]
Cd $3d_{3/2}$	411.78		Cd in CdS	Cd $3d_{3/2}$	411.81		Cd in CdS	411.8[58]
				Cd $3d_{5/2}$	405.65	15.4	Cd in $CdSO_4$	405.4[59]
				Cd $3d_{3/2}$	412.67		Cd in $CdSO_4$	412.2[59]
S $2p_{3/2}$	161.50	87.8	S^{2-} in CdS	S $2p_{3/2}$	161.56	80.2	S^{2-} in CdS	161.4[58]
S $2p_{1/2}$	162.68		S^{2-} in CdS	S $2p_{1/2}$	162.74		S^{2-} in CdS	162.6[58]
S $2p_{3/2}$	163.10	3.2	S^0	S $2p_{3/2}$	162.83	4.5	S^0	163.3[b59]
S $2p_{1/2}$	164.28		S^0	S $2p_{1/2}$	164.01		S^0	
S $2p_{3/2}$	168.21	8.9	S^{6+} in SO_4^{2-}	S $2p_{3/2}$	168.40	15.3	S^{6+} in SO_4^{2-}	168.6 [b59]
S $2p_{1/2}$	169.39		S^{6+} in SO_4^{2-}	S $2p_{1/2}$	169.58		S^{6+} in SO_4^{2-}	

oxidation of the QDs leads to the conversion of sulfide to sulfate,[60] and sulfate ions can detach from the QDs over time and expose a fresh layer of material susceptible to subsequent oxidation. Table 3 summarizes the atomic compositions of the samples before and after a catalytic run, which provide information on the quality of the QD films. Some detachment of QDs is evident by the increase in In3d signal (from the ITO substrate) after reaction. It suggests a more exposed substrate, likely due to cracks or pin holes in the film after use. Therefore, additional passivation or repeated cross-linking of the QDs films after a reaction trial may increase the durability of the QD films. Other sacrificial electron donors such as, S^{2-}/SO_3^{2-}, triethylamine, and EDTA, may be explored to increase the reusability of the QD films because they have higher redox potentials than methanol and may provide faster electron regeneration in the QD film. The ionic hole scavengers such as S^{2-}/SO_3^{2-} may be more compatible in aqueous media and yield more favourable kinetics.[48,61–63] We note that although microscopic changes on the QD surface were detected after

Table 2.3. Atomic % composition obtained from XPS of crosslinked Mn:CdS/ZnS QD film before and after reaction. Signals of Indium come from the ITO substrates and that of Si come from MPTMS used to anchor the QDs on the substrate. A significant increase in In 3d signal was observed post reaction, suggesting the loss of QDs. Note that Mn signals overlapped with loss structures of other species and could not be fitted or quantified.

		Films Before Reaction	**Films After Reaction**
Element/ Transition	**B. E. (eV)**	**Atomic %**	**Atomic %**
Si *2p*	102.21	0.45	0.15
P *2p*	132.47	0.1	0.05
S *2p*	161.98	9.5	7.25
C 2_p	284.96	73.15	73.3
Cd *3d*	405.13	3.6	3.3
O *1s*	532.01	7.95	12.55
Zn *2p3*	1021.96	4.35	2
In *3d*	450.95	0	1.05
N *1s*	399.82	0.85	0.25

1 run, the decrease in the reactivity was detected only after 3 runs (72 h of irradiation). Overall, the model reaction of stilbene production shows that doped QDs have superior photocatalytic activity compared with undoped QDs and may serve as replacements to transition metal complexes. Furthermore, the facile three-step film fabrication process to incorporate supported-QD catalysts in the reaction is desirable because ligand exchange of QDs to make them dispersible in reaction solvents is not needed and the reaction solution is readily separated from the QD film.

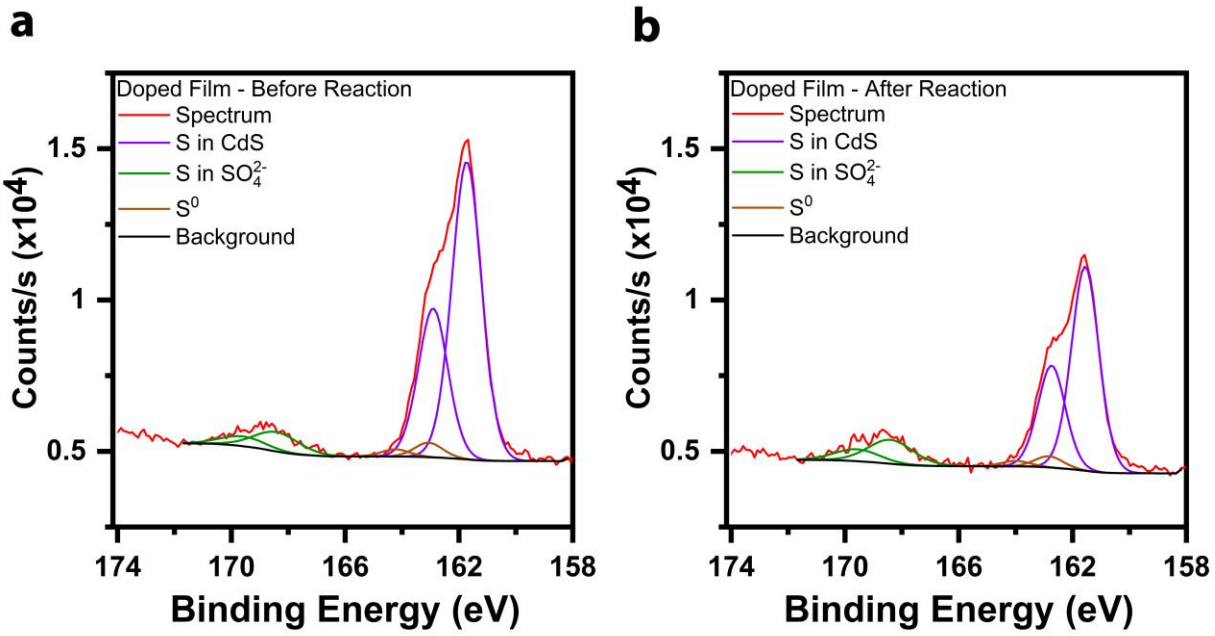

Figure 2.15. X-ray photoelectron spectra of S 2p of Mn:CdS/ZnS QD films before (A) and after (B) the photoredox reaction of DDE. Experimental spectra shown in red and fitted curves in other colors with each doublet corresponding to the spin-orbit coupling of $2p_{3/2}$ and $2p_{1/2}$.

2.3.5 Photoreduction of nitrobenzene

Lastly, we applied the Mn:CdS/ZnS QD films to the photocatalytic reduction of nitrobenzene to aniline to investigate if the enhanced reduction from hot electrons of Mn-doped QDs is applicable broadly. The reduction of nitrobenzene to aniline is a six-electron and six-proton reaction that requires multiple electron transfer steps, via either the direct or indirect pathway.[64,65] Typical transition metal photocatalysts generate one exciton at a time, thus multielectron

reductions need to be mediated via a cocatalyst or require additional intrinsic mechanisms that accumulate charge carriers.[66]

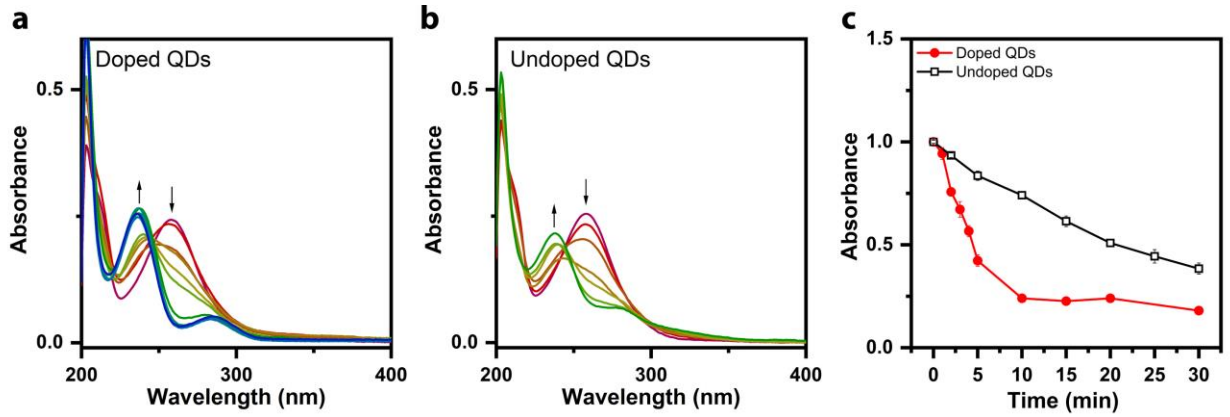

Figure 2.16. Photoreduction of nitrobenzene (258 nm) to aniline (237 nm 280 nm) monitored by UV-Vis spectroscopy. (A & B) UV absorption spectra of the reaction solution photocatalyzed by doped (A) and undoped QDs (B) respectively. (C) Time dependence of absorbance of nitrobenzene at 258 nm for triplicate runs with doped (red) and undoped (black) QDs respectively. Error bars represent standard deviations.

Heterogeneous catalysts with large surface area could circumvent these drawbacks. We carried out the photoreduction of nitrobenzene in 2-propanol with ammonium formate as the sacrificial electron donor and proton source, using reaction vials coated with the QDs. Figure 2.16A, B shows the UV absorption spectra of the reaction solutions over 30 min under irradiation at 395 nm as photocatalyzed by the doped QDs vs undoped QDs. The absorbance peak of nitrobenzene is centered at 258 nm compared with those of aniline at 237 and 280 nm. The spectral changes in Figure 2.16A, B suggest the reduction of nitrobenzene to aniline. We monitored the extent of the reaction from the absorbance peak of nitrobenzene at 258 nm, as summarized in Figure 5C over three trials. We observed a rapid decrease (77%) in the nitrobenzene absorption within the first 10 min of the reaction photocatalyzed by the doped QDs. Conversely, the undoped QDs produced a slow linear decay of 26% during the first 10 min and the reaction remained

incomplete up to 48 h of irradiation. For doped QDs, the ^{1}H NMR shows a complete conversion to aniline within 15 minutes (Figure 2.17). We obtained an internal quantum efficiency (IQE) of ~3 % for the six-electron process to form aniline (see Appendix A1) where 33 excitons were needed to reduce one nitrobenzene molecule to aniline. If all electron transfer steps are sequential[66] and similar in efficiency, the results suggest an impressive IQE of 55% for each step by the doped QDs.

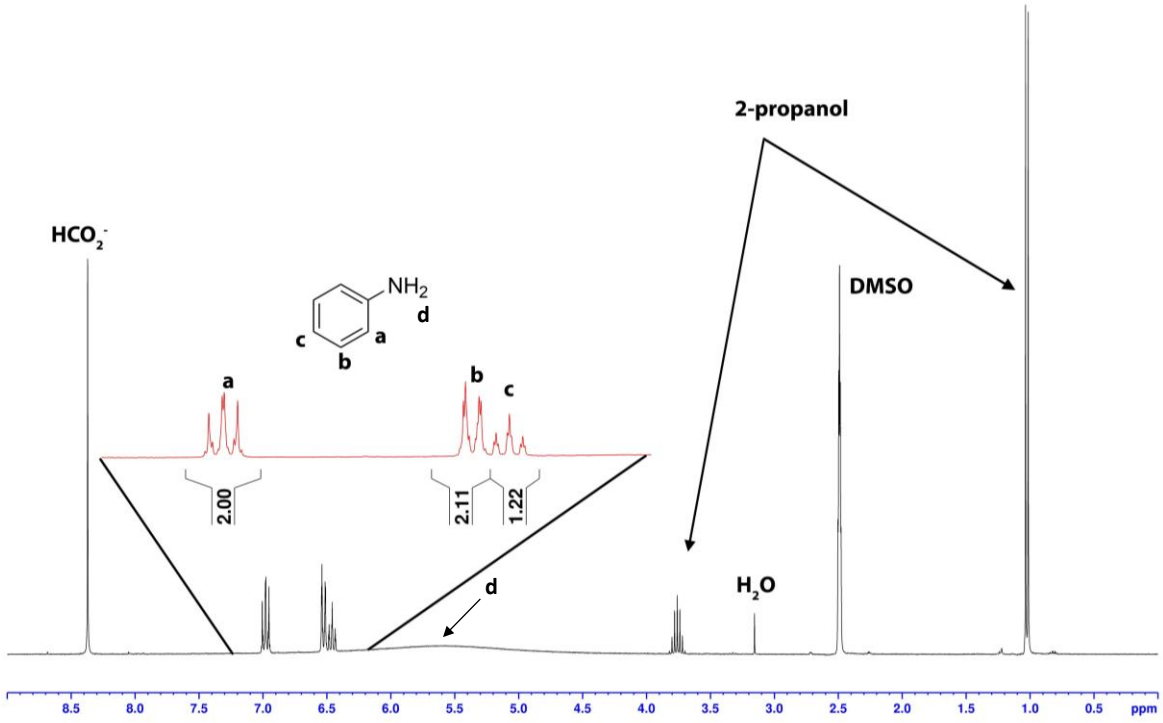

Figure 2.17. ^{1}H NMR spectrum of post reaction solution depicting successful conversion of nitrobenzene to aniline in d-DMSO. Inset shows the ratio between integrated peaks.

The photoreduction of nitrobenzene at neutral pH serves as a direct investigation of the reducing power of the hot electrons from the Mn^{2+}-Auger relaxation process. Our reaction condition at neutral pH is in contrast with previous work that employed undoped CdS QDs at an acidic pH,[66] where the reduction potential of nitrobenzene (-0.16 V vs NHE at pH 4) was significantly below the energy of the CB of CdS. At neutral pH, the reduction potential of

nitrobenzene is ca. -1.19 V vs NHE, thus placing the LUMO of nitrobenzene close to the CB of QD (see Figure 2.5). Photogenerated electrons at the band edge therefore may be insufficient in reducing power compared with hot electrons from Mn-doped QDs. However, the undoped QDs can drive this reaction at a moderate rate, suggesting non-negligible Auger relaxation in the undoped CdS that yields a small fraction of hot electrons. Notably, recent works of Mn^{2+}-doped QDs showed that the rate of Auger process outpaces that of intraband cooling,[17,18] and the exceptionally large uphill energy gain rates enabled by the spin-exchange Auger process leads to a large population of non-equilibrium hot electrons, which can undergo additional energy-transfer steps and upconversion to yield ejected electrons[18]. Other reaction pathways in our nitrobenzene reduction may involve H_2 generated by the oxidation of formate or 2-propanol by the photogenerated holes. Interestingly, a previous study showed that undoped QDs preferentially produced H_2 from formate while doped QDs generated more CO. Hence, the indirect reduction of nitrobenzene by H_2 may be more dominant in undoped QDs than doped QDs. Taken together these differences, the significantly higher rate of photoreduction of nitrobenzene by the Mn:CdS/ZnS QDs highlight the strong reducing power of the Auger-mediated hot electrons.

2.4 Conclusions

The Mn^{2+}-doped QDs consistently showed an increased photocatalysis of organic reactions compared with the undoped QDs, which we attribute to enhanced Auger processes in Mn:CdS/ZnS. The QD film coating shows high versatility in various solvents, can be employed in biphasic systems, is reusable, and reduces post-reaction purification needs. Improvements on the recyclability may be achieved by passivating the films between reaction intervals and further optimizing the sacrificial electron donors. Future directions include assembling the QD film on conductive substrates to yield a photoelectrochemical device, where secondary electrons can be

injected to undergo Auger relaxation with the excited Mn^{2+} state, further boosting the hot-electron generation and opening new opportunities in photoelectrochemical-driven organic transformations. Overall, Mn-doped QDs show great promise as photocatalysts in organic reactions and may substantially increase the rate of photoreductions of challenging substrates recently demonstrated to be photocatalyzed by undoped CdS QDs.[67] Importantly, Auger cross-relaxation, which otherwise is a detrimental process in optoelectronic applications, presents a promising phenomenon in advancing QD-based photocatalysis.

2.5 Experimental

Materials

Cadmium oxide (CdO), oleic acid, octadecene technical grade (ODE), sulfur (S), oleylamine, manganese (II) acetate tetrahydrate ($Mn(OAc)_2 \cdot 4H_2O$), heptanediamine (HDA), 1,2-dibromo-1,2-diphenylethane (DDE), anhydrous methanol, heptyl viologen (HV^{2+}), deuterated-dimethyl sulfoxide (d-DMSO), 1,1'-dimethyl-4-4'-bipyridinium ditriflate (MV^{2+}), 1,1'-diheptyl-4-4'-bipyridinium dibromide (HV^{2+}), mercaptopropyltrimethoxysilane (MPTMS) and ammonium formate, and nitrobenzene were obtained from Sigma Aldrich.

Synthesis of manganese-doped cadmium sulfide quantum dots

In a typical synthesis of Mn:CdS QDs, three flasks separately containing 0.75 mmol of CdO in 7.9 g of ODE, 0.25 mmol of sulfur in 3.3 g of ODE, and 0.04 mmol of manganese (II) acetate tetrahydrate in 2.44 g of oleylamine were degassed for 30 minutes under nitrogen at 130 °C. The CdO solution was heated to 285°C, followed by the injection of the Mn oleylamine solution.[15,57,68,69] The temperature of the solution was quickly brought back up to 285 °C and the sulfur solution was rapidly injected to start the nucleation of the QDs. The reaction was kept at

265 °C for 3 minutes to allow for the growth of the particles. Then, the solution was cooled in a water bath to room temperature. The synthesis of undoped CdS QD was carried out similarly without Mn precursor in the oleylamine. The orange photoluminescence was observed for Mn:CdS and blue photoluminescence for undoped CdS QDs. The particles were washed via flocculation with ethanol and redispersing in toluene.

Growth of ZnS shell via successive ionic layer adsorption and reaction (SILAR)

Both doped and undoped quantum dots were passivated with a ZnS shell using previously established methods[70]. QDs were re-suspended in a 3:1 ODE/oleylamine mixture and degassed for 30 min at 130 °C. A 0.4 M zinc oleate solution was prepared by dissolving zinc oleate in octadecene at 200 °C. A sulfur precursor solution was prepared by dissolving sulfur in octadecene at 130 °C. The temperature of the QD solution was raised to 265-270 °C followed by the slow injection of aliquots of zinc oleate and sulfur solutions sequentially (~1 mL/minute) with 10 min reaction time between injections. The zinc oleate and sulfur solutions were injected while warm to prevent precipitation and each aliquot corresponded to the amount needed to deposit a monolayer of atoms on the existing CdS. For example, a sample containing 2.89×10^{16} CdS QDs with 2.25 nm radius required 3.15 mmol of Zn oleate and S for each monolayer growth. Each monolayer of ZnS is theoretically 0.31 nm in thickness (i.e. $\frac{\sqrt[3]{a}}{3}$ where a = 5.41 Å, the unit cell length of zinc blende[71]). The procedure was repeated to install 2 monolayers of ZnS plus a Zn terminal layer (i.e. collectively referred to as 2.5 monolayers of ZnS shell). The passivated QDs were washed and redispersed in toluene.

QD film preparation

The glass vessels or cut microscope slides were cleaned with piranha solution (3:1 H_2SO_4/H_2O_2) for 20 minutes, rinsed with copious amounts of water, followed by silanization with 1 vol% mercaptopropyltrimethoxysilane (MPTMS) in anhydrous ethanol for 2 h. The substrates were rinsed and annealed for one hour under nitrogen at 80 °C. ***Caution!*** *Piranha solution must be prepared and handled with extreme care. It is a strong oxidizing agent that reacts aggressively with organic matter*.

For in situ spectrophotometric experiments (i.e. photoreduction of MV), the QD film was deposited on a MPTMS-treated glass slide (0.5 x 1 cm) via the evaporation-induced self-assembly process. The glass slide was suspended vertically in 4-mL vial containing 2 mL of ~300 μM QD in toluene and placed in the oven at 60 °C for 24 h. Upon evaporating the solvent, the QDs uniformly deposited on the glass surface and one side was wiped clean. The sample was then transferred to a glove box to crosslink the QDs with HDA, as previously established.[15] The films were immersed in 0.5 vol% HDA in ethanol at 80 °C for 2 min, rinsed with ethanol and annealed under nitrogen for 1 hour.[15] A similar procedure was carried out for glass vials for DDE and nitrobenzene reactions.

The amount of deposited QD was determined from the extinction coefficient and absorbance of a toluene solution containing redissolved QDs from a non-crosslinked film. Similar procedure was used for determining moles of QDs in the coated vials.

Photoreduction of methyl viologen

A volume of 3 mL 500 μM methyl viologen in water was transferred to a cuvette with a QD-functionalized glass strip (0.5 x 1 cm) inside. The system was thoroughly degassed and sealed.

The cuvette was irradiated with blue light (440 nm, Lumencor SpectraX light engine) and in-situ UV-visible absorption spectra (Perkin Elmer Lambda 950) were acquired at 3-min interval using a custom setup. The reduction of methyl viologen was confirmed by monitoring the development of peaks at 396 nm and 605 nm, and the emergence of blue color in the solution. Experiments with 10% v/v methanol as a hole scavenger were conducted similarly. Control experiments in the absence of light and in the absence of QDs were also performed with the same setup.

Photoluminescence experiments

Photoluminescence (PL) of QD deposited on the glass strips was measured for both doped and undoped samples using a custom-made setup comprising a light source (Lumencor SpectraX) and a spectrometer (Ocean Optics 2000+). PL lifetime measurements were obtained with a Cary Eclipse fluorescence spectrometer with a pulsed Xe lamp.

Dehalogenation reaction

To a 4-mL vial coated with QDs, an aqueous solution of 2 mL heptyl viologen (500 µM) containing 10 vol% methanol was added. Then 1 mL of 4 mM 1,2-dibromo-1,2-diphenylethane (DDE) in ethyl acetate was added as the organic phase. The vial was sealed and placed under 395-nm LED (SZ-05-U6, Luxeonstar) irradiation for 24 h. The stirring was kept at 250 rpm to form a small vortex between the two layers. After 24 h, the organic layer was separated. Subsequently, the aqueous layer was extracted three times with 0.5 mL portions of ethyl acetate. The ethyl acetate solution was then air dried. Control experiments were carried out in the absence of QDs (i.e., uncoated vials), and in the absence of heptyl viologen or methanol.

The single-phase reaction, in the absence of heptyl viologen, was also performed. A QD-coated vial containing 3 mL of 4 mM DDE in ethyl acetate and methanol (10 vol%) was irradiated

at 395 nm for 24h. UV-Vis absorbance of as-is solution was acquired using Perkin Elmer Lambda 950 spectrophotometer, and ^{1}H NMR of isolated sample in d-DMSO was measured using Bruker Avance (300 MHz). Percent conversion of reactants to products was determined by taking the peak area ratios of the doublets of products (7.61-7.59 ppm) to the sum of the products and reactants (7.70-7.68 ppm). All reactions of DDE were run inside the glove box.

Reduction of nitrobenzene

The reduction of nitrobenzene was carried out in a similar fashion as that of the DDE. In a typical reaction, a QD-coated vial containing 3 mL of nitrobenzene (3.7 mM) and 100 mM ammonium formate in 2-propanol was sealed and placed under 395-nm irradiation for 30 min with stirring. UV absorption spectra of as-is solution were measured at various time intervals, and NMR spectra were collected in d-DMSO after the sample was dried and extracted with dichloromethane.

Physical characterizations

EPR measurement was carried out on a solution of Mn:CdS/ZnS QD dissolved in toluene using a Bruker ECS-EMX X-band EPR spectrometer equipped with an ER4119HS cavity. EPR data was collected at room temperature with the following acquisition settings: 9.367 GHz microwave frequency, 2.15 mW microwave power, 4G modulation amplitude, a 100 kHz modulation frequency, 5000 G sweep width, 0.01 ms time constant, 50 dB receiver gain, and 300s total sweep time. The spectrum was corrected using DPPH (1,1-diphenyl-2-picrylhydrazyl) as a standard.

TEM images were acquired using Hitachi HT7700 with LaB_6 thermionic filament operating at an emission current of 10 mA and accelerating voltage of 100 kV.

X-ray photoelectron spectra of films on indium tin oxide substrates were measured by Thermo Fisher Scientific K-Alpha XPS spectrometer (East Grinstead, UK) with a spot area of 400 μm. A monochromatic Al K_α X-ray source was used to obtain an initial survey spectrum (pass energy (PE) – 200 eV) followed by low resolution spectra of the spectral regions of interest (PE – 150 eV) from which composition was obtained, and higher resolution spectra (PE – 25 eV). Charge compensation was applied using the system's combined e^-/Ar^+ flood gun with the spectra shifted to place the main C-C peak at 285.0 eV. The peak fitting was performed on the high-resolution spectra by the supplied software (Avantage v. 5.9925), using the Smart Background (a modified Shirley background) and a mixed Gaussian-Lorentzian peak shape.

Powder XRD data was obtained with a AXRD Benchtop diffractometer (PROTO) with a Cu K_α source. The spectrum was fitted with wurtzite and zinc blende by utilising the Rietveld refinement[34,35] method and GSAS II software.[72]

The concentration of Mn^{2+} dopant in CdS/ZnS core/shell QDs was determined via ICP-OES with a Thermo Scientific™ iCAP PRO Series utilizing the axial detector (Analest, University of Toronto). QDs were digested in concentrated nitric acid at 60 °C over 48 hours. The solution was then diluted with MQ water to 10 mL in a volumetric flask.

(TEM and XPS were performed at the Ontario Centre for the Characterization of Advanced Materials, Department of Chemical Engineering and Applied Chemistry, University of Toronto. EPR data were acquired at Analest facility, Department of Chemistry at University of Toronto.)

2.6 References

1. Malile, B., Sodhi, R. & Chen, J. I. L. Mn(ii)-doped CdS/ZnS core/shell quantum dot films photocatalyze reductive organic transformations with a boost in efficiency from enhanced Auger processes. *J. Mater. Chem. A* **10**, 25319–25328 (2022).

2. Pal, A., Ghosh, I., Sapra, S. & König, B. Quantum Dots in Visible-Light Photoredox Catalysis: Reductive Dehalogenations and C-H Arylation Reactions Using Aryl Bromides. *Chem. Mater.* **29**, 5225–5231 (2017).

3. Efros, A. L. *et al.* Evaluating the potential of using quantum dots for monitoring electrical signals in neurons. *Nat. Nanotechnol.* **13**, 278–288 (2018).

4. Nozik, A. J. Quantum dot solar cells. *Phys. E Low-dimensional Syst. Nanostructures* **14**, 115–120 (2002).

5. Klimov, V. I. Nanocrystal Quantum Dots: From fundamental photophysics to multicolor lasing. in *Los Alamos Science* vol. 28 214–220 (2003).

6. Wang, D. Y., Yin, Y. Y., Feng, C. W., Rukhsana & Shen, Y. M. Advances in homogeneous photocatalytic organic synthesis with colloidal quantum dots. *Catalysts* **11**, 1–14 (2021).

7. Caputo, J. A. *et al.* General and Efficient C-C Bond Forming Photoredox Catalysis with Semiconductor Quantum Dots. *J. Am. Chem. Soc.* **139**, 4250–4253 (2017).

8. Yuan, Y.-J., Chen, D., Yu, Z.-T. & Zou, Z.-G. Cadmium sulfide-based nanomaterials for photocatalytic hydrogen production. *J. Mater. Chem. A* **6**, 11606–11630 (2018).

9. Henckel, D. A. *et al.* Modeling Equilibrium Binding at Quantum Dot Surfaces Using Cyclic Voltammetry. *Nano Lett.* **20**, 2620–2624 (2020).

10. McClelland, K. P. & Weiss, E. A. Selective Photocatalytic Oxidation of Benzyl Alcohol to Benzaldehyde or C–C Coupled Products by Visible-Light-Absorbing Quantum Dots. *ACS Appl. Energy Mater.* **2**, 92–96 (2019).

11. Enright, M. J., Gilbert-Bass, K., Sarsito, H. & Cossairt, B. M. Photolytic C-O Bond Cleavage with Quantum Dots. *Chem. Mater.* **31**, 2677–2682 (2019).

12. Kodaimati, M. S. *et al.* Viewpoint: Challenges in Colloidal Photocatalysis and Some Strategies for Addressing Them. *Inorg. Chem.* **57**, 3659–3670 (2018).

13. Olshansky, J. H., Ding, T. X., Lee, Y. V., Leone, S. R. & Alivisatos, A. P. Hole Transfer from Photoexcited Quantum Dots: The Relationship between Driving Force and Rate. *J. Am. Chem. Soc.* **137**, 15567–15575 (2015).

14. Erwin, S. C. *et al.* Doping semiconductor nanocrystals. *Nature* **436**, 91–94 (2005).

15. Barrows, C. J. *et al.* Electrical Detection of Quantum Dot Hot Electrons Generated via a Mn2+-Enhanced Auger Process. *J. Phys. Chem. Lett.* **8**, 126–130 (2017).

16. Bradshaw, L. R., Hauser, A., McLaurin, E. J. & Gamelin, D. R. Luminescence saturation via Mn 2+-exciton cross relaxation in colloidal doped semiconductor nanocrystals. *J. Phys. Chem. C* **116**, 9300–9310 (2012).

17. Singh, R., Liu, W., Lim, J., Robel, I. & Klimov, V. I. Hot-electron dynamics in quantum dots manipulated by spin-exchange Auger interactions. *Nat. Nanotechnol.* **14**, 1035–1041 (2019).

18. Livache, C. *et al.* High-efficiency photoemission from magnetically doped quantum dots driven by multi-step spin-exchange Auger ionization. *Nat. Photonics* **16**, 433–440 (2022).

19. Dong, Y., Rossi, D., Parobek, D. & Son, D. H. Nonplasmonic Hot-Electron Photocurrents from Mn-Doped Quantum Dots in Photoelectrochemical Cells. *Chemphyschem* **17**, 660–664 (2016).

20. Parobek, D., Qiao, T. & Son, D. H. Energetic hot electrons from exciton-to-hot electron upconversion in Mn-doped semiconductor nanocrystals. *J. Chem. Phys.* **151**, 120901 (2019).

21. Li, X. B. *et al.* Semiconductor nanocrystals for small molecule activation: Via artificial photosynthesis. *Chem. Soc. Rev.* **49**, 9028–9056 (2020).

22. Yang, X. & Wang, D. Photocatalysis: From Fundamental Principles to Materials and Applications. *ACS Appl. Energy Mater.* **1**, 6657–6693 (2018).

23. Banin, U. *et al.* Nanotechnology for catalysis and solar energy conversion. *Nanotechnology* **32**, 42003 (2020).

24. Wu, W. *et al.* A simple and highly efficient route for the preparation of p-phenylenediamine by reducing 4-nitroaniline over commercial CdS visible light-driven photocatalyst in water. *Green Chem.* **14**, 1705–1709 (2012).

25. Dong, Y., Choi, J., Jeong, H. K. & Son, D. H. Hot electrons generated from doped quantum dots via upconversion of excitons to hot charge carriers for enhanced photocatalysis. *J. Am. Chem. Soc.* **137**, 5549–5554 (2015).

26. Parobek, D., Meeder, J. R., Puthenpurayil, J., Nippe, M. & Son, D. H. Breaking the short-range proximity requirement in quantum dot/molecular catalyst hybrids for CO2reduction: Via long-range hot electron sensitization. *J. Mater. Chem. A* **8**, 12984–12989 (2020).

27. White, M. A., Weaver, A. L., Beaulac, R. & Gamelin, D. R. Electrochemically controlled Auger quenching of Mn2+ photoluminescence in doped semiconductor nanocrystals. *ACS Nano* **5**, 4158–4168 (2011).

28. Yu, D., Wehrenberg, B. L., Jha, P., Ma, J. & Guyot-Sionnest, P. Electronic transport of n-type CdSe quantum dot films: Effect of film treatment. *J. Appl. Phys.* **99**, (2006).

29. Peng, X., Schlamp, M. C., Kadavanich, A. V & Alivisatos, A. P. Epitaxial Growth of Highly Luminescent CdSe/CdS Core/Shell Nanocrystals with Photostability and Electronic Accessibility. *J. Am. Chem. Soc.* **119**, 7019–7029 (1997).

30. Beaulac, R., Archer, P. I., Ochsenbein, S. T. & Gamelin, D. R. Mn2+-doped CdSe quantum dots: New inorganic materials for spin-electronics and spin-photonics. *Adv. Funct. Mater.* **18**, 3873–3891 (2008).

31. Schimpf, A. M., Ochsenbein, S. T. & Gamelin, D. R. Surface contributions to Mn2+ spin

dynamics in colloidal doped quantum dots. *J. Phys. Chem. Lett.* **6**, 457–463 (2015).

32. Koh, A. K. & Miller, D. J. The systematic variation of the EPR parameters of manganese in II–VI semiconductors. *Solid State Commun.* **60**, 217–222 (1986).

33. Kennedy, T. A., Glaser, E. R., Klein, P. B. & Bhargava, R. N. Symmetry and electronic structure of the Mn impurity in ZnS nanocrystals. *Phys. Rev. B* **52**, R14356–R14359 (1995).

34. Rietveld, H. M. A profile refinement method for nuclear and magnetic structures. *J. Appl. Crystallogr.* **2**, 65–71 (1969).

35. Toby, B. H. R factors in Rietveld analysis: How good is good enough? . *Powder Diffr.* **21**, 67–70 (2006).

36. Brus, L. E. Electron–electron and electron-hole interactions in small semiconductor crystallites: The size dependence of the lowest excited electronic state. *J. Chem. Phys.* **80**, 4403–4409 (1984).

37. Mikulec, F. V. *et al.* Organometallic synthesis and spectroscopic characterization of manganese-doped CdSe nanocrystals. *J. Am. Chem. Soc.* **122**, 2532–2540 (2000).

38. Dabbousi, B. O. *et al.* (CdSe)ZnS core-shell quantum dots: Synthesis and characterization of a size series of highly luminescent nanocrystallites. *J. Phys. Chem. B* **101**, 9463–9475 (1997).

39. Eskandari, P., Kazemi, F. & Zand, Z. Photocatalytic reduction of aromatic nitro compounds using CdS nanostructure under blue LED irradiation. *J. Photochem. Photobiol. A Chem.* **274**, 7–12 (2014).

40. Wang, M., Shen, S., Li, L., Tang, Z. & Yang, J. Effects of sacrificial reagents on photocatalytic hydrogen evolution over different photocatalysts. *J. Mater. Sci.* **52**, 5155–5164 (2017).

41. Belloni, J., Treguer, M., Remita, H. & De Keyzer, R. Enhanced yield of photoinduced electrons in doped silver halide crystals. *Nature* **402**, 865–866 (1999).

42. Bird, C. L. & Kuhn, A. T. Electrochemistry of the viologens. *Chem. Soc. Rev.* **10**, 49–82 (1981).

43. Bosser, G. & Paris, J. Dehalogenation of Vicinal Dibromides by Electrogenerated Polysulf ide Ions in Dimethylacetamide. *J. Chem. Soc. Perkins Trans.* **2**, 2057–2063 (1992).

44. Zhao, L. Bin *et al.* A DFT study on photoinduced surface catalytic coupling reactions on nanostructured silver: Selective formation of azobenzene derivatives from para-substituted nitrobenzene and aniline. *Phys. Chem. Chem. Phys.* **14**, 12919–12929 (2012).

45. Kuhn, A., Von Eschwege, K. G. & Conradie, J. Reduction potentials of para-substituted nitrobenzenes-an infrared, nuclear magnetic resonance, and density functional theory study. *J. Phys. Org. Chem.* **25**, 58–68 (2012).

46. Chen, H. Y. *et al.* Hot electrons from consecutive exciton - Mn energy transfer in Mn-doped semiconductor nanocrystals. *J. Phys. Chem. C* **115**, 11407–11412 (2011).

47. Qiu, X. *et al.* Applications of Nanomaterials in Asymmetric Photocatalysis: Recent Progress, Challenges, and Opportunities. *Adv. Mater.* **33**, 1–14 (2021).

48. Costantino, F. & Kamat, P. V. Do Sacrificial Donors Donate H2 in Photocatalysis? *ACS Energy Lett.* **7**, 242–246 (2022).

49. Hainer, A. S. *et al.* Photocatalytic Hydrogen Generation Using Metal-Decorated TiO2: Sacrificial Donors vs True Water Splitting. *ACS Energy Lett.* **3**, 542–545 (2018).

50. Striepe, L. & Baumgartner, T. Viologens and Their Application as Functional Materials. *Chem. - A Eur. J.* **23**, 16924–16940 (2017).

51. Maidan, R., Goren, Z., Willner, I. & Becker, J. Y. Application of Multielectron Charge Relays in Chemical and Photochemical Debromination Processes. The Role of Induced Disproportionation of N,N′-Dioctyl-4,4′-bipyridinium Radical Cation in Two-Phase Systems. *J. Am. Chem. Soc.* **106**, 6217–6222 (1984).

52. Willner, I., Goren, Z., Mandler, D., Maidan, R. & Degani, Y. Transformation of single-electron transfer photoproducts into multielectron charge relays: the functions of water-oil two-phase systems and enzyme catalysis. *J. Photochem.* **28**, 215–228 (1985).

53. Twilton, J. *et al.* The merger of transition metal and photocatalysis. *Nat. Rev. Chem.* **1**, (2017).

54. Fawell, P., Avraamides, J. & Hefter, G. Reduction of Vicinal Dihalides. I. The Electrochemical Reduction of <I>meso</I> and (±)-1,2-Dibromo-1,2-diphenylethane. *Aust. J. Chem.* **43**, 1421–1430 (1990).

55. Tang, J. *et al.* Colloidal-quantum-dot photovoltaics using atomic-ligand passivation. *Nat. Mater.* **10**, 765–771 (2011).

56. Bodunov, E. N. & Simões Gamboa, A. L. Photoluminescence Decay of Colloidal Quantum Dots: Reversible Trapping and the Nature of the Relevant Trap States. *J. Phys. Chem. C* **123**, 25515–25523 (2019).

57. Yu, W. W., Qu, L., Guo, W. & Peng, X. Experimental determination of the extinction coefficient of CdTe, CdSe, and CdS nanocrystals. *Chem. Mater.* **15**, 2854–2860 (2003).

58. Barreca, D., Gasparotto, A., Maragno, C. & Tondello, E. Nanostructured Cadmium Sulfide Thin Films by XPS. *Surf. Sci. Spectra* **9**, 46–53 (2002).

59. Meissner, D. cathodic processes at CdS particles fixed in monograin membranes [4], This technique enabled us to investigate the CdS corrosion by use of electron microscopy . In contrast to the results cited above we found that the dissolu- tion of the semiconductor. *Appl. Surf. Sci.* **27**, 423–436 (2000).

60. Alivisatos, A. P. Perspectives on the physical chemistry of semiconductor nanocrystals. *J. Phys. Chem.* **100**, 13226–13239 (1996).

61. Zhao, F., Li, Q., Han, K. & Lian, T. Mechanism of Efficient Viologen Radical Generation by Ultrafast Electron Transfer from CdS Quantum Dots. *J. Phys. Chem. C* **122**, 17136–17142 (2018).

62. Herance, J. R., Ferrer, B., Bourdelande, J. L., Marquet, J. & Garcia, H. A photocatalytic acid- and base-free Meerwein-Ponndorf-Verley-type reduction using a [Ru(bpy)3]2+/viologen couple. *Chem. - A Eur. J.* **12**, 3890–3895 (2006).

63. Berr, M. J. *et al.* Hole scavenger redox potentials determine quantum efficiency and stability of Pt- decorated CdS nanorods for photocatalytic hydrogen generation of Pt-decorated CdS nanorods for photocatalytic hydrogen generation. **223903**, (2020).

64. Mahata, A., Rai, R. K., Choudhuri, I., Singh, S. K. & Pathak, B. Direct vs. indirect pathway for nitrobenzene reduction reaction on a Ni catalyst surface: a density functional study. *Phys. Chem. Chem. Phys.* **16**, 26365–26374 (2014).

65. Gelder, E. A., Jackson, S. D. & Lok, C. M. The hydrogenation of nitrobenzene to aniline: a new mechanism. *Chem. Commun.* 522–524 (2005) doi:10.1039/B411603H.

66. Jensen, S. C., Homan, S. B. & Weiss, E. A. Photocatalytic Conversion of Nitrobenzene to Aniline through Sequential Proton-Coupled One-Electron Transfers from a Cadmium Sulfide Quantum Dot. *J. Am. Chem. Soc.* **138**, 1591–1600 (2016).

67. Widness, J. K. *et al.* CdS Quantum Dots as Potent Photoreductants for Organic Chemistry Enabled by Auger Processes. *J. Am. Chem. Soc.* **144**, 12229–12246 (2022).

68. Yu, W. W. & Peng, X. Formation of high-quality CdS and other II-VI semiconductor nanocrystals in noncoordinating solvents: Tunable reactivity of monomers. *Angew. Chemie - Int. Ed.* **41**, 2368–2371 (2002).

69. Yu, W. W. & Peng, X. Formation of High-Quality CdS and Other II–VI Semiconductor Nanocrystals in Noncoordinating Solvents: Tunable Reactivity of Monomers. *Angew. Chemie Int. Ed.* **46**, 2559 (2007).

70. Li, J. J. *et al.* Large-scale synthesis of nearly monodisperse CdSe/CdS core/shell nanocrystals using air-stable reagents via successive ion layer adsorption and reaction. *J. Am. Chem. Soc.* **125**, 12567–12575 (2003).

71. Battaglia, D., Blackman, B. & Peng, X. Coupled and Decoupled Dual Quantum Systems in One Semiconductor Nanocrystal. *J. Am. Chem. Soc.* **127**, 10889–10897 (2005).

72. Toby, B. H. & Von Dreele, R. B. {\it GSAS-II}: the genesis of a modern open-source all purpose crystallography software package. *J. Appl. Crystallogr.* **46**, 544–549 (2013).

2.7 Appendix

A1. Calculations

I. Internal quantum efficiency of methyl viologen reduction

Absorbance of film = 0.2
Film area = 1cm x 0.5 cm = 0.5 cm^2
Irradiation density at 440 nm: 85 mW/cm^2

Photons absorbed by 0.5 cm^2 film:

$$0.085\frac{W}{cm^2} \times (1 - 10^{-0.2}) \times 0.50cm^2 = 0.0157\,W$$

$$\frac{0.0157\,J/s}{4.51E^{-19}\,J/photon_{440nm}} = 3.48E^{16}\,photons/s$$

$$\frac{3.48E^{16}\,\frac{photons}{s}}{6.022\,E^{23}\,\frac{photons}{mol}} = 5.79E^{-8}\,\frac{mol}{s}\ of\ photons$$

Rate of $MV^{\bullet+}$ formation:
Initial MV^{2+} concentration and volume = 500 µM × 3 mL

$$0.00112\,s^{-1} \times 1.5E^{-6}mol = 1.7E^{-9}\,\frac{mol}{s}\ of\ MV$$

$$IQE = \frac{rate\ of\ product\ formation}{rate\ of\ absrobed\ photons} = \frac{1.7E^{-9}\,mol/s}{5.8E^{-8}\,mol/s} = 0.029\ or\ 2.9\%$$

II. Number of photons irradiated, and excitons produced per QD at 85 mW/cm^2:

$$0.085\,W/cm^2 \times 0.50cm^2 = 0.042\,W$$

$$\frac{0.042\,J/s}{4.51E^{-19}\,J/photon_{440nm}} = 9.42E^{16}\,photons/s$$

$$rate\ of\ photons\ irradiated\ per\ QD = \frac{rate\ of\ photons}{number\ of\ QDs} = \frac{9.2E^{16}\,\frac{mol}{s}}{1.26E^{13}\,\frac{mol}{s}} = 7400\,photons/s$$

$$rate\ of\ exciton\ produced\ per\ QD = 7400\,\frac{photons}{s} \times 0.37 = 2700\,\frac{excitons}{s}$$

III. Internal quantum efficiency of photoreduction of nitrobenzene to aniline

Absorbance of film at 395 nm was ca. 0.25 (based on deposition condition and film used in MV reaction). Absorbance by the film on the concave vial wall would be affected by scattering, and thus the IQE is an estimate.

Irradiation density at 395 nm: 150 mW/cm^2

Area of film: 1.87 cm^2

Photons absorbed in 15 min:

$$0.15\frac{W}{cm^2} \times (1 - 10^{-0.25}) \times 1.87cm^2 = 0.123\,W$$

$$\frac{0.123\,J/s}{5.03E^{-19}\,J/photon_{440nm}} \times 15\,\text{min} \times 60s = 2.21E^{20}\,photons\,absorbed$$

$$= 3.67E^{-4}\,mol\,of\,absorbed\,photons$$

Assuming total conversion of nitrobenzene to aniline (based on ^{1}H NMR):

$$IQE = \frac{product\ formed\ in\ 15\ min}{photons\ absorbed\ in\ 15\ min} = \frac{1.11E^{-5}\text{mol aniline}}{3.67E^{-4}\text{ mol absorbed photons}} = 3.0\ \%$$

If sequential electron reduction with same efficiency:

$$IQE\ for\ each\ step = 0.030^{\frac{1}{6}} = 0.55 = 55\%$$

A2. ICP-OES

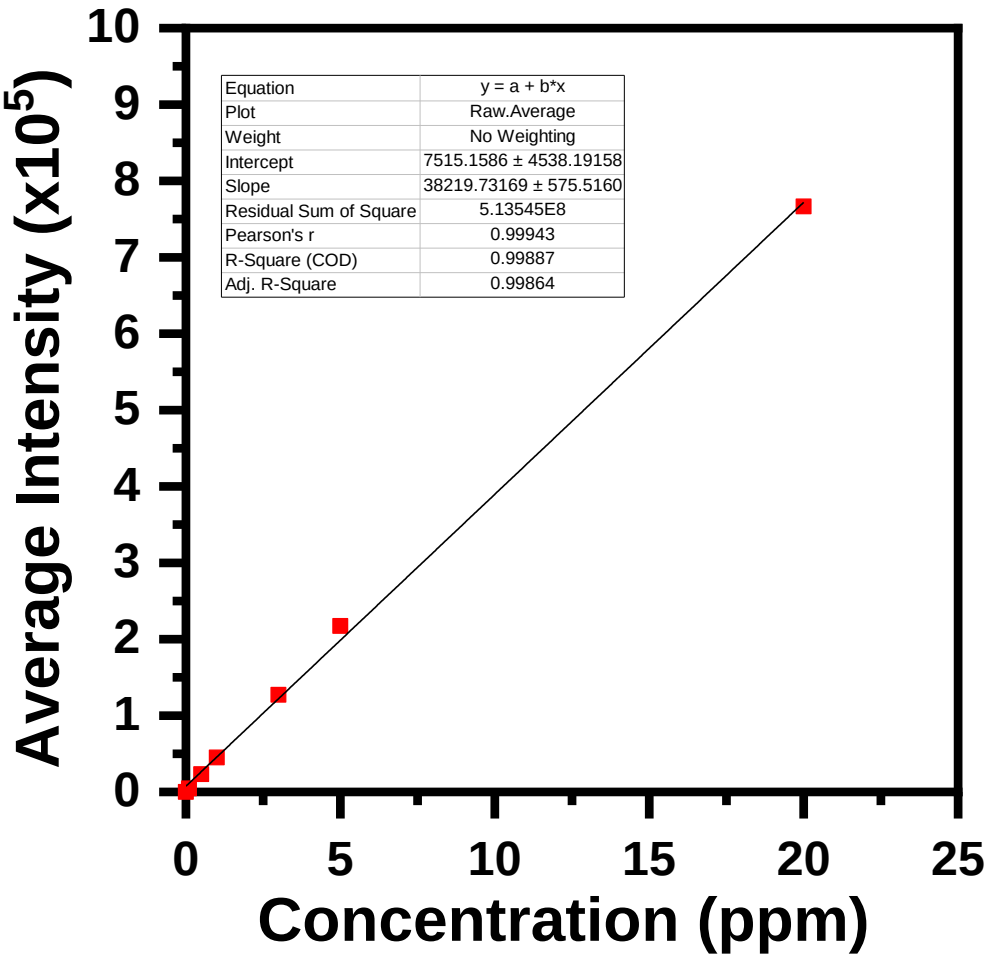

Figure A1. Calibration curve for Mn, Cd, and Zn.

Table A1: Elemental analysis of QDs with ICP-OES.

	Emission Wavelength (nm)	**Concentration (ppm)**
Mn	257.610	2.47 ± 0.03
	259.573	2.43 ± 0.01
	260.569	2.37 ± 0.01
Cd	228.820	295.3 ± 0.5
	226.502	297.5 ± 0.2
	214.438	311.3 ± 0.2
Zn	213.856	261.5 ± 0.4
	202.548	265.4 ± 0.1
	206.200	253.4 ± 0.3

Chapter 3 – Doped-QD Coated Photocatalytic Flow Reactors, Challenges, and Future Directions.

Previously, Mn:CdS/ZnS QD films proved effective photocatalysts for reductive organic transformations. The QD films displayed compatibility in various solvents, and accelerated post reaction workup by eliminating time-consuming separation steps. These attributes are highly desirable in the field of flow chemistry. In this chapter, we showcase and discuss the potential of doped-QD coated flow reactors, which may provide alternative tools for organic transformations and facilitate reactions otherwise not possible under mild conditions.

3.1 Background to flow reactors

Batch processes are an example of thermal chemistry and have been utilized for decades in the pharmaceutical industry.[1] They comprise consecutive reactions and separation steps with the aim of obtaining high yields of a specific pharmaceutical while offering little regard to energy usage, chemical waste, and overall reagent consumption.[2,3] These processes have remained relatively unchanged over the years. However, with legislations shifting toward sustainability and reduction of carbon emissions, the overall profile of these batch processes is desired to be "green" as well.

Continuous flow processes have shown their potential for increasing sustainability and efficiency. Already implemented in the petrochemical and food industries, flow processes have resulted in an increased productivity and a decreased cost when compared with batch processes.[4] Currently, research in the implementation of continuous flow processes in the pharmaceutical industry is growing rapidly. While flow reactors are unlikely to replace batch processes entirely, they can provide sustainable, cost-effective, and time-efficient alternative methods for organic transformations.[5] In the small scale, continuous flow reactors offer precise heat transfer and

mixing of reagents, better control of toxic and reactive substances, and highly efficient photochemical or electrochemical methods.[5,6] Specifically, the utilization of flow reactors in visible-light photocatalysis presents new, green, and sustainable approaches to synthetic organic chemists.

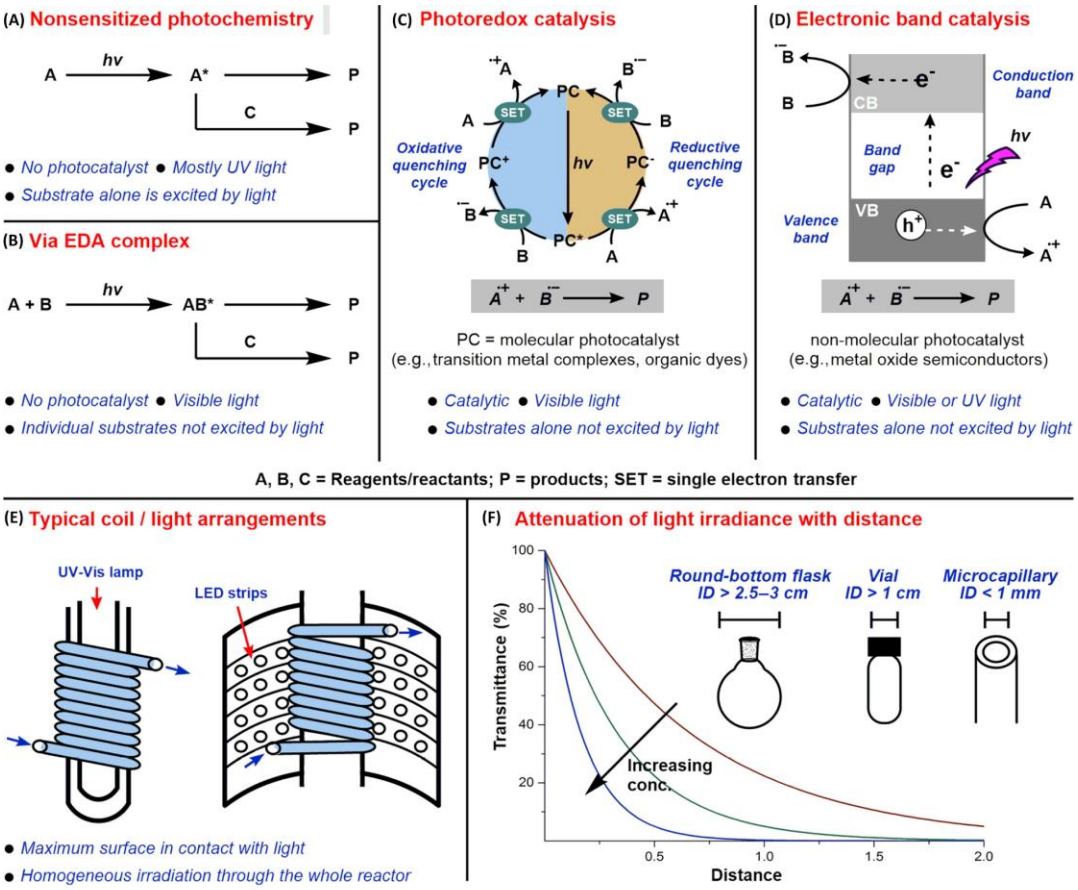

Figure 3.1: (A) Light driven photochemical reaction. (B) Photochemical formation of electron donor-acceptor (EDA) complex. (C) Photoredox catalysis. (D) Semiconductor-assisted Photoredox catalysis. (E) Typical schematics of flow reactors. (F) Effect of distance on the irradiation intensity. Reprinted with permission from reference 3.

Figure 3.1 A-D shows various types of photochemical reactions that have potential to be implemented in a flow settup.[7] Figure 3.1A and 3.1B show schematics of non-sensitized photochemical reactions that can be driven via UV or visible light. Figure 3.1C and D show photoredox catalysis typically facilitated by transition metal complexes and semiconductor

materials respectively, as discussed in Chapter 1. Irrespective of the sensitizers, a small-scale flow reactor consists of tubing either wrapped around a light source or surrounded by strips of LED lighting (Figure 3.1E). Lastly, light intensity decreases exponentially with distance from the light source (Figure 3.1F). Thus, non-homogeneous irradiation can result in slow reactions or formation of undesirable reaction intermediates. Conversely, a narrow flow reactor improves the photon flux to the sensitizer and increases the efficiency of the reaction. [7,8]

Various photoredox reactions with iridium complexes as sensitizers that activate the nickel catalytic cycle have been adapted for flow conditions.[9] Figure 3.2 depicts a decarboxylative arylation reaction in the multigram scale. However, homogenous conditions result in wasteful isolation, purification, and post reaction workup, specifically for the catalysts.[2,10] Replacing the iridium photocatalyst with QDs supported on the walls of the flow reactors, simplifies the reaction setup and post reaction processes. While semiconductor films have been investigated as coatings in flow reactors for water treatment applications,[11] their use in photoredox catalysis of organic transformations remains limited. Here, we present the implementation of the Mn-doped CdS/ZnS core/shell QDs as photocatalysts in a flow reactor. Utilizing the nitrobenzene reduction as a model reaction, we performed preliminary investigation on the feasibility of Mn^{2+}:CdS/ZnS coating in a photocatalytic flow reactor. Challenges and future work are discussed.

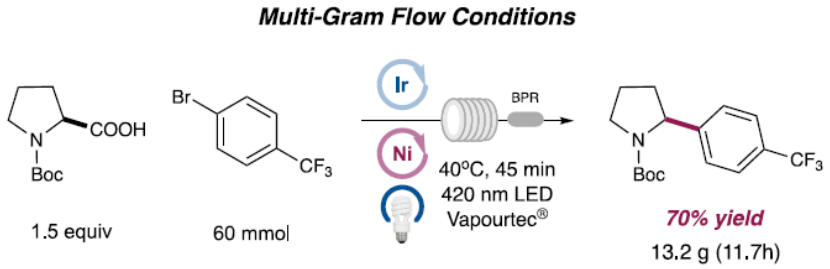

Figure 3.2. Decarboxylative arylation adapted for flow conditions. Image adapted from reference 9. License link https://creativecommons.org/licenses/by-nc-nd/4.0/legalcode

3.2 Flow reactor coated with Mn-doped quantum dots

3.2.1 Experimental

The inner wall of a Pasteur pipette, which served as the reaction chamber, was treated with mercaptopropyltrimethoxysilane followed by coating with Mn-doped QDs via evaporated-assisted deposition. The quantum dot film was then crosslinked with heptanediamine (as in Section 2.5) and stored under inert conditions. The coated reaction chamber was connected via a plastic tubing to a syringe filled with a solution of 0.5 mM nitrobenzene and 150 mM ammonium formate in 2-propanol under inert conditions. The flow system was equilibrated under 395-nm irradiation (SZ-05-U6, Luxeonstar LEDs) for 30 min before initializing the syringe pump to deliver at a rate of 2 mL/h. (unless otherwise specified). Aliquots were collected and diluted for UV absorption measurement. For back-to-back reactions, the flow reactor, tubing and syringe were rinsed with isopropanol, dried and placed in the glove box where they were assembled again.

3.2.2 Results and Discussion

We developed a flow reactor to show the versatility of the QD films and their potential for efficient, large-scale photoredox reactions. Figure 3.3 shows the setup. We investigated the reduction of nitrobenzene to aniline in the flow system. The reaction solution consisted of 0.5 mM nitrobenzene and 150 mM ammonium formate in 2-propanol. Flow rates of 10 to 2 mL/h were tested under irradiation of 395 nm. High flow rates (e.g., 10 mL/h) hindered the conversion of nitrobenzene to aniline, while slower rates proved to be more effective with a rate of 2 mL/h yielding the most reproducible conversion. Figure 3.4A shows the UV-Vis spectra of sequential aliquots of the reaction solution collected at a flow rate of 2 mL/h. The peak at 258 nm corresponds to the unreacted nitrobenzene. As the reaction mixture flowed through the reaction chamber, the

nitrobenzene peak decreased, and the absorption feature of aniline increased. We monitored the absorbance of aniline and nitrobenzene at 236 and 258 nm, respectively. Figure 3.4B summarizes the average absorbance intensities of three trials at a flow rate of 2 mL/h. The initial volume (~2 mL) showed unreacted material because no equilibration with light was employed. As the solution flowed through under constant irradiation, the presence of aniline was detected consistently in the UV spectra. The flow system was used in back-to-back trials totalling 15 hours of irradiation and 30 mL of reaction solution with no observable drop in performance.

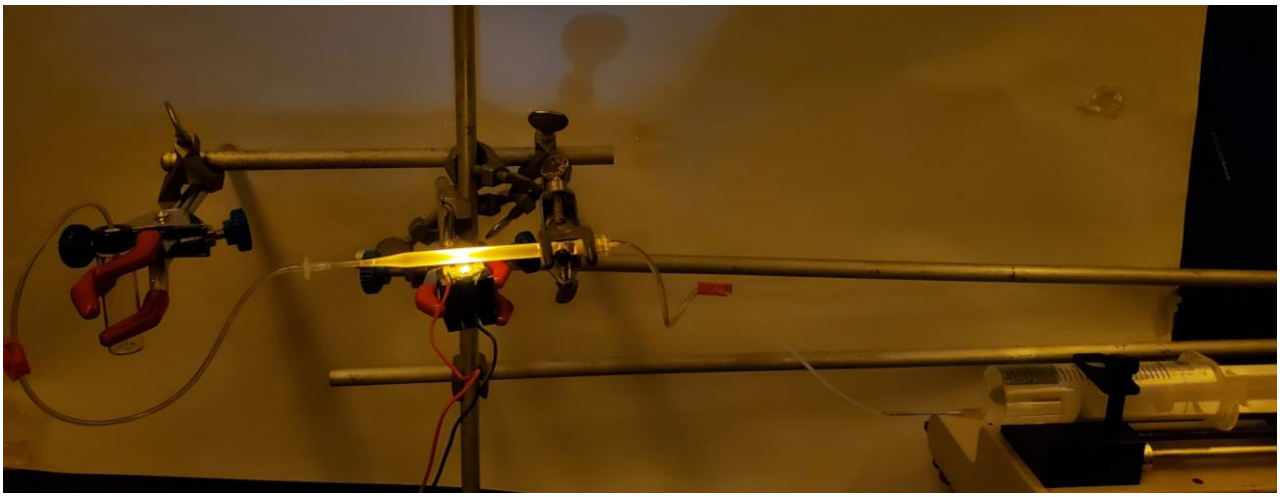

Figure 3.3. Mn-Doped CdS/ZnS coated pipette for use in a photocatalytic flow reactor under 395 nm illumination. Reaction mixture flowed at a rate of 2 mL/h through the QD-coated reaction chamber and collected in a 20 ml vial.

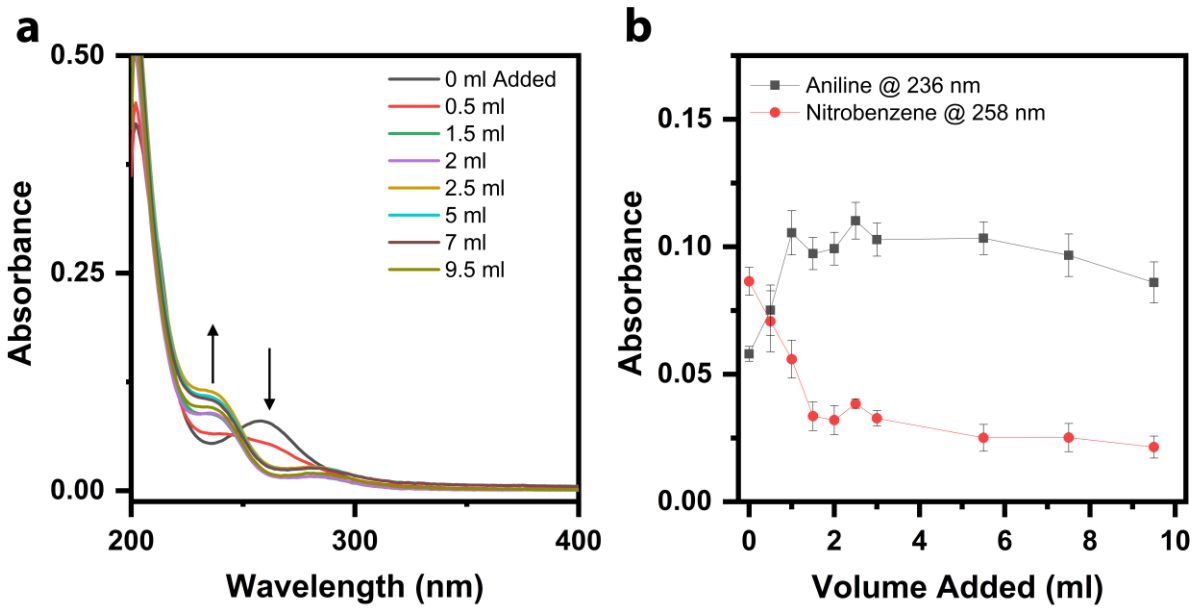

Figure 3.4. (A) UV absorption spectra of aliquots collected from the reaction at a flow rate of 2 mL/h. (B) Average of three trials showing the peak intensities at 236 nm (grey squares) from aniline and 258 nm (red circles) for nitrobenzene. Data points in the 0-2 mL range show unreacted material present in the connection tubing.

However, further optimization is still necessary. The ^{1}H NMR spectra of the post reaction solution do not show pure products. Figure 3.5 shows the proton NMR spectrum of the products obtained from the reaction under flow conditions. While aniline is present in the products, the broad peak down field, at ~7.2 ppm, suggests presence of other aromatics such as phenylhydroxylamine and nitrobenzene. Meanwhile the up-field signals could result from the ligands of detached QDs, such as oleylamine or the crosslinker heptane diamine. There are several factors that can contribute to the incomplete conversion of nitrobenzene to aniline, a 6-electron process, that mechanistically proceeds through multiple intermediate species (i.e. nitrosobenzene, phenylhydroxylamine) which can accumulate in the reaction solution and decrease yield.[12] The first two reduction steps are fast while the final conversion of phenylhydroxylamine to aniline is

slow. This limiting step leads to an accumulation of phenylhydroxylamine which can undergo condensation to azoxybenzene and azobenzene and subsequently yield aniline.[12] The various pathways that lead to the production of aniline can affect reproducibility and complicate the optimization of flow reactors. Additionally, surface interactions between the reactant and catalyst, together with diffusion limited proton transfer also need to be considered. [12]

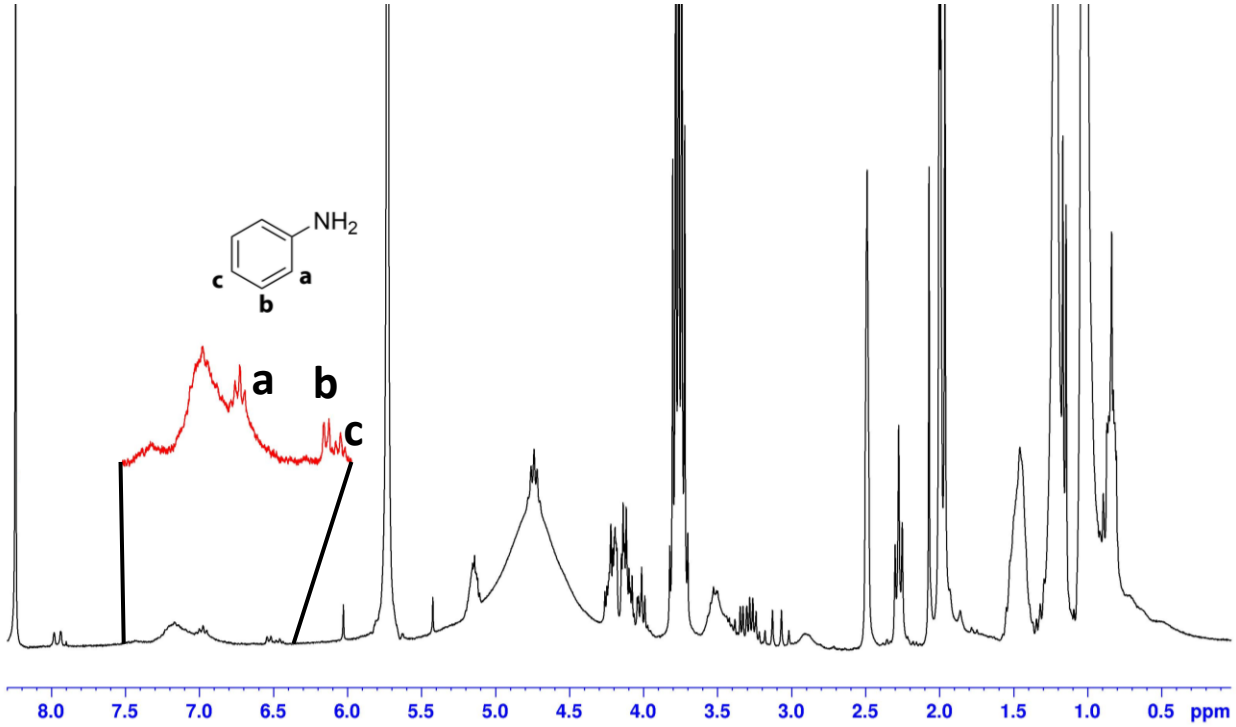

Figure 3.5. ^{1}H NMR spectrum of post reaction solution at a flow rate of 2 mL/h. Peaks at 6.47-6.52 ppm (c), 6.55-6.58 ppm (b), and 6.98-7.03 ppm (a) depict the presence of aniline. The broad peak downfield of aniline (~7.2 ppm) can be a combination of phenylhydroxylamine and nitrosobenzene.

Despite the reproducible UV absorption results, the flow rate of 2 mL/h might still be too fast for the reaction to go to completion because the process is diffusion driven. Second, the inefficiency in conversion may be attributed to the diameter of the flow reactor (~5 mm). In straight flow reactor, the flow is laminar with limited mixing of reactants. Capillary tubing (with a much smaller diameter) can overcome the problem of mixing by shortening the distance between the

reactants and photocatalysts. Additionally, due to the exponential attenuation of light distance, a narrower tubing can potentially improve the conversion via more uniform irradiation. However, a challenge with using capillaries is the effective coating of the walls with QDs. Narrow capillaries can be clogged by detached QDs or undesirable precipitates from the reaction mixture. The third factor is the presence of oxygen in the reaction solution that can be detrimental in the reduction of nitrobenzene. Oxygen molecules can easily react with any of the reaction intermediates and generate nitrobenzene or other biproducts. Therefore, a sealed reaction setup is crucial for an efficient conversion. Addressing these issues may improve the photocatalytic flow system to yield high efficiency and throughput.

There are several advantages of the flow system. It can increase the number of photocatalytic cycles of the Mn-Doped QD because the flow of the reaction mixture provides fresh sacrificial hole scavenger to the QD film. This rapid replenishment of the vacancies left by the hot electrons may inhibit detrimental processes such as loss of ligands and photo oxidation of the QD surface. Anilines are important intermediates in medicinal chemistry and are used to make a wide variety of products such as polymers, agricultural chemicals, synthetic dyes, and additives for the rubber industry. The mild and neutral conditions employed in the autonomous flow system are attractive for a variety of fields and eliminate the conventional commercial production methods that require pressurized hydrogen, expensive transition metal catalysts, and closed vessels. The preliminary work on the Mn-doped QD-coated flow reactor shows promising potential and may be expanded for use in other reactions including the hydrogenation of nitriles and reductions of alkyl or aryl azides.

3.3 Challenges and limitations of doped QDs as photocatalysts

Despite the superior performance of doped QDs to undoped QDs, some challenges remain. Successful doping is one of the main synthetic challenges of QDs. Self-purification processes take place during crystal growth and expel the dopants from QDs crystal structure. The dopants may end up on the surface of the QDs or in the reaction solution. Thus, after synthesis, every batch of doped QDs needs to be characterized extensively to determine size (TEM), dopant location (EPR), and dopant concentration (ICP-OES). Some of these characterization methods can be costly. Also, an in-depth understanding of the photophysical processes, specifically the generation and the fate of hot electrons during photoexcitation, needs to be established for a broader implementation of QDs in photocatalytic applications. Lastly, the stability of the photocatalyst is key. In the case of QDs, photodegradation from accumulated holes causes oxidation of ligands which fall off and expose the material. Unrestricted oxidation severely diminishes the performance of the QDs as catalysts. Thus, the determination of sacrificial agents which efficiently quench the photogenerated holes is a key aspect in increasing the reusability of QDs. Additionally, treating the films with the crosslinker between reactions can help increase their lifetime. Addressing these challenges will significantly improve the chances of the large-scale implementation of QDs in photocatalysis.

3.4 Future directions

Reviews by MacMillan[13–15] outline a plethora of well-characterized photoredox reactions catalyzed by transition metal complexes, some of which we hypothesize that doped QDs can potentially substitute. Figure 3.2 depicts three potential reactions where the QDs may replace the $Ru(bpy)_3Cl_2$. Figure 3.5A and B show net reductive and net oxidative reactions respectively. In these types of reactions sacrificial hole scavengers or electron sources are necessary. Figure 3.5C shows a redox neutral reaction which does not require additional reagents. Utilisation of QDs as

films in redox neutral reactions can prove advantageous in simplifying the reaction setup, catalyst recovery, and post reaction workup procedures.

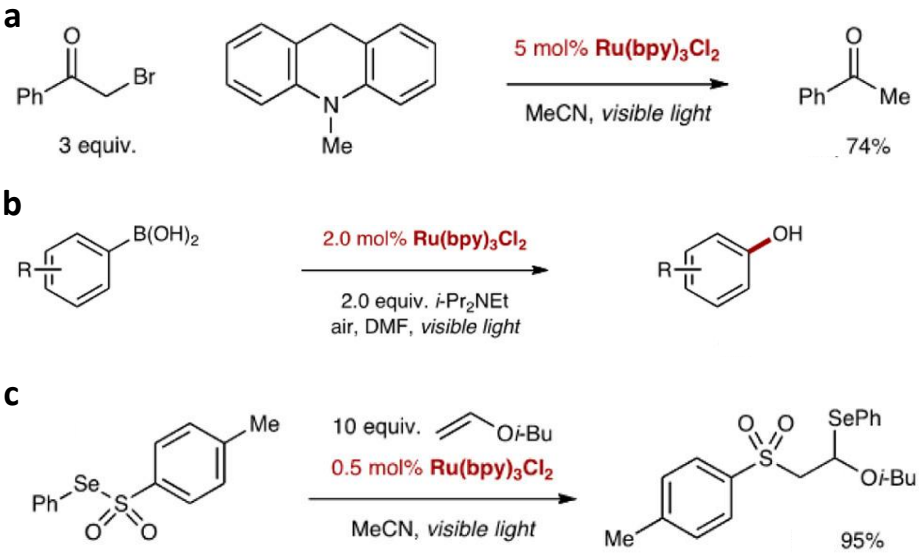

Figure 3.6. (A) Reductive dehalogenation of phenacyl bromide. (B) Oxidative hydroxylation of arylboronic acids. (C) Radical addition of *Se*-phenyl *p*-tolueneselenosulfonate to allkyl vinyl ethers. Reprinted with permission from reference 13.

The formation of carbon-carbon bonds is a crucial aspect of synthetic organic chemistry. A prospective research direction is the implementation of doped QDs as sensitizers in traditional cross-coupling reactions. Almost all cross-coupling reaction involve oxidative addition of a metal centre followed by a transmetalation step and a reductive elimination step.[7] Photogenerated electrons and holes in the doped QDs can potentially improve the oxidation and reduction of metal centres and increase the efficiency of catalytic cycles. Figure 3.6 shows a proposed mechanism where the conventional iridium photocatalyst acts a sensitizer for the nickel catalytic cycle in a cross-coupling reaction. We propose that transition-metal cross-coupling reactions including copper,[16] nickel,[17] cobalt,[18] palladium[19] can be adapted with doped QDs as sensitizers where QDs can perform single electron transfer to either the nickel catalyst or to the reactants heterogeneously.

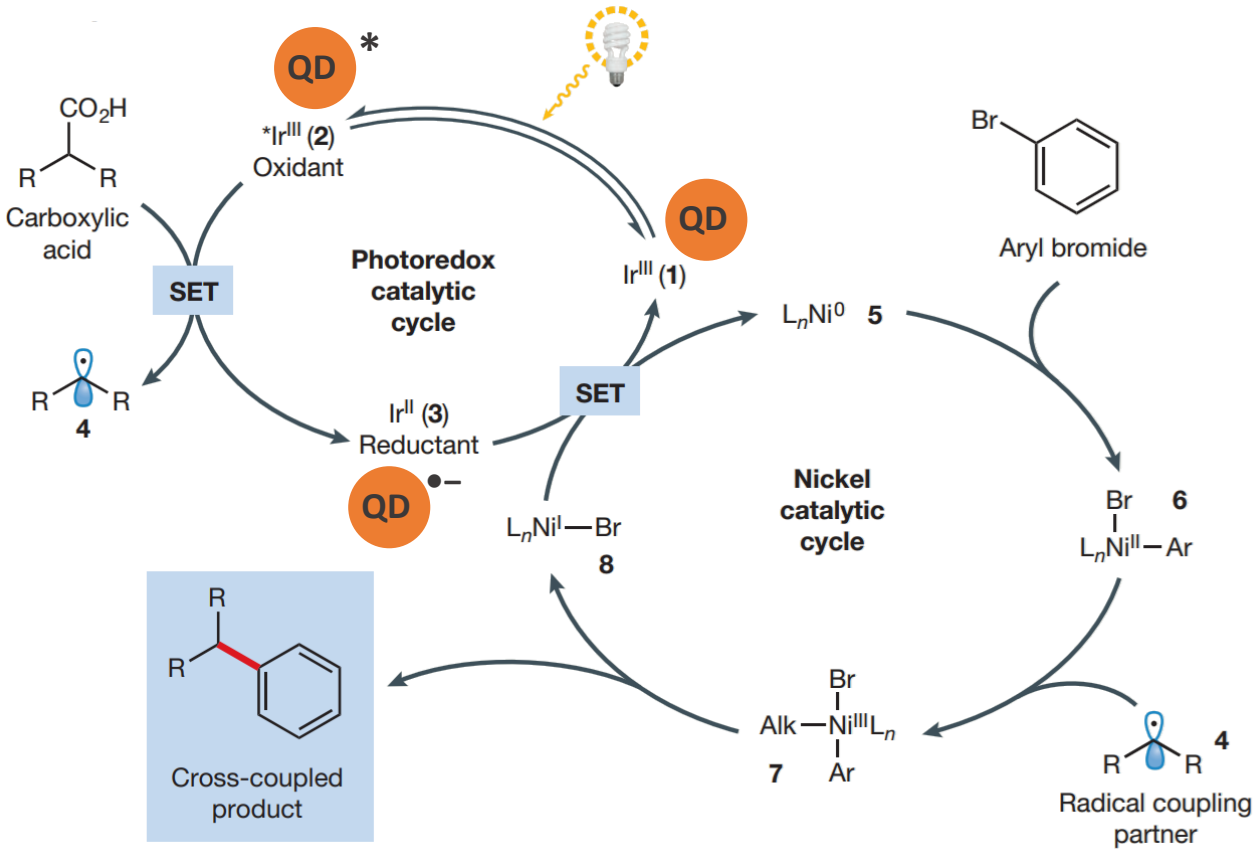

Figure 3.7. Proposed mechanism for carbon-carbon cross coupling reaction where photoredox catalysis is used in tandem with the nickel catalytic cycle. Replacing the photoredox cycle of iridium with doped QDs may increase the efficiency of the reaction. Reprinted with permission from reference 14.

Finally, flow reactors are emerging platforms in synthetic organic chemistry. With respect to photocatalysis, flow reactors are highly desirable over batch processes. One of the limitations of photochemical reactions in largescale batch processes is that light intensity decreases exponentially with distance as described by Beer-Lambert law. Utilizing a thin and long reactor with light source distributed along its length can therefore circumvent this issue. However, shifting from well established batch reactions to flow processes remains a challenge due to the high number of parameters that need to be optimized. These needs can be addressed by utilizing the high-throughput experimentation (HTE) method, such as a 96-well plate, to investigate batch conditions

under illumination for use in flow reactors.[9] Figure 6.1 depicts the translation of batch reaction to flow reaction via HTE. The microscale size of the reactions in a 96-well place mimics the flow reaction conditions.

Our initial work with immobilized Mn-doped QDs as flow reactor coatings, instead of the homogeneous transition metal complexes, shows that heterogeneous photocatalysts can potentially simplify the adaptation of batch conditions to flow systems. We propose that multiple reaction solutions can be set up in vials and connected to an array of photocatalyst-coated flow reactor chambers. This array of QD-coated reaction chambers can investigate several reaction conditions in parallel. The parallel flow setup can provide a high throughput platform for integrating doped QDs instead of iridium and ruthenium complexes in photoredox reactions, with a significant

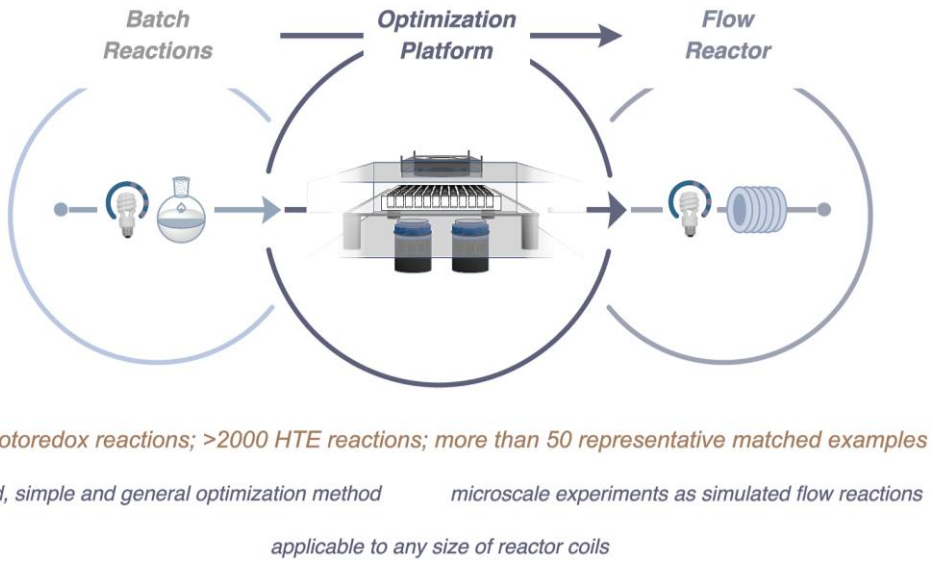

Figure 3.8. Translation of batch reaction to flow reactor via HTE. Reprinted with permission from reference 10. License link https://creativecommons.org/licenses/by-nc-nd/4.0/legalcode

reduction in post-reaction work up. Once the flow conditions of a specific reaction have effectively been optimized, these arrays can be used in parallel to increase output. The adaptation of parallel arrays of catalyst-coated tubing is feasible because of the low cost, reusability, and facile assembly

of the QD films. Work on increasing the stability of the QDs would further improve the reusability of these arrays.

3.5 References

1. Rehm, T. H. Flow Photochemistry as a Tool in Organic Synthesis. *Chem. – A Eur. J.* **26**, 16952–16974 (2020).
2. Wegner, J., Ceylan, S. & Kirschning, A. Ten key issues in modern flow chemistry. *Chem. Commun.* **47**, 4583–4592 (2011).
3. Sambiagio, C. & Noël, T. Flow Photochemistry: Shine Some Light on Those Tubes! *Trends Chem.* **2**, 92–106 (2020).
4. Hartman, R. L., McMullen, J. P. & Jensen, K. F. Deciding Whether To Go with the Flow: Evaluating the Merits of Flow Reactors for Synthesis. *Angew. Chemie Int. Ed.* **50**, 7502–7519 (2011).
5. Frost, C. G. & Mutton, L. Heterogeneous catalytic synthesis using microreactor technology. *Green Chem.* **12**, 1687–1703 (2010).
6. McQuade, D. T. & Seeberger, P. H. Applying Flow Chemistry: Methods, Materials, and Multistep Synthesis. *J. Org. Chem.* **78**, 6384–6389 (2013).
7. McAtee, R. C., McClain, E. J. & Stephenson, C. R. J. Illuminating Photoredox Catalysis. *Trends Chem.* **1**, 111–125 (2019).
8. Rehm, T. H. Reactor Technology Concepts for Flow Photochemistry. *ChemPhotoChem* **4**, 235–254 (2020).
9. González-Esguevillas, M. *et al.* Rapid Optimization of Photoredox Reactions for Continuous-Flow Systems Using Microscale Batch Technology. *ACS Cent. Sci.* **7**, 1126–1134 (2021).
10. Yang, C. *et al.* Heterogeneous photoredox flow chemistry for the scalable organosynthesis of fine chemicals. *Nat. Commun.* **11**, 1239 (2020).
11. Lazar, M. A., Varghese, S. & Nair, S. S. Photocatalytic Water Treatment by Titanium Dioxide: Recent Updates. *Catalysts* vol. 2 572–601 (2012).
12. Zhu, P., Liu, M. & Zheng, Z. Catalysis Science & Technology nitrobenzene reduction reaction †. 6681–6690 (2019) doi:10.1039/c9cy01257e.
13. Prier, C. K., Rankic, D. A. & MacMillan, D. W. C. Visible Light Photoredox Catalysis with Transition Metal Complexes: Applications in Organic Synthesis. *Chem. Rev.* **113**, 5322–5363 (2013).
14. Twilton, J. *et al.* The merger of transition metal and photocatalysis. *Nat. Rev. Chem.* **1**, (2017).
15. Shaw, M. H., Twilton, J. & MacMillan, D. W. C. Photoredox Catalysis in Organic Chemistry. *Journal of Organic Chemistry* vol. 81 6898–6926 (2016).
16. Creutz, S. E., Lotito, K. J., Fu, G. C. & Peters, J. C. Photoinduced Ullmann C–N Coupling: Demonstrating the Viability of a Radical Pathway. *Science (80-.).* **338**, 647–651 (2012).

17. Zuo, Z. *et al.* Merging photoredox with nickel catalysis: Coupling of α-carboxyl sp3-carbons with aryl halides. *Science (80-.).* **345**, 437–440 (2014).

18. Ruhl, K. E. & Rovis, T. Visible Light-Gated Cobalt Catalysis for a Spatially and Temporally Resolved [2+2+2] Cycloaddition. *J. Am. Chem. Soc.* **138**, 15527–15530 (2016).

19. Kalyani, D., McMurtrey, K. B., Neufeldt, S. R. & Sanford, M. S. Room-Temperature C–H Arylation: Merger of Pd-Catalyzed C–H Functionalization and Visible-Light Photocatalysis. *J. Am. Chem. Soc.* **133**, 18566–18569 (2011).

Part Two: Sequence-specific DNA-Gold Nanoparticles as High Mass Probes in Imaging Mass Cytometry

(An industrial collaboration with Fluidigm Inc.)

Chapter 4 – Introduction to Biomarkers, MicroRNAs (miRNA), Localized Surface Plasmon Resonance (LSPR), and Imaging Mass Cytometry (IMC)

4.1 Biomarkers

The importance of biomarkers cannot be overstated. Generally, a biomarker is an indicator that identifies and describes health, disease, or disorder. In the early stages of medicine, biomarkers were physical observables such as pulse, blood pressure and bodyweight. The scope of what defines a biomarker has rapidly expanded with scientific and technological advances. Today, the term biomarker typically refers to specific biological entities such as molecules or proteins that can be reliably detected and quantified, in turn providing insight on the onset and progression of a specific disease or disorder.[1] The utilization of biomarkers as predictive means allows for rapid diagnosis of disorders, delivery of specific information, and ample time for treatment.[2] Some common and well studied biomarkers in blood serum include troponin (myocardial infraction)[3], carcinoembryonic antigen (various cancers),[4] and amino transferases (liver disease).[5] Additionally, biomarkers can be detected not only in blood, but in urine, saliva, breath, and sweat.

The constant advancement in technological and medical fields demands new, accurate, and specific biomarkers, primarily for implementation in precision medicine. First, the ideal biomarker needs to be easily detected. Second, it should be specific to the disease or disorder that it is linked to. Third, the biomarker should be detected prior to the onset of symptoms and its quantity should change with disease development or treatment.[6] Finally, the methods for the detection of the biomarkers should be transferable from the research to clinical settings. New biomarkers that fully satisfy the above criteria are hard to come by. The lack of clinically significant proteins highly specific to a disease, and a shortage of robust detection methods, deter the translation of new biomarkers.[7,8] However, efforts to expand the spectrum of potential candidates have persisted.

The first detection of cell-free nucleic acid (cfNA) in human blood was reported in 1948 by Mandel an Metais.[9] The importance of the discovery was not appreciated until 1994, when cfNA, comprising DNA and messenger RNA (mRNA) and microRNA (miRNA), in blood was directly linked to cancer.[10,11] However, the potential of RNA as a biomarker was initially dismissed due to its instability and the elevated amounts of nucleases present in plasma. These claims were eventually overturned, and it was established that the detection of cfNA in serum could improve diagnosis while circumventing invasive tumor biopsies.[12] Additionally, cfNA levels are elevated not only in cancer patients, but also in patients with inflammatory disease and tissue trauma.[13] This new class of biomarkers has proven promising for cancer and various other disorders.

4.2 MicroRNA

Of all the cfNAs discovered in blood, miRNAs attracted the most attention, primarily because they were a newly discovered class of nucleic acids in 1993.[14] Since then, miRNAs have been found in all animals studied. MiRNAs are short, non-coding RNAs ranging from 17-22 nucleotides in length.[14,15] Generally, they are transcribed from DNA and undergo extensive modifications to reach their final form.[16,17] They are important mediators in gene regulation and serve critical roles in animal development. The specific mechanisms by which miR-210 controls gene regulation depend on the target mRNA molecules it interacts with. In general, the binding miRNA-210 to the 3' untranslated region (UTR) of target mRNA, typically through a short complementary sequence of nucleotides known as the seed region, leads to either degradation of the mRNA molecule or inhibition of its translation into protein.[15,16] The degradation of mRNA can occur through the activity of RNA-induced silencing complex (RISC) or miRNA-mediated deadenylating. Inhibition of mRNA translation occurs through steric hindrance or interference with translation initiation factors. The binding specificity of miRNA-210 is further influenced by

other factors, including the abundance of the miRNA and its target mRNA, as well as the presence of other RNA-binding proteins that can compete with the miRNA for binding to the mRNA.[15-17] Atypical expressions of these miRNAs can be linked to various diseases and cancers,[16,18] and their presence in extracellular fluids makes them excellent candidates as biomarkers. The discovery of miRNAs opened new avenues in the field of molecular biology, genetics, and biomarkers.

The first use of miRNA as a biomarker, for non-Hodgkin lymphoma, was reported in 2008.[19] With well established methods for the detection and amplification (qRT-PCR) of nucleic acids, the exploration of miRNAs as biomarkers rapidly increased.[20] MiRNAs have the potential to surpass proteins as biomarkers due to the ease of implementing them in multimarker panels, which are crucial for the diagnosis cancer – a heterogenous disease.[21] A panel utilizing nine miRNAs has reportedly improved the diagnosis of breast cancer.[22] Finally, multimarker panels of miRNAs can provide patient specific diagnosis and treatment. Since their discovery, the scope of studies of miRNAs has expanded to other disorders such as preeclampsia.[23]

A human placenta contains upwards of 600 miRNAs with miRNA-210 as the most studied one: specifically in its relation to preeclampsia.[24] Preeclampsia is a pregnancy-specific disorder which affects 5-8% of pregnant women, and its onset is difficult to predict. It is a leading cause of maternal and neonatal mortality.[25] Extensive studies have shown that miRNA-210 is upregulated with the onset of preeclampsia and it has potential to serve as a biomarker.[26] Furthermore, the overexpression of miRNA-210 can be induced under low oxygen (hypoxic) condition, not only in endothelial and tumor cells but also in cultured trophoblasts.[27] Thus, it can serve as a model molecule to study and for developing new technologies for its detection as biomarkers.

4.3 Gold nanoparticles

Localized surface plasmon resonance (LSPR) is a phenomenon in various metal nanoparticles that results in enhanced extinction cross sections. Most commonly, gold (AuNP) and silver nanoparticles have been implemented in various applications such as diagnostics, sensing, imaging and photothermal therapy.[28,29] Additionally, noble metal nanoparticles, can be easily modified with polymers, proteins, and DNA. Particularly, DNA conjugated AuNP have become attractive candidates to study biological systems such as cells and tissues using confocal microscopy, and flow cytometry.

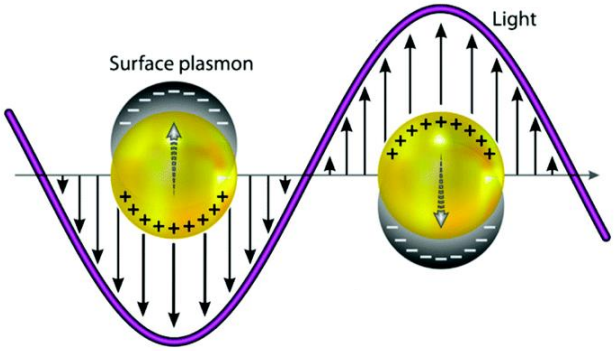

Figure 4.1. Interaction with the electric field of light shifts the conduction electrons of the nanoparticle, giving rise to a dipole. The oscillation of this dipole results in intense colours. Reprinted with permission from reference 30.

LSPR refers to the collective oscillation of surface electrons on a noble metal nanoparticle with dimensions much smaller than the wavelength of light (Figure 4.1).[30] The high surface to volume ratio of the nanoparticles results in the exposure of the free electrons to the electric field of incident light which triggers the collective oscillation of the free electrons on the nanoparticles. At specific wavelengths, these oscillations resonate, polarizing the particle and increasing the extinction cross section. Mie theory describes the LSPR phenomenon.[31]

$$C_{ext} = \frac{24\pi^3 \varepsilon_{med}^{1.5} R^3 N}{\lambda} \frac{\varepsilon_i}{[\varepsilon_r + \chi\varepsilon_{med}]^2 + \varepsilon_i^2} \qquad \textbf{Equation 4.1}$$

Equation 4.1 depicts the relationship of the extinction cross section to nanoparticle radius (R), wavelength (λ), electron density (N), dielectric constant of the medium (ε_{med}), and ε_i and ε_r which are the imaginary and real components of the dielectric function of the bulk metal. Finally, χ, describes the effect of shape on the polarization of surface electron under incident light.[31,32]

Extinction cross-section reaches a maximum when the condition $\varepsilon_r = -\chi\varepsilon_{med}$ is satisfied, where resonance is achieved and the characteristic LSPR peak is observed.[31–33] For noble metal nanoparticles such as Au and Ag this phenomenon occurs in the visible region, hence giving rise to their use in sensing and imaging applications. Factors such as size, electron density, and the imaginary components of the dielectric function, which depend on intrinsic properties of the metal, can affect the LSPR peak position and shape. Typically, the smaller dielectric function of Ag, yields sharper peaks and more tunable extinction spectra than Au[34]. However, AuNP are more widely used due to their stability.

4.4 DNA-AuNP

Conjugation of AuNPs with sequence-specific DNA strands (denoted as DNA-AuNP) permits for the implementation of these nanoparticles in a wider range of applications when compared with the bare AuNP. Single-stranded DNA (ssDNA) on AuNPs can improve their biocompatibility, facilitate installation of fluorescent probes, and increase colloidal stability.[35,36] Additionally, DNA-AuNPs with unique sequences that bind to a specific target can serve as probes and signal generators in sensing methods.[37] These DNA-AuNP systems have been used to

investigate nanoparticle uptake and mRNA detection. Specifically, nanoflares developed by Mirkin et al. are available as commercial kits for the detection of RNA.[38]

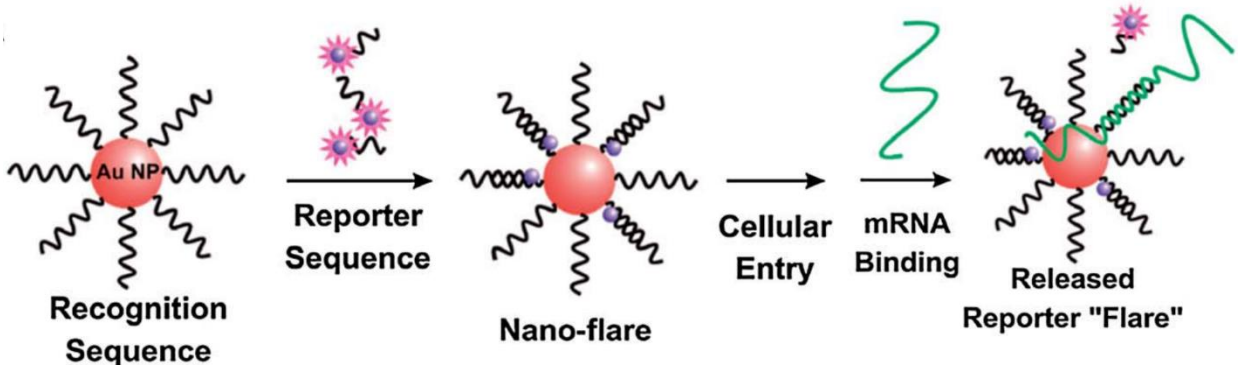

Figure 4.2. Illustration of nanoflare system developed by Mirkin et al. Hybridization of the recognition sequence on the AuNP with a dye labeled reporter sequence orients the dye close to the AuNP surface, quenching its fluorescence. Upon cell entry, the mRNA target displaces the reporter sequences restoring the fluorescence of the dye. Reprinted with permission from reference 38. Copyright 2009 American Chemical Society.

Nano-flares are DNA-AuNP conjugates that function as reporters in cellular uptake processes, and probes to detect mRNA binding.[39] They utilize the distance-dependent fluorescence quenching capabilities of AuNP to generate an optical signal.[40,41] Figure 4.2 depicts the nanoflare system with mRNA as a target molecule with sequence-specific ssDNA on the AuNP as a recognition agent.[42] A short reporter sequence tagged with a fluorescent molecule (Cy5), hybridizes to the ssDNA on the nanoparticles with the Cy5-terminated end in proximity to the nanoparticle. Nonradiative energy transfer from the Cy5 to the AuNP keeps the dye dark.[43] Binding of the target nucleic acid displaces the shorter reporter strand, the fluorescence of which restores when far enough from the AuNP (Figure 4.2). Fluorescence-based methods suffer from weak signals and bleaching, especially when used for detecting low abundant targets such as miRNAs. Therefore, an alternative technique capable of detecting low abundant species is sought after.

4.5 Imaging mass cytometry

Imaging mass cytometry (IMC), a method that analyzes fixed cells, couples traditional mass cytometry, with a laser ablation technique to generate multiplexed images of cells and tissues.[44] IMC utilizes antibodies conjugated with high mass probes, typically stable isotopes of transition metals in the lanthanide series. Its mode of operation involves treating slides of immobilised cells or tissue sections with various lanthanide-tagged antibodies and intercalators as stains followed by laser ablation and time-of-flight (TOF) mass spectrometry. A pulsed laser (213 nm) with a 1 µm diameter spot size scans the slide and vaporizes each spot sequentially. A carrier

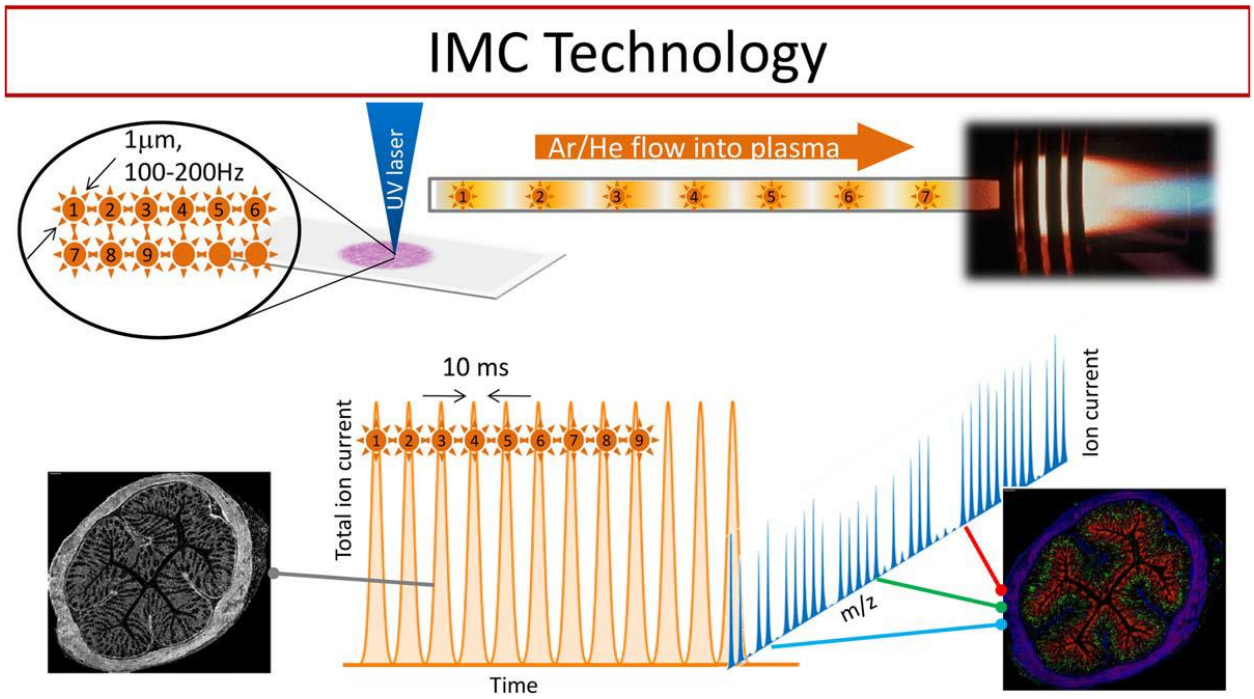

Figure 4.3. Principle of operation of Imaging Mass Cytometry. (TOP) Lanthanide-labelled samples are ablated with a laser 1 µm in diameter. The plume of ions is ionized in an ICP torch then analyzed with a time-of-flight mass analyzer. (BOTTOM) Each ablated spot corresponds to one image pixel and is generated by collecting the m/z signal over a 10 ms time window. Signals corresponding to various ions from the same ablated spot are then overlaid to generate multiplexed images. Reprinted with permission from reference 44.

gas transports the plume of particles to the inductively coupled plasma (ICP) ionizer. Then, a TOF analyzer separates the ions based on mass to charge ratio. The ions of interest, i.e. the high mass lanthanides, are indexed with each spot on the slide ultimately producing an intensity map of all the targeted components in the cell or tissue.[44,45] Figure 4.3 depicts the process.

The resolution of ~1 μm in IMC enables the interrogation of subcellular components, biomarkers, and signalling pathways. A higher resolution, of less than 1 μm spot size, is possible at the cost of a reduced sensitivity because a smaller spot size results in fewer ions. The resolution also depends on the frequency of ablation (spots/s); a higher frequency results in a decrease in resolution because of cross contamination of the plumes from individual spots. The resolution of IMC is higher than Matrix Assisted Laser Deposition Ionization (MALDI) which ranges from 3 to 5 μm.[44,46] Generally, a 1 mm^2 square area on the slide can be scanned in approximately 2 hours using IMC. Coupled with cell segmentation software and bioinformatic tools, IMC is emerging as a powerful tool for cellular and tissue analysis.

One of the main advantages of IMC is its multiplexing capabilities. The CyTOF technology produces highly resolved signals from lanthanide ions that are conjugated to antibodies.[47,48] This overcomes the main drawback of spectral overlaps of dyes in immunofluorescence methods. While standard immunofluorescence methods utilize up to four tags simultaneously, IMC can implement and resolve up to 37 tags without overlap.[44] On the other hand, one challenge with IMC lies in the detection of low amounts of target proteins or biomarkers. Low levels of protein target lead to few bound metal-tagged antibodies and low signal intensity. Additionally, the detection of nucleic acids, such as miRNA, by IMC has not been demonstrated.

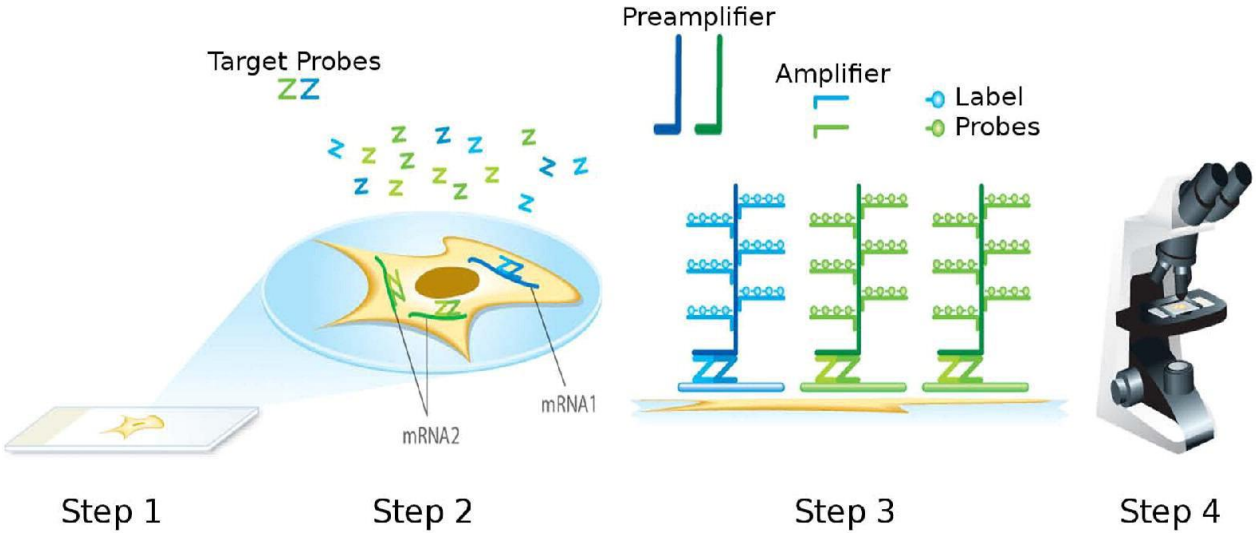

Figure 4.4. Diagram of the RNAscope assay mode of operation. (Step 1) Tissues or cells are fixed and permeabilized. (Step 2) Tissues or cells are incubated with RNA-sequence specific Z probes. (Step 3) Multiple signal amplification species are introduced comprising amplifiers, labels, and probes. (Step 4) Conventionally imaged with fluorescent microscope. Reprinted with permission from reference 49.

Detecting and imaging RNA in cells are difficult. Figure 4.4 depicts one of the few methods for detecting mRNA, known as the RNAscope assay. This assay utilizes various sequence-specific recognition factors (Z probes) that bind to mRNAs of fixed cells. Then, a cascade of signal amplification molecules and fluorescent labels (or mass labels) self assemble onto these Z probes. The cells can then be imaged with a fluorescent microscope[49] or IMC. While this assay works for mRNA, it is not transferrable to miRNAs. The short sequence of miRNAs (17-22 nucleotides) does not allow for sufficient Z probes to hybridize and thus diminishes the signal amplification cascade. Therefore, alternative mass probes are desirable and critically needed for detecting low abundant nucleic acids, such as miRNAs, by IMC.

The scope of the second part of the dissertation explores DNA-AuNPs for imaging low abundant miRNAs in human trophoblast cells. The target-specific DNA serves as a recognition element (for miRNA-210) and the AuNP serves as a high-mass probe with approximately 10 000

atoms for signal amplification. Compared with the IMC's limit of detection, >400 ions/μm^2, a single binding event of a gold nanoparticle provides ample signal low abundant molecules. Overall, we investigated the cellular uptake DNA-AuNP by imaging mass cytometry in comparison with traditional confocal microscopy utilizing the AuNP nanoflares. The work is the first exploration of nanoparticles as high-mass probes in the field of imaging mass cytometry.

4.6 References

1. Aronson, J. K. & Ferner, R. E. Biomarkers—A General Review. *Curr. Protoc. Pharmacol.* **76**, 9.23.1-9.23.17 (2017).

2. Aronson, J. K. An agenda for UK clinical pharmacology: Research priorities in biomarkers and surrogate end-points. *Br. J. Clin. Pharmacol.* **73**, 900–907 (2012).

3. Preliminary report: effect of encainide and flecainide on mortality in a randomized trial of arrhythmia suppression after myocardial infarction. *N. Engl. J. Med.* **321**, 406–412 (1989).

4. Engelen, M. J. *et al.* Serum CA 125, carcinoembryonic antigen, and CA 19-9 as tumor markers in borderline ovarian tumors. *Gynecol. Oncol.* **78**, 16–20 (2000).

5. Ferner, R. E., Dear, J. W. & Bateman, D. N. Management of paracetamol poisoning. *BMJ* **342**, d2218 (2011).

6. FitzGerald, G. A. Measure for Measure: Biomarker standards and transparency. *Sci. Transl. Med.* **8**, 343fs10 (2016).

7. MacLean, E. *et al.* A systematic review of biomarkers to detect active tuberculosis. *Nat. Microbiol.* **4**, 748–758 (2019).

8. Jortani, S. A., Prabhu, S. D. & Valdes, R. J. Strategies for developing biomarkers of heart failure. *Clin. Chem.* **50**, 265–278 (2004).

9. MANDEL, P. & METAIS, P. [Nuclear Acids In Human Blood Plasma]. *C. R. Seances Soc. Biol. Fil.* **142**, 241–243 (1948).

10. Vasioukhin, V. *et al.* Point mutations of the N-ras gene in the blood plasma DNA of patients with myelodysplastic syndrome or acute myelogenous leukaemia. *Br. J. Haematol.* **86**, 774–779 (1994).

11. Sorenson, G. D. *et al.* Soluble normal and mutated DNA sequences from single-copy genes in human blood. *Cancer Epidemiol. biomarkers Prev. a Publ. Am. Assoc. Cancer Res. cosponsored by Am. Soc. Prev. Oncol.* **3**, 67–71 (1994).

12. Schwarzenbach, H., Hoon, D. S. B. & Pantel, K. Cell-free nucleic acids as biomarkers in cancer patients. *Nat. Rev. Cancer* **11**, 426–437 (2011).

13. Swaminathan, R. & Butt, A. N. Circulating nucleic acids in plasma and serum: recent developments. *Ann. N. Y. Acad. Sci.* **1075**, 1–9 (2006).

14. O'Brien, J., Hayder, H., Zayed, Y. & Peng, C. Overview of MicroRNA Biogenesis, Mechanisms of Actions, and Circulation . *Frontiers in Endocrinology* vol. 9 (2018).

15. Pasquinelli, A. E. MicroRNAs: Heralds of the noncoding RNA revolution. *Rna* **21**, 709–710 (2015).

16. Gustafson, D. *et al.* How to measure miRNA expression Expansion of microRNA research. *Methods* **8**, 358–369 (2016).

17. Pasquinelli, A. E. A sense-able microRNA. *Genes Dev.* **30**, 2019–2020 (2016).

18. Broughton, J. P. & Pasquinelli, A. E. A tale of two sequences: MicroRNA-target chimeric reads. *Genet. Sel. Evol.* **48**, 1–7 (2016).

19. Navarro, A. *et al.* MicroRNA expression profiling in classic Hodgkin lymphoma. *Blood* **111**, 2825–2832 (2008).

20. Gudnason, H., Dufva, M., Bang, D. D. & Wolff, A. Comparison of multiple DNA dyes for real-time PCR: Effects of dye concentration and sequence composition on DNA amplification and melting temperature. *Nucleic Acids Res.* **35**, 1–8 (2007).

21. Alhasan, A. H. *et al.* Scanometric MicroRNA array profiling of prostate cancer markers using spherical nucleic acid-gold nanoparticle conjugates. *Anal. Chem.* **84**, 4153–4160 (2012).

22. Cuk, K. *et al.* Plasma MicroRNA Panel for Minimally Invasive Detection of Breast Cancer. *PLoS One* **8**, e76729 (2013).

23. Condrat, C. E. *et al.* miRNAs as Biomarkers in Disease: Latest Findings Regarding Their Role in Diagnosis and Prognosis. *Cells* **9**, (2020).

24. Luo, R. *et al.* MicroRNA-210 Contributes to Preeclampsia by Downregulating Potassium Channel Modulatory Factor 1. *Hypertension* **64**, 839–845 (2014).

25. Jairajpuri, D. S., Malalla, Z. H., Mahmood, N. & Almawi, W. Y. Circulating microRNA expression as predictor of preeclampsia and its severity. *Gene* **627**, 543–548 (2017).

26. Chen, D. & Wang, W. Human placental microRNAs and preeclampsia. *Biol. Reprod.* **88**, 130 (2013).

27. Jaszczuk, I. *et al.* The role of miRNA-210 in pre-eclampsia development. *Ann. Med.* **54**, 1350–1356 (2022).

28. Jain, P. K., Huang, X., El-Sayed, I. H. & El-Sayed, M. A. Noble Metals on the Nanoscale: Optical and Photothermal Properties and Some Applications in Imaging, Sensing, Biology, and Medicine. *Acc. Chem. Res.* **41**, 1578–1586 (2008).

29. Lee, K.-S. & El-Sayed, M. A. Gold and Silver Nanoparticles in Sensing and Imaging: Sensitivity of Plasmon Response to Size, Shape, and Metal Composition. *J. Phys. Chem. B* **110**, 19220–19225 (2006).

30. Masson, J.-F. Portable and field-deployed surface plasmon resonance and plasmonic sensors. *Analyst* **145**, 3776–3800 (2020)..

31. Mie, G. Beiträge zur Optik trüber Medien, speziell kolloidaler Metallösungen. *Ann. Phys.* **330**, 377–445 (1908).

32. Petryayeva, E. & Krull, U. J. Localized surface plasmon resonance: Nanostructures, bioassays and biosensing—A review. *Anal. Chim. Acta* **706**, 8–24 (2011).

33. Johnson, P. B. & Christy, R. W. Optical Constants of the Noble Metals. *Phys. Rev. B* **6**, 4370–4379 (1972).

34. Jensen, T. R. *et al.* Nanosphere Lithography: Effect of the External Dielectric Medium on

the Surface Plasmon Resonance Spectrum of a Periodic Array of Silver Nanoparticles. *J. Phys. Chem. B* **103**, 9846–9853 (1999).

35. Liu, B. & Liu, J. Methods for preparing DNA-functionalized gold nanoparticles, a key reagent of bioanalytical chemistry. *Anal. Methods* **9**, 2633–2643 (2017).

36. Giljohann, D. A. *et al.* Gold nanoparticles for biology and medicine. *Angew. Chemie - Int. Ed.* **49**, 3280–3294 (2010).

37. Zhang, S., Geryak, R., Geldmeier, J., Kim, S. & Tsukruk, V. V. Synthesis, Assembly, and Applications of Hybrid Nanostructures for Biosensing. *Chemical Reviews* vol. 117 12942–13038 (2017).

38. Zheng, D., Seferos, D. S., Giljohann, D. A., Patel, P. C. & Mirkin, C. A. Aptamer nano-flares for molecular detection in living cells. *Nano Lett.* **9**, 3258–3261 (2009).

39. Seferos, D. S., Giljohann, D. A., Hill, H. D., Prigodich, A. E. & Mirkin, C. A. Nano-Flares: Probes for Transfection and mRNA Detection in Living Cells. *J. Am. Chem. Soc.* **129**, 15477–15479 (2007).

40. Heuer-Jungemann, A., Harimech, P. K., Brown, T. & Kanaras, A. G. Gold nanoparticles and fluorescently-labelled DNA as a platform for biological sensing. *Nanoscale* **5**, 9503–9510 (2013).

41. Briley, W. E., Bondy, M. H., Randeria, P. S., Dupper, T. J. & Mirkin, C. A. Quantification and real-time tracking of RNA in live cells using Sticky-flares. *Proc. Natl. Acad. Sci. U. S. A.* **112**, 9591–9595 (2015).

42. Prigodich, A. E. *et al.* Multiplexed Nanoflares: mRNA Detection in Live Cells. *Anal. Chem.* **84**, 2062–2066 (2012).

43. Tu, Y., Wu, P., Zhang, H. & Cai, C. Fluorescence quenching of gold nanoparticles integrating with a conformation-switched hairpin oligonucleotide probe for microRNA detection. *Chem. Commun.* **48**, 10718–10720 (2012).

44. Chang, Q. *et al.* Imaging Mass Cytometry. *Cytom. Part A* **91**, 160–169 (2017).

45. Chang, Q. *et al.* Biodistribution of cisplatin revealed by imaging mass cytometry identifies extensive collagen binding in tumor and normal tissues. *Sci. Rep.* **6**, 1–11 (2016).

46. Bouzekri, A., Esch, A. & Ornatsky, O. Multidimensional profiling of drug-treated cells by Imaging Mass Cytometry. *FEBS Open Bio* **9**, 1652–1669 (2019).

47. Ali, H. R. *et al.* Imaging mass cytometry and multiplatform genomics define the phenogenomic landscape of breast cancer. *Nat. Cancer* **1**, 163–175 (2020).

48. Wang, Y. J. *et al.* Multiplexed In Situ Imaging Mass Cytometry Analysis of the Human Endocrine Pancreas and Immune System in Type 1 Diabetes. *Cell Metab.* **29**, 769-783.e4 (2019).

49. Wang, F. *et al.* RNAscope: A Novel in Situ RNA Analysis Platform for Formalin-Fixed, Paraffin-Embedded Tissues. *J. Mol. Diagnostics* **14**, 22–29 (2012).

Chapter 5 - DNA-conjugated Gold Nanoparticles as High-Mass Probes in Imaging Mass Cytometry

(This chapter is adapted with permission from Brian Malile, Jelena Brkic, Alexandre Bouzekri, Derek J. Wilson, Olga Ornatsky, Chun Peng and Jennifer I. L. Chen. *ACS Appl. Bio Mater*. **2**, 4316–4323 (2019). Copyright 2019 American Chemical Society.)

(All experiments, data analysis, and manuscript preparation were performed by Brian Malile, with the exception of the initial IMC experiment related to the concentration-dependence study by Jelena Brkic. IMC data were acquired with the assistance of Dr. Alexandre Bouzekri, under the directorship of Dr. Olga Ornatsky at Fluidigm Inc. Funding was secured by Dr. Wilson, Dr. Peng and Dr. Chen)

5.1 Abstract

We employ Imaging Mass Cytometry™ (IMC™) to investigate *in vitro* uptake and cellular distribution of DNA-functionalized gold nanoparticles (AuNP). IMC enables the multiparametric imaging of cell components and allows for the detection of AuNP in cells with >100 times higher sensitivity than fluorescence imaging, as each nanoparticle contains thousands of atoms for signal amplification. Changes in the accumulation of nanoparticles in cells due to oligonucleotide sequence-dependent interactions are exploited to examine a model biomarker for hypoxia – microRNA-210. We find that AuNP functionalized with microRNA-210-targeting sequence accumulate in hypoxic cells 3 to 4-fold compared to normoxic cells. The work examines the potential use of DNA-AuNP as high-mass probes for the analysis of non-abundant nucleic acids.

5.2 Introduction

DNA-conjugated gold nanoparticles (DNA-AuNP) are widely explored for theranostic and imaging applications.[1] The sequence-specific interactions of DNA-AuNP with cellular species in particular have led to their use as antisense therapeutics[2] and imaging probes for biomarkers and metabolites *in vitro*.[3-6] To track their cellular uptake, optical microscopy based on fluorescence[7]

or darkfield scattering[8,9] is commonly employed. However, these techniques show limited sensitivity where high concentrations of nanoparticles are required or impose restriction on the size of the nanoparticles. Notably, the effect of binding of biomolecules to DNA-AuNP on subsequent intracellular trafficking and the fate of the nanoparticles is not well known. If such biomolecular interactions can change the trafficking or accumulation of nanoparticles in cells, they may present an alternative sensing mechanism for detecting biomarkers with DNA-AuNP.

A technique offering a much higher sensitivity than optical microscopy is Imaging Mass Cytometry™ (IMC™). IMC combines highly multiplexed immunohistochemistry with CyTOF® technology, which employs a time-of-flight mass cytometer and a scanning laser ablation source. In IMC, antibodies, DNA-intercalators, and other probes are functionalized with high-mass tags from the lanthanide series, with the possibility of analyzing up to 37 tags simultaneously.[10] The immobilized and labelled cells are ablated by a pulsed laser and the plume of sample fragments ionized by inductively coupled plasma is detected by the CyTOF® mass analyzer. The area of interest is scanned spot by spot with a resolution of 1 μm per pixel[10-12] to generate a full image of the mass tags in the cells or tissue. The technique overcomes the limitations of common optical imaging techniques such as immunohistochemistry and immunofluorescence, which suffer from narrow dynamic range for quantification and limited multi-parametric detection as a result of the spectral overlap of fluorophores.[13] IMC has been shown to be invaluable for mapping intracellular environments as well as heterogeneity of tissues and tumors,[11] and it is poised to facilitate the diagnosis and prevention of diseases.

On the other hand, challenges exist in employing IMC for the detection of low-abundant species in cells where the signal of targets tagged by a few hundred transition-metal atoms may be insufficient for detection. Nanoparticles, each comprising hundreds to tens of thousands of atoms,

can potentially amplify these mass signals dramatically. Previous work exploring polymer-labelled AuNP[14] and lanthanide nanoparticles[15] in mass cytometry demonstrated enhanced detection of low-abundant biomarkers such as CD14, CD3, and CD4. DNA-AuNP are potentially ideal ultrahigh-mass targets for IMC through the sequence-specific hybridization of the surface-anchored oligonucleotides with cellular nucleic acids. A class of low-abundant biomarkers recently discovered is microRNA (miRNA). miRNAs are short noncoding oligonucleotide sequences that regulate gene expression mainly by inducing the degradation of messenger RNAs (mRNA) and by inhibiting mRNA translation.[16] With diverse functions, microRNAs are involved in many biological processes and their aberrant expression is linked to disease.[17,18] Hypoxia, or the deficiency of oxygen in tissues, is a well-studied facet of the disease state that is involved in the development of many diseases, including preeclampsia.[19] A well-studied miRNA, miRNA-210, is the only miRNA consistently shown to be upregulated by hypoxia.[20] Although mRNAs can be readily tagged and corresponding IMC signals amplified using the cascade hybridization assay (RNAscope®),[21] such an approach cannot be applied to miRNAs because of their short length. Hence there is a need to develop probes and methodologies for IMC of low-abundant nucleic acids.

Herein we study the uptake and intracellular trafficking of DNA-AuNP using IMC and investigate the differences in the fate of the nanoparticles arising from the sequence-specific interactions with miRNA-210. We show that the multi-parametric imaging allows for the segmentation of cells and quantitative analysis of gold signals, which are found to be the highest in hypoxic cells incubated with miRNA-210-targeting DNA-AuNP. The findings pave the way to exploit DNA-AuNP as probes in IMC for the analysis of low-abundant nucleic acids.

5.3 Results and discussion

5.3.1 Uptake of AuNP and detection by IMC

DNA-AuNP of 15-nm in size were used for cell internalization studies. We constructed several different types of DNA-AuNP (Figure 5.1) to carry out comparative studies between IMC and confocal fluorescence microscopy.

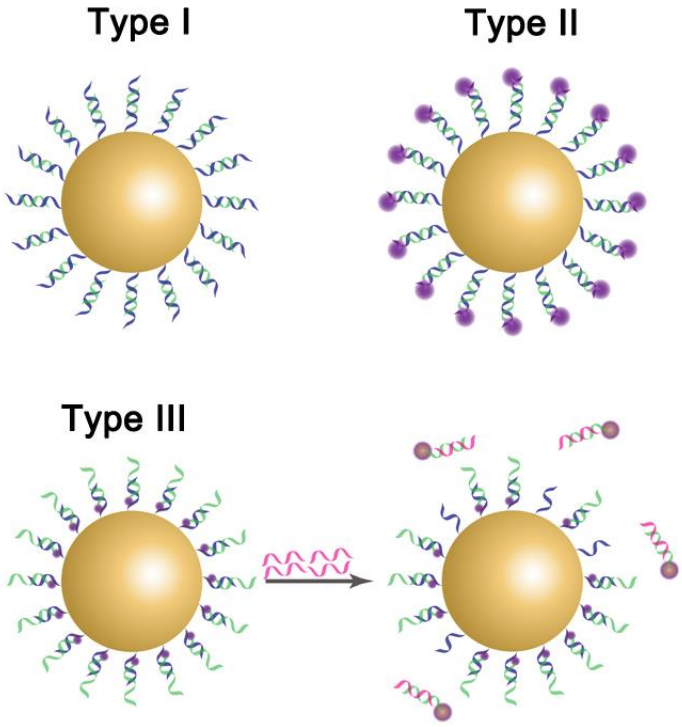

Figure 5.1. Different types of DNA-AuNP employed for IMC (Type I), fluorescence tracking (Type II) and Energy-Transfer-Based assay for miRNA-210 detection (Type III).

To gauge the sensitivity of IMC at ablating nanoparticles and detecting Au, cells were incubated with nanoparticles (Type I DNA-AuNP, Figure 5.1) at increasing concentrations of 0.001 nM, 0.01 nM and 0.1 nM and stained with an ^{191}Ir-labelled DNA-intercalator. IMC images in Figure 5.2 a-c show a clear consistent signal of the DNA-intercalator localized to the nucleus (blue). The Au signals (Figure 5.2 a-c, in red, and Figure 5.2 d-f shown alone for clarity) show an increase of signal with increasing concentration of AuNP. Furthermore, we observe that most of the gold

signals come from the perinuclear region, consistent with the endocytosis uptake pathway.[22] As the particles become internalized in the cytoplasm, they traverse through early endosomes, to late endosomes and finally to lysosomes which are located close to the nucleus.[23,24]

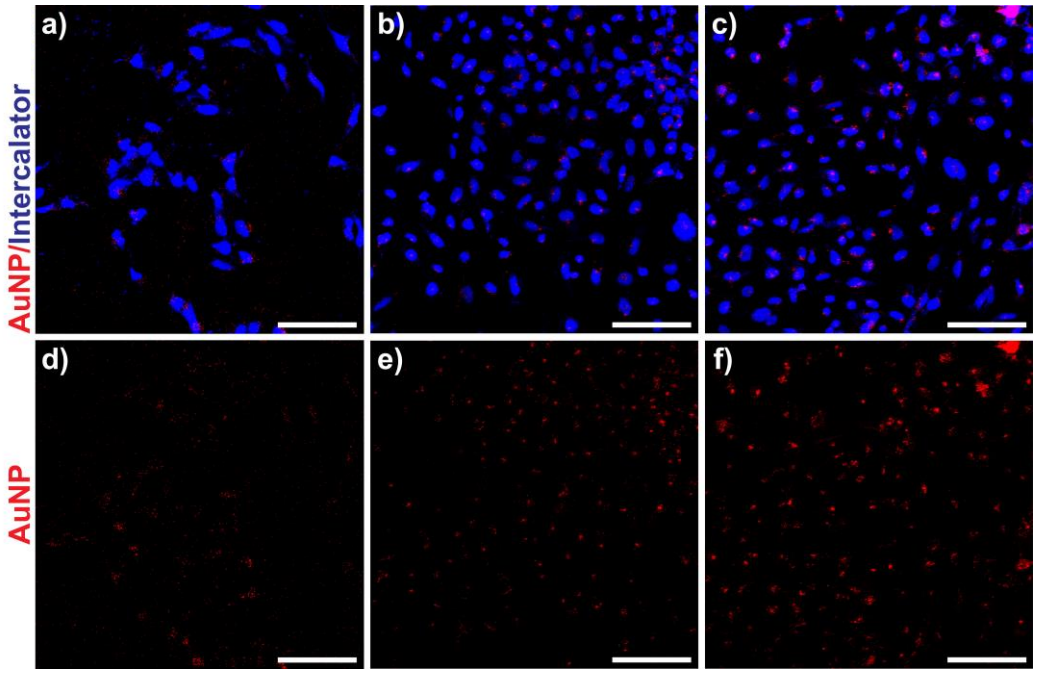

Figure 5.2. IMC images of cells incubated with increasing concentration of gold nanoparticles for 24 h: 0.001 nM (a, d); 0.01 nM (b, e); and 0.1 nM (c, f). Signals from ^{191}Ir-labelled DNA intercalator (blue) and ^{197}Au (red) are overlaid in a-c, and signals from Au alone are shown in d-f for clarity. Scale bar: 100 μm.

Notably, IMC can detect the presence of Au inside cells after incubation with as low as 0.001 nM AuNP (Figure 5.2d), a concentration that is 1000-fold lower than what can be observed via fluorophore-tagged AuNP. Increasing the concentration of AuNP to 0.01 nM (Fig. 5.2e) leads to intense ^{197}Au signals localized at the perinuclear region, consistent with previous reports.[23,25] For comparison, Figure 5.3 shows the optical mapping of the AuNP using fluorophore-tagged DNA on nanoparticles (Type II DNA-AuNP, Figure 5.1, denoted as Cy5-DNA-AuNP), where a discernible signal can be observed only at a concentration of >1 nM AuNP.

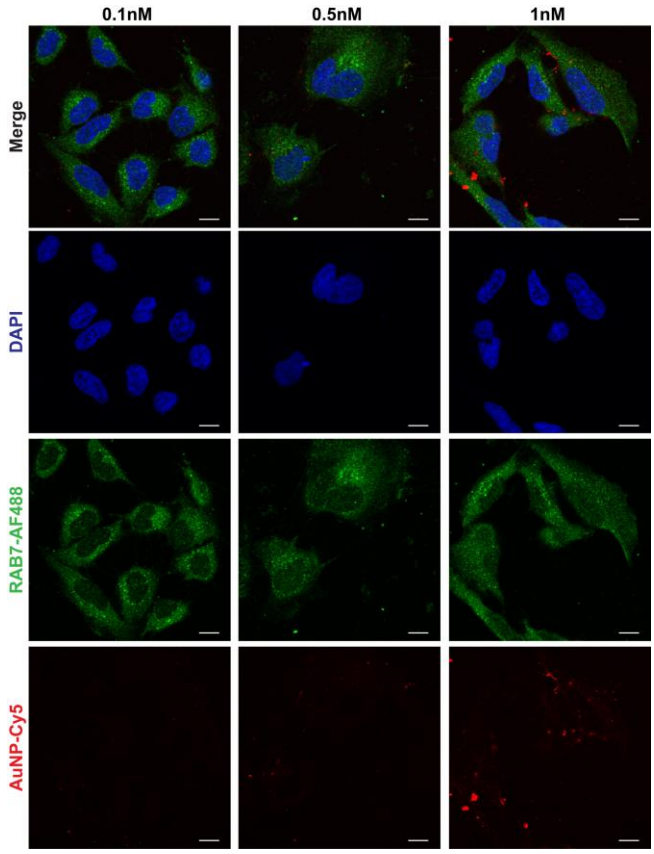

Figure 5.3. Fluorophore-tagged AuNP (red) with increasing concentrations in cells media. Fluorescence signal is observed at nanoparticle concentration of 1 nM. Little to no signal was observed at 0.1 and 0.5 nM of AuNP in growth media. Nuclei and late endosomes are shown in blue and green, respectively. Scale bar: 10 µm. Arrangement of oligonucleotides on the AuNP is depicted in Figure 5.1, Type II.

Because IMC is a destructive technique and lacks vertical resolution, we used confocal fluorescence microscopy to confirm the internalization of the AuNP. Figure 5.4 shows the Z-stack fluorescent images of Cy5-DNA-AuNP, nuclei and lysosomes. Images obtained in the Z-stack mode with the confocal microscope depict the tags, specifically the AuNP-Cy5 (red) in the same plane as the cell. Conversely, images representing the confocal planes above and below the cells show a decreased intensity of the tags ruling out the possibility of the AuNP-Cy5 being sedimented on top of the cells.

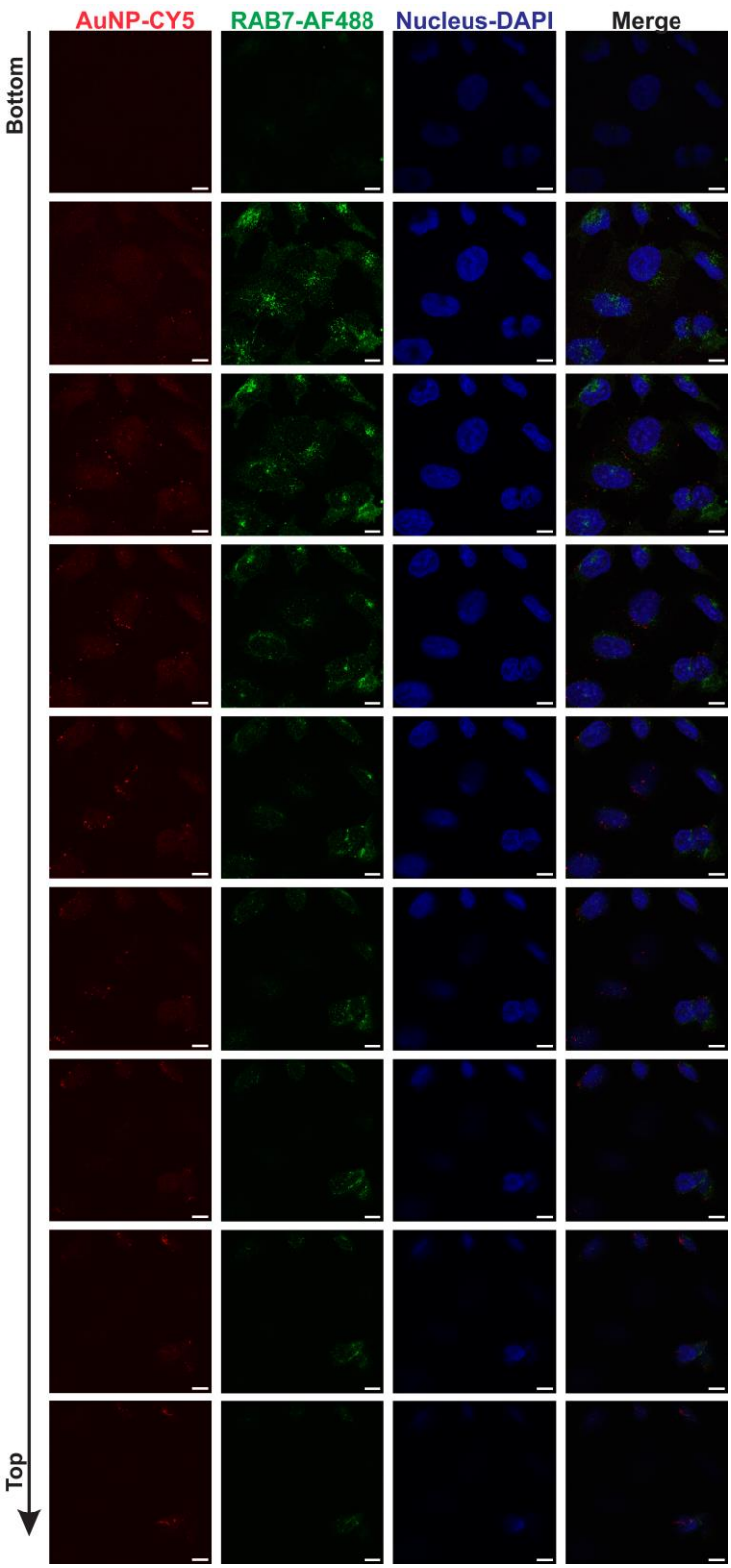

Figure 5.4. Z-stack confocal microscopy images of cells incubated with 1 nM of Cy5-tagged AuNP: Signals of Cy5 displayed in red, late endosome in green, and DAPI in blue. The vertical distance between confocal planes is 1 µm. Scale bar: 10 µm.

5.3.2 Multiparametric imaging

Next, we exploit the multiparametric capability of IMC by incorporating five labels. The absence of spectral overlap in mass tags provides a clear view of the cellular components. Figure 5.5a shows a merged image of five labels. Figure 5.5 b-f shows the individual channels of the tagged biomolecules: The pankeratin marker (Figure 5.5c) and iridium DNA-intercalator (Figure 5.5e) are used to determine the cytoplasm and cell nuclei; Ki-67 (Figure 5.5f) is used for identifying proliferating cells; other cell components, such as late endosome (Figure 5.5d) and lysosome, can be tagged with labelled antibodies/antigens. Conjugated gold nanoparticles (Figure 5.5b) are the species of interest. The combination of labels allows for downstream analysis, identification, and segmentation of cells to their components.

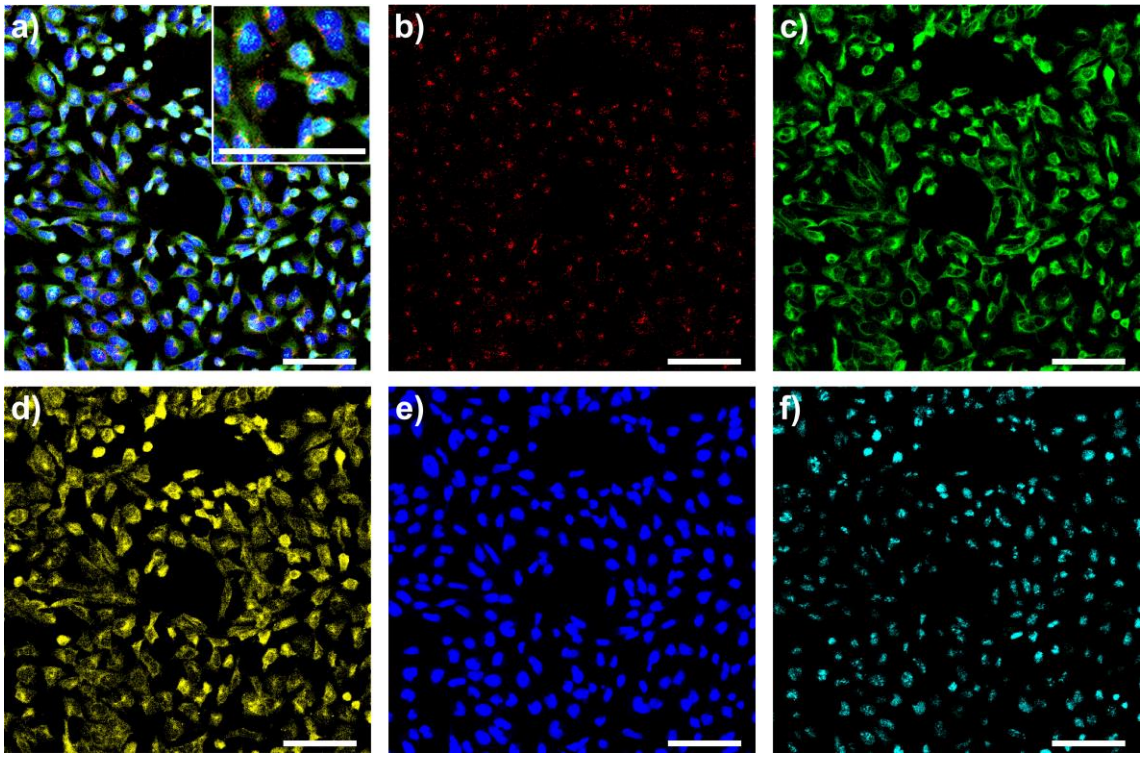

Figure 5.5. Multiparametric imaging with IMC: merged image of all signals (a); images of AuNP(^{197}Au) (b), pankeratin-^{162}Dy (c), late endosome (Rab7-^{165}Ho) (d), DNA (Intercalator-^{191}Ir) (e), and Ki-67-^{168}Er (f). Scale bar: 100 µm.

5.3.2.1 Sequence-specific uptake and trafficking of DNA-AuNP

We investigate the role of the oligonucleotide sequence in the cellular uptake and trafficking of the nanoparticles using IMC. Previous work has shown that the uptake of DNA-AuNP depends on several factors including the conformation of the conjugated oligonucleotides, the nature of the DNA (single- vs double-stranded),[24] and the surface charge of the nanoparticles.[27,28] Nanoparticles with single-stranded DNA were shown to be internalized more readily than nanoparticles with double-stranded DNA. However, dsDNA-AuNP are more resistant to nuclease activity[24,26] making them more stable and therefore we employed a short complement strand in the DNA-AuNP (Type I, Figure 5.1) for IMC. We examine two sequences conjugated on gold nanoparticles: (i) a probe sequence that is complementary to miRNA-210 (denoted as AuNP-Probe) and (ii) a nonbinding scrambled sequence that serves as a control (denoted as AuNP-Scramble). The short complement allows for the exposed nucleotides of the surface-bound oligonucleotides in AuNP-Probe to interact with miRNA-210 via strand-displacement. The conjugated nanoparticles were separately incubated with HTR-8/SVneo cells under normoxic or hypoxic conditions. Because of the aforementioned factors that can influence the uptake of DNA-AuNP, a direct comparison between different sequences may not necessarily reveal the influence of the sequence-specific interaction with the cellular nucleic acids. Hence, we examine the relative change in the uptake of AuNP-Scramble and AuNP-Probe under different conditions, instead of between sequences under the same condition.

The hypoxic condition was induced either directly by culturing in low oxygen (3%) or indirectly by the addition of $CoCl_2$. Cobalt binds to von Hippel-Lindau protein and stabilizes a transcription factor that is upregulated in low-oxygen conditions, Hypoxia Inducible Factor 2α,

thus mimicking hypoxia.[29] The cells were incubated with DNA-AuNP for at least 24 h, then fixed, labelled, and mapped using IMC. Figures 5.6a-d show DNA-intercalator and pankeratin stain in blue and green, depicting the nucleus and cytoplasm, respectively. The signals from gold nanoparticles are shown separately in Figures 5.6e-h (red),

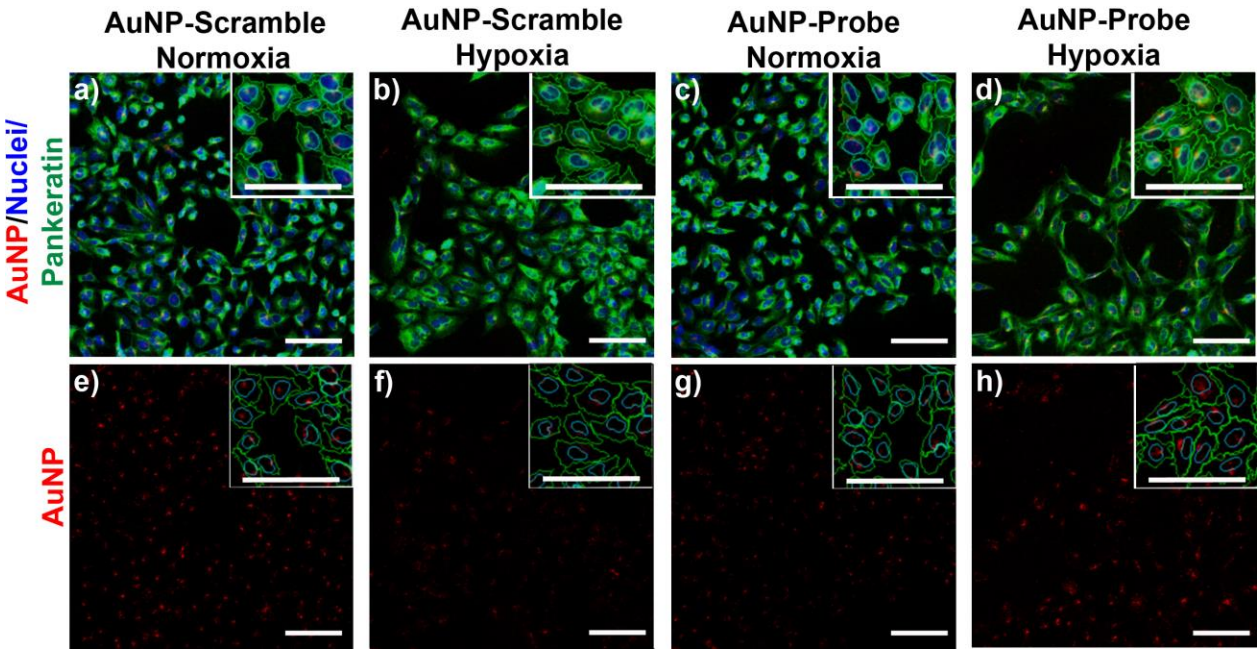

Figure 5.6. IMC images of cells incubated with AuNP-Probe or AuNP-Scramble under normoxic (a and c) and hypoxic (b and d) conditions: DNA (blue), pankeratin (green), and AuNP (red). Au signal (red) is shown in e-h. Inset depicts representative outlines of nuclei (light blue) and cells (green) from segmentation. Scale bar: 100 µm.

along with high magnification insets depicting outlines of cells and nuclei (obtained from pankeratin and DNA-intercalator stains) overlaid with the merged (Figure 5.6a-d) and Au (Figure 5.6e-h) signals. For quantitative analysis, Au signals were integrated across areas of whole cells and nuclei, while the cytoplasmic signals were obtained by taking the difference between the two. Figure 5.7 shows the box plots of integrated Au signals in whole cells (Figure 5.7a), cytoplasm (Figure 5.7b), and nuclei (Figure 5.7c) of the different samples. Cells incubated with AuNP-Scramble show a decrease in Au signal from normoxic to hypoxic condition (median of 4202 vs 2431 counts). In comparison, cells with AuNP-Probe exhibit an increase in Au signal from

normoxic to hypoxic condition (median of 1973 vs 5610 counts). The increase in Au signal from AuNP-Probe observed from normoxic to hypoxic condition is observed in all cellular compartments with the greatest difference (by 3.9-fold) found in the cytoplasm (Figure 5.7b). Additionally, we quantified the signals of other cellular markers in IMC. Figure 5.8 shows all the tags used to stain the cells under the four conditions. Quantification of these signals shows no correlation between normoxic and hypoxic conditions as well as AuNP-Scramble and AuNP-Probe (Figure 5.9). Therefore, we attribute the changes in Au signals to the sequence-specific interaction of oligonucleotides on the nanoparticle with cellular species, in this case miRNA-210.

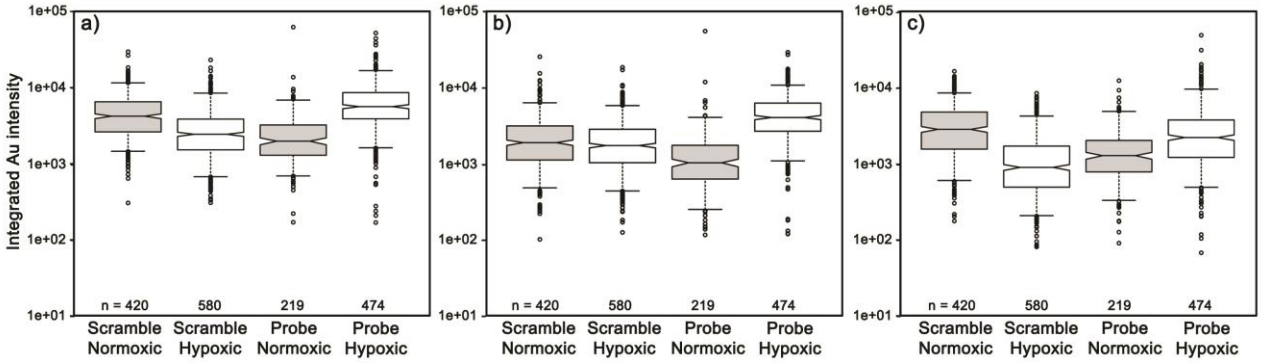

Figure 5.7. Quantification of ^{197}Au signals from cells incubated with AuNP-Scramble and AuNP-Probe under normoxic (grey) and hypoxic (white) conditions: Au signals in whole cells (a), cytoplasm (b), and nuclei (c). Hypoxia was induced by incubating cells at 3% oxygen.

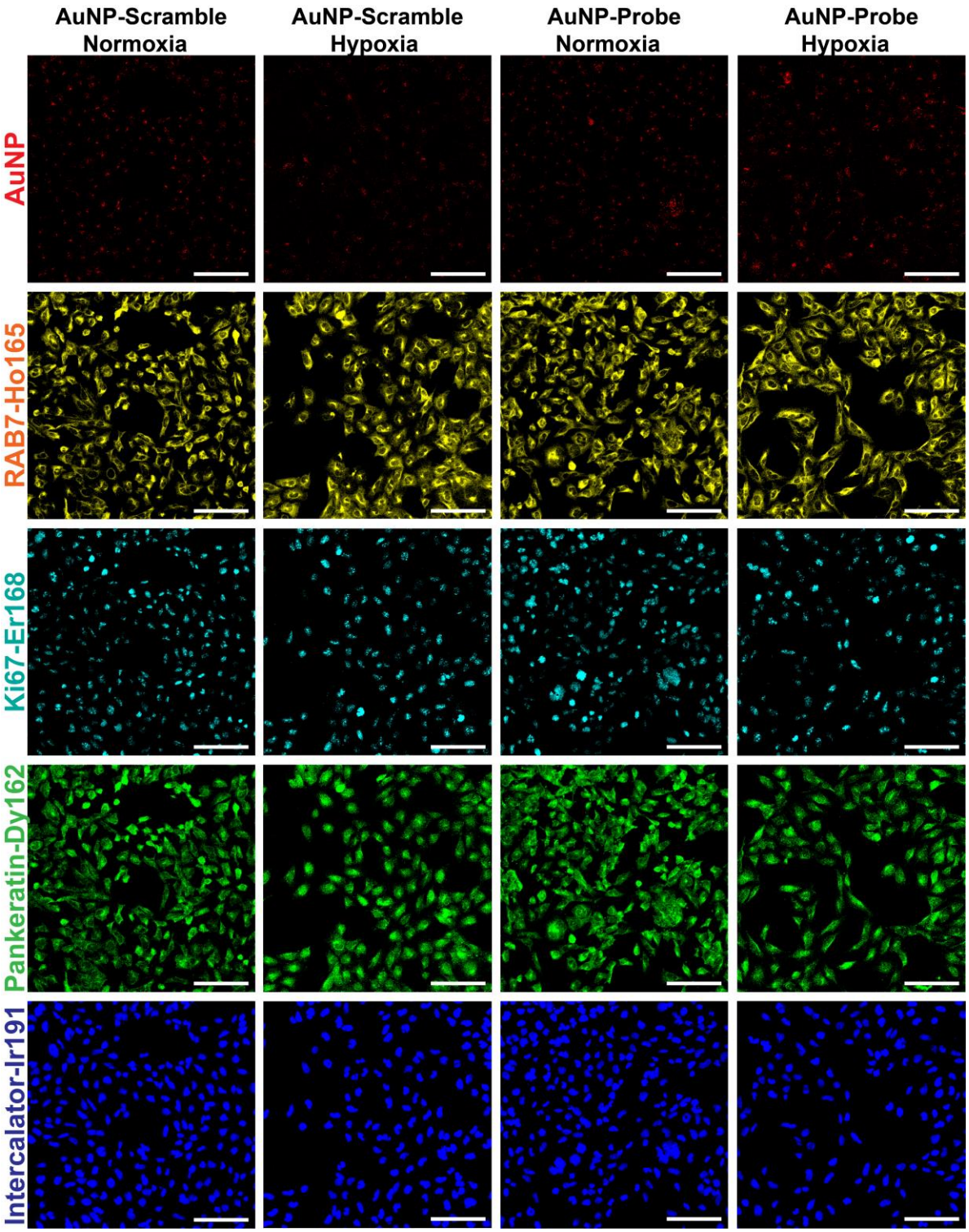

Figure 5.8. Representative images of all signals from IMC for samples with different conditions: signals of ^{197}Au in red, late endosome (Rab7-^{165}Ho) in yellow, Ki-67-^{168}Er in cyan, pankeratin-^{162}Dy in green, and DNA in blue. The cellular markers show negligible variations in intensity. Scale bar: 100 μm.

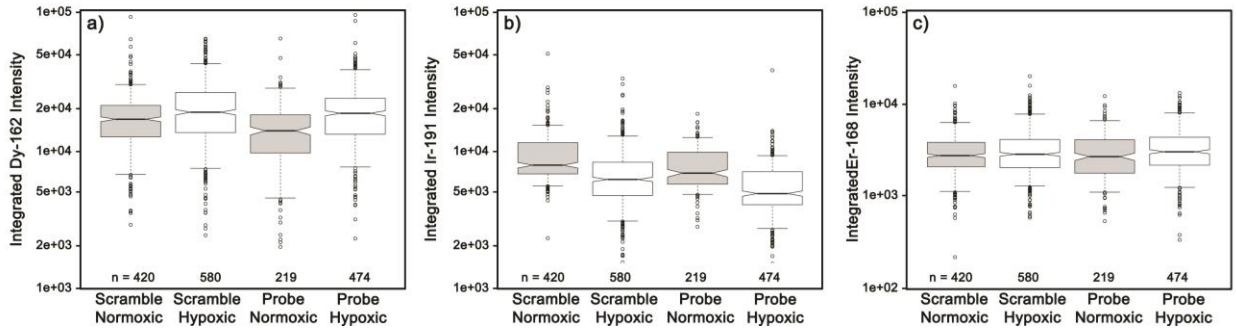

Figure 5.9. Analysis of IMC signals corresponding to other biomarkers: a) pankeratin, b) DNA, c) Ki-67.

Figures 5.10 and 5.11show additional IMC experiments between AuNP-Scramble and AuNP-Probe under normoxic vs hypoxic conditions, where the decrease in Au signal is consistently observed for AuNP-Scramble while an increase is observed for AuNP-Probe.

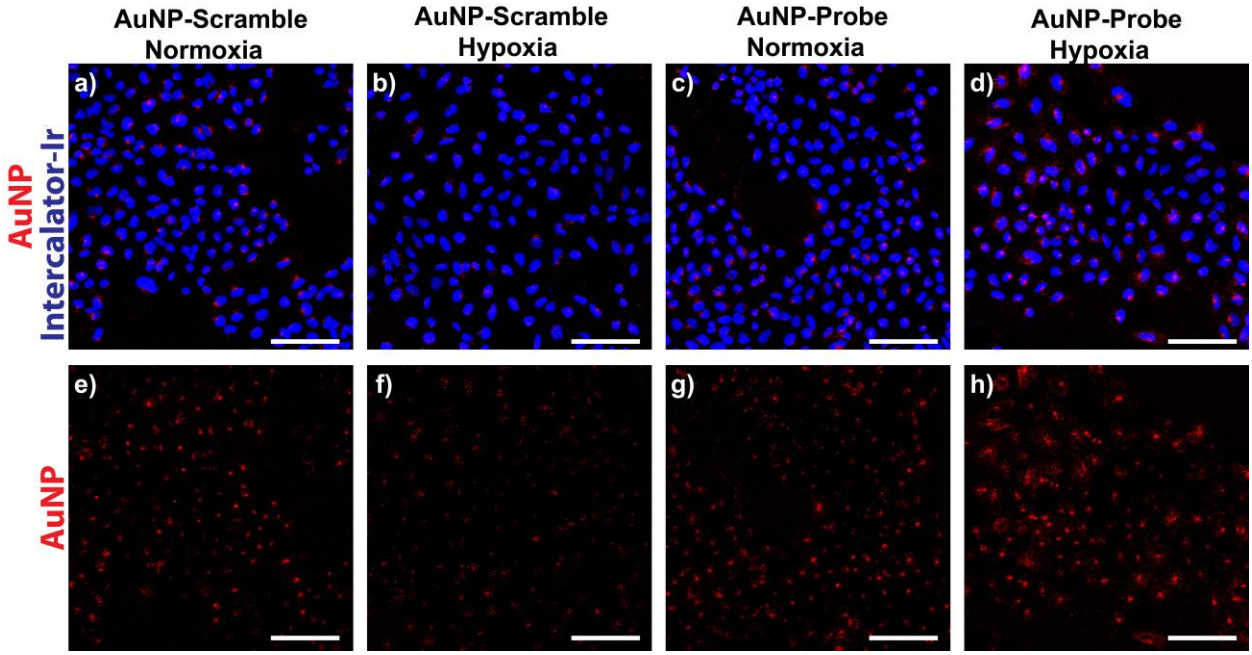

Figure 5.10. Additional IMC images of AuNP-Scramble (a and b) and AuNP-Probe (c and d) under normoxic and hypoxic conditions, respectively. Hypoxia was induced by incubating cells in growth media with 100 µM $CoCl_2$. Nuclei is shown in blue(Intercalator-^{191}Ir) and ^{197} Au signal in red. Images e–h show only the gold signals for clarity. Scale bar: 100 µm.

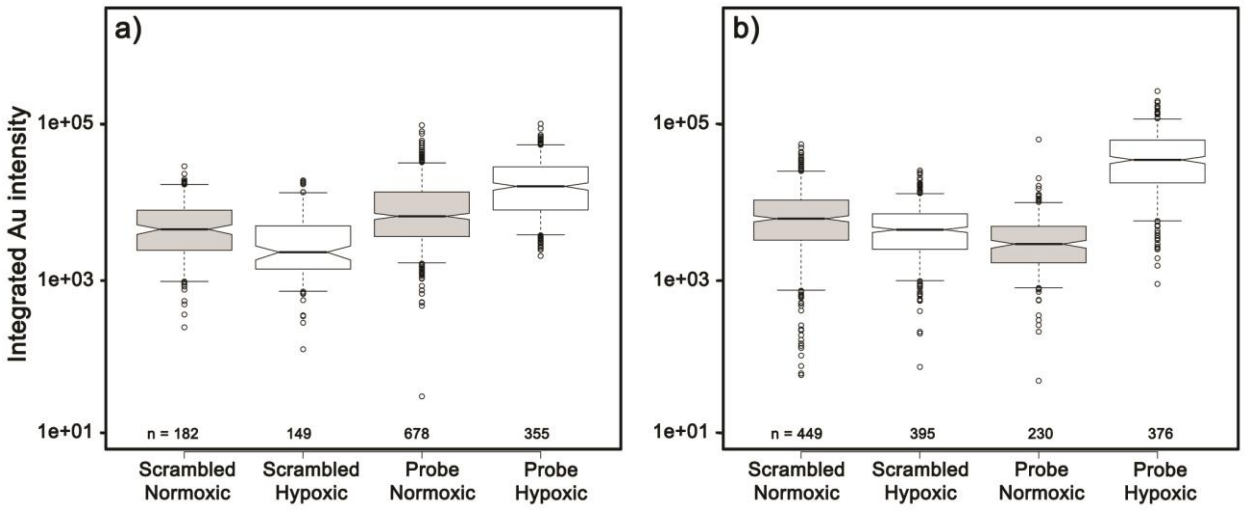

Figure 5.11. Additional IMC studies of cells incubated with AuNP-Scramble and AuNP-Probe under normoxic (grey) and hypoxic (white) conditions. ^{197}Au signals in cells are integrated and quantified. Hypoxia was induced by incubating cells in growth media with 100 μM $CoCl_2$.

We hypothesize that the greater accumulation of AuNP-Probe under hypoxic conditions may be attributed to the sequence-specific interaction with miRNA-210, which is elevated under hypoxia. Mature miRNAs function as part of a larger ribonucleoprotein complex, known as the RNA-induced silencing complex (RISC), where they provide transcript specificity. The binding of miRNA-210 and its associated RISC to the AuNP-Probe may alter the trafficking of the nanoparticles, leading to a greater retention inside cells, in particular in the cytoplasm where mature miRNA are processed and the majority of them carry out their function.[30-33] Previous work suggests that the exocytosis of nanoparticles can be affected by the surface charge, with cationic nanoparticles being retained in cells the longest compared to anionic or zwitterionic nanoparticles. The surface properties of the nanoparticles may be altered due to protein adsorption which in turn affects the exocytosis rate.[34] As a result, the association of related proteins to miRNA bound on the AuNP-Probe may lead to an overall greater accumulation of nanoparticles inside cells, before the nanoparticles are packaged up for excretion in lysosomes[23,24] as detected in the perinuclear region.

5.3.3 Comparative fluorescence study

In parallel we carried out a confocal fluorescence study to investigate how hypoxia affects the general uptake and retention rate of DNA-AuNP using AuNP functionalized with fluorophore-tagged non-interacting oligonucleotides (Type II DNA-AuNP, Figure 5.1). Figure 5.12 shows a decrease in the amount of AuNP in cells under hypoxia, in line with the decrease observed for AuNP-Scramble in IMC study.

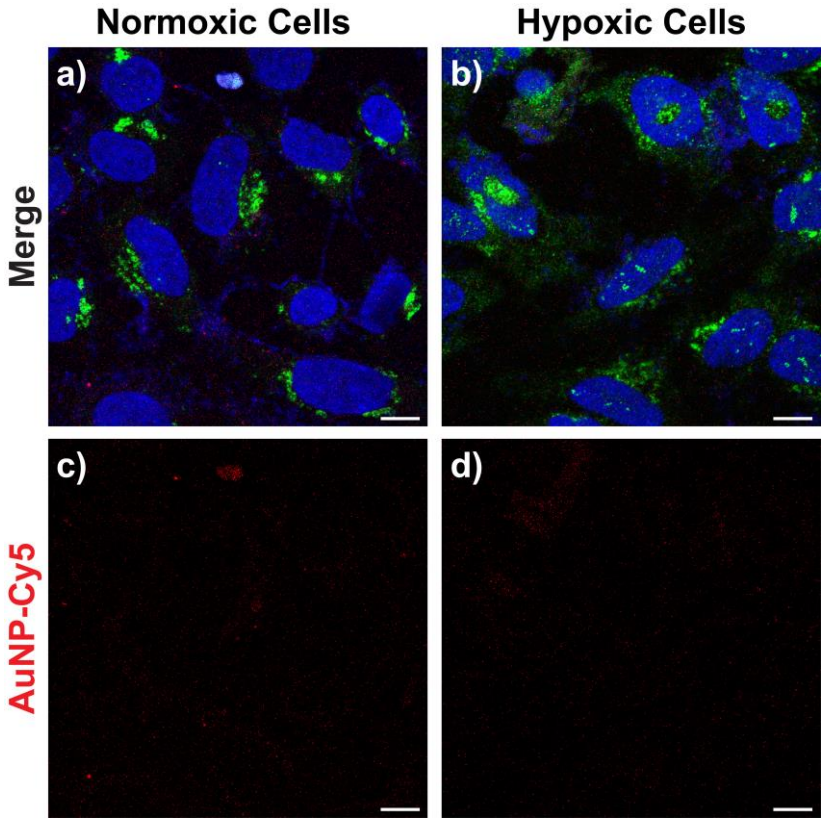

Figure 5.12. A comparison of nanoparticle (type II DNA-AuNP, Scheme 1) uptake in normoxia vs. hypoxia using confocal fluorescence microscopy. Panels a and b show merged signals of nuclei (blue), lysosome (green), and Cy5-DNA-AuNP (red). Panels c and d show Cy5 signal that reports the location of AuNP. Scale bar: 10 μm.

We confirm the upregulation of miRNA-210 in HTR-8/SVneo cells under hypoxic condition with qRT-PCR, and in single cells using energy-transfer-based nanoparticle assay. The qRT-PCR results show that miRNA-210 levels increase by 3-fold under hypoxic condition compared to normoxic condition (Figure 5.13).

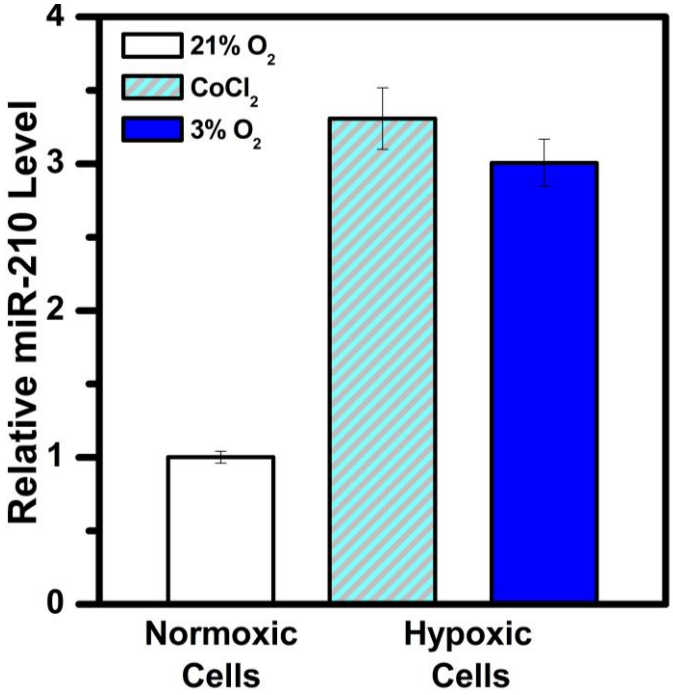

Figure 5.13. Relative miRNA-210 levels of cells under normoxic (white) and hypoxic conditions quantified by qRT-PCR. Hypoxia was induced by decreasing O_2 to 3% (blue) or adding $CoCl_2$ to growth media (striped). An upregulation of miRNA-210 of ~3-fold under hypoxia is observed compared to normoxia.

In the energy-transfer-based nanoparticle assay, cells were incubated with AuNP-Scramble-Cy3 and AuNP-Probe2-Cy3 (Type III DNA-AuNP, Figure 5.1), where the partial complement of the DNA-AuNP is fluorescently tagged. The orientation of the fluorescent tag is designed to be close to the surface of AuNP thereby quenching the fluorescence. Upon binding of the target, the partial complement with the fluorescent tag is displaced and fluorescence is restored. This approach has been widely explored for the detection of biomolecules such as mRNA and ATP.[3-5] Figure 5.14 shows the confocal fluorescence images and Cy3 signals of the different

samples. We observe that cells incubated with AuNP-Probe2-Cy3 display an increased signal from normoxic to hypoxic conditions.

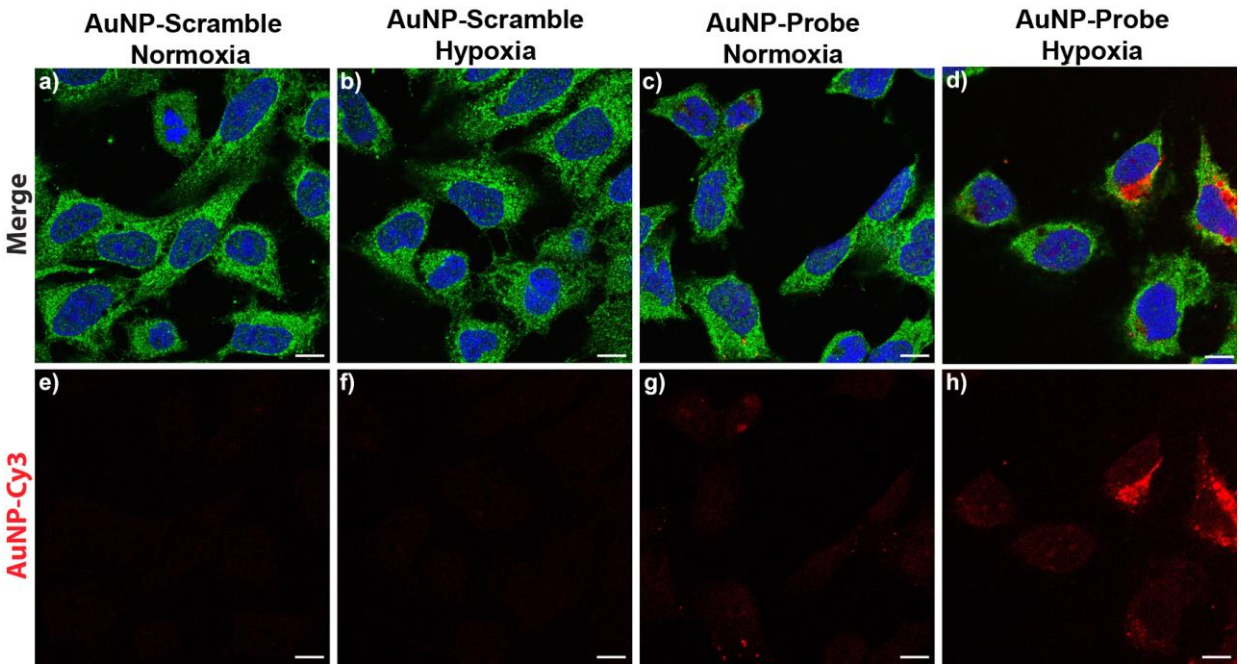

Figure 5.14. Energy-transfer-based nanoparticle assay for miRNA-210 analysis. Fluorescently-tagged AuNP-Scramble (a, b) and AuNP-Probe (c, d) were incubated with cells under normoxic and hypoxic conditions. Merged images showing nuclei (blue), lysosome (green) and AuNP-Cy3 (red, also shown separately in e-h). An increase in Cy3 signal is observed for cells with AuNP-Probe under hypoxia (3% O_2). Scale bar: 10 μm

In contrast, cells incubated with the nonbinding sequence (AuNP-Scramble-Cy3) show negligible difference in the fluorescence intensity. Quantification of the fluorescence signals segmented into the different cell compartments (Fig. 5.15) shows an increased signal in both the cytoplasmic and nuclear regions; however, it is most pronounced in the cytoplasm, in line with our IMC findings. Note that in the fluorescence study, the signal does not come from the gold nanoparticle but from the displaced Cy3-tagged strand unlike IMC that directly probes the location and existence of AuNP. Overall, the fluorescence study corroborates the 3-fold increase in miRNA-210 under hypoxia, in agreement with qRT-PCR results.

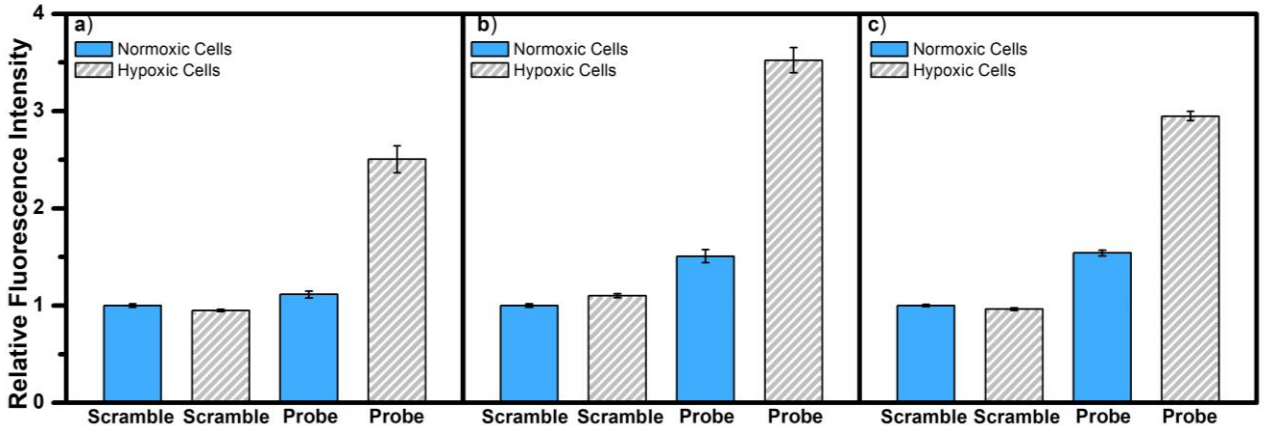

Figure 5.15. Probing miRNA-210 levels using energy-transfer-based nanoparticle assay. The fluorescent signals of AuNP-Scramble-Cy3 and AuNP-Probe2-Cy3 under normoxia (blue) and hypoxia (stripe) obtained from confocal microscopy: in cells (a), in cytoplasm (b), and from the nucleus region (c). The binding of miRNA-210 to AuNP-Probe2-Cy3 leads to the release of Cy3-labelled DNA and an increase of ~2.5–3-fold in fluorescence intensity in hypoxic cells.

5.4 Conclusions and outlook

In conclusion, we show that DNA-conjugated AuNP have the potential to be used as probes in IMC. With this method we achieved greater than 100-fold increase in sensitivity compared to conventional fluorescence-based techniques allowing us to utilize picomolars of nanoparticles, rather than nanomolars. An enhanced accumulation of nanoparticles under hypoxic condition was found for AuNP functionalized with miRNA-210-targeting sequence. This accumulation is more pronounced in the cytoplasm than the nucleus and is consistent with the upregulation of miRNA-210 under hypoxia as confirmed by qRT-PCR and the FRET-based nanoparticle assay. A potential challenge with using DNA-AuNP as probes in mass cytometry through endocytosis is that the uptake of nanoparticles may be variable and dependent on cell type, culturing condition, and microenvironment. Hence, factors influencing the rate of nanoparticle uptake and trafficking may confound the direct comparison of sequence-specific interactions. Further methodology

development will explore smaller DNA-AuNP for the direct staining of low-abundant nucleic acid biomarkers in fixed cells. Additionally, IMC is a qualitative technique thus its findings will always need to be supported with quantitative methods. With the flexibility in sequence design and materials compositional control, DNA-functionalized nanoparticles may be valuable high-mass probes in multiparametric IMC.

5.5 Methods

Reagents and materials

Gold nanoparticles (15 nm) were purchased from Ted Pella, Inc. Thiolated and fluorescently tagged oligonucleotides were purchased from IDT DNA Technologies. NAP-5 Columns were purchased from GE Healthcare Lifesciences. Ki-67-^{168}Er and Pankeratin-^{162}Dy, DNA Intercalator-^{191,193}Ir, and goat anti mouse-^{165}Ho, were obtained from Fluidigm. The 4-well chambered slides (Nunc™ Lab-Tek™ II CC2™) were purchased from ThermoFisher Scientific. Mouse monoclonal antibodies to Rab7117, rabbit monoclonal to Lamp1, and rabbit monoclonal antibodies to EEA1 were purchased from Cell Signalling Technology. All other chemicals were obtained from Sigma Aldrich.

Functionalization of gold nanoparticles

Thiolated DNA oligonucleotides were incubated with tris(2-carboxyethyl) phosphine hydrochloride for two hours at room temperature to reduce the disulfide bonds. The oligonucleotide mixture was then desalted using a NAP™-5 column, dried and isolated.

A volume of 300 µL of AuNP (2.5 nM) was incubated with 0.7 OD of oligonucleotides for 10 min. Sodium Dodecyl Sulfate (SDS) and Phosphate Buffer (PB) were added to a final concentration of 0.01 % and 1X PB (10 mM), respectively. After 20 min, volumes of 2 M NaCl in

0.01% SDS and 1X PB were added incrementally to increase the NaCl concentration of the DNA-AuNP solution to 0.4 M.[35] The mixture was vortexed, sonicated, and allowed to sit for 30 min between each addition. The DNA-AuNP were then incubated overnight at room temperature, and subsequently centrifuged and purified to remove excess DNA. The DNA-AuNP were resuspended in 0.01% SDS/0.05 M NaCl/0.01 M NaN_3 in 1X PB with sonication.

Depending on the study, different sequences were used in the functionalization, and the DNA-AuNP were hybridized with the corresponding complement.

DNA Sequences:

Type I - IMC Studies:
AuNP-Probe:
Seq. 1: 5′- HS - AAA AAT CAG CCG CTG TCA CAC GCA CAG -3′
Seq. 2: 5′- ACA GCG GCT GAT -3′

AuNP-Scramble:
Seq. 3a: 5′- HS - AAA AAA AAA AAT GCG ATG CGT T -3′
Seq. 4a: 5′- AAC GCA TCG CAT -3′-Cy3

Seq. 3b: 5′- HS - AAA AAT CAA CCT TGG TTA TAC GAT GAC -3′
Seq. 4b: 5′- ACC AAG GTT GAT -3′

Two sets of control sequences were used. The combination of Seq. 3b and 4b was designed to be similar in length and composition to AuNP-Probe. Seq. 3b was randomized to have no known homology to human RNA based on GenScript® Sequence Scramble.

Type II - Confocal Fluorescence Tracking:
Cy5-DNA-AuNP
Seq. 5: 5′ - HS - AAA AAA AAA AGA GCT GCA CGCT GCC GTC -3′
Seq. 6: Cy5 - 5′- GAC GGC AGC GTG CAG CTC -3′

Type III – Energy -Transfer-Based miRNA-210 Assay:
AuNP-Probe2-Cy3
Seq. 7: 5′ - HS - AAA AAA AAA A CTG TGC GTG TGA -3′
Seq. 8: 5′- TCA GCC GCT GTC ACA CGC ACA G -3′ -Cy3

Target
miRNA-210: 5′- CUG UGC GUG UGA CAG CGG CUG A -3′
Imaging Mass Cytometry Studies

Concentration dependence

An immortalized first-trimester trophoblast cell line, HTR-8/SVneo, was obtained from and cultured as previously reported.[36] Cells were seeded on a 4-well chambered slide at 7500 cells/chamber in 10% Fetal Bovine Serum (FBS)/RPMI and incubated for 24 hours at 37 ^{o}C under 5% CO_2 and 21% O_2. DNA-AuNP (functionalized with Seq. 1 and hybridized with Seq. 2) were added to three chambers at final concentrations of 0.001, 0.01, and 0.1 nM. After 24 h of incubation with the nanoparticles, cells were washed with 1X PB three times. The cells were then fixed with 400 μL of 4% formaldehyde/PBS (phosphate buffer saline) per chamber for 15 min, followed by permeabilization with ice-cold methanol for 30 min at room temperature. The cell antigens were blocked with 1% bovine serum albumin/PBS for 1 h and stained with monoclonal antibodies against cytoplasmic and nuclear compartments of adherent cells in 0.5% BSA/PBS overnight at 4 °C. The labelled monoclonal antibodies (Fluidigm) consist of Ki-67-^{168}Er (Clone Ki-67) and pankeratin-^{162}Dy (Clone C11). After overnight incubation, the cells were washed two times with PBS/triton 1% for 5 min each and three times with 1X PBS. Cells were stained with the DNA intercalator-^{191,193}Ir (Cell-ID™ Intercalator-Ir, Fluidigm) in PBS for 30 min, washed with PBS and deionized water, and air-dried. The slides were analyzed with the Hyperion™ Imaging System™, acquiring typically 2 images of each well at 500 μm x 500 μm per area. Data analysis was performed using MCD™ Viewer 1.0, CellProfiler™ 3.0 and Igor Pro. Boxplots were generated using BoxPlotR available at http://shiny.chemgrid.org/boxplotr/. Center lines show the medians; box limits indicate the 25th and 75th percentiles as determined by R software; whiskers extend to 5th and 95th percentiles; outliers are represented by dots; sample size (n = number of cells) is

noted. The notches are defined as ±1.58*IQR/sqrt(n) and represent the 95% confidence interval for each median. Non-overlapping notches give roughly 95% confidence that two medians differ.[37]

Comparison of uptake under normoxia vs hypoxia

AuNP-Probe (Seq. 1 and Seq. 2) and AuNP-Scrambled (Seq. 3a and Seq. 4a, or Seq. 3b and Seq. 4b) were separately added to cells cultured on the chamber slide. A final concentration of 0.01 nM of NP in cell media was used. The cells were cultured under normoxic condition (21% O_2) or hypoxic condition (3% O_2) for 24 h. Alternatively, the method of $CoCl_2$ addition was used to induce hypoxia in which cells were first incubated for 24 h with AuNP, followed by additional 24 h in growth media with 100 µM $CoCl_2$. The cells were incubated at 37 °C in 5% CO_2 and 21% O_2. Samples were fixed, blocked, and stained. Anti-Rab7 mouse primary antibody with a secondary goat anti mouse-^{165}Ho were used for imaging late endosomes, followed by Ki-67-^{168}Er, pankeratin-^{162} Dy and DNA Intercalator-^{191,193}Ir to avoid any crosslinking with the antibodies.

Confocal microscopy

Tracking cellular uptake

Nanoparticles functionalized with Seq. 5 and hybridized with Seq. 6 (denoted as Cy5-DNA-AuNP) were used to track the cellular uptake. They were added to the growth medium at specified final concentrations (or 1 nM). After incubating for 24 h, the growth medium with excess DNA-AuNP was removed and cells were washed three times with 1X PBS, followed by 30-min treatment with ice-cold DAPI in methanol for fixing. Cell antigens were blocked with 1% bovine serum albumin/PBS for 1 h, then incubated for an additional 24 h with Rabit-Anti-Lamp1 primary antibody for lysosome detection, or with mouse anti-RAB7 for late endosome detection. Cells were then washed three times with 1X PBS after 24 h and incubated with secondary goat anti-

rabbit tagged with Alexa Fluor 488 for 60 mins at room temperature. The cells were washed and imaged with a Zeiss LSM 700 laser scanning microscope.

Energy-transfer-based nanoparticle assay

AuNP-Probe2-Cy3 (Seq. 7 and Seq. 8 tagged with Cy3) and AuNP-Scrambled (Seq. 3a and Seq. 4a tagged with Cy3) were separately added to cells cultured on the chamber slide at a final nanoparticle concentration of 1 nM. The cells were either grown at normoxic (21 % O_2) or hypoxic (3% O_2) condition for 24 h. The staining and washing procedures were identical to the previous confocal procedure.

Quantification of miRNA-210 by qRT-PCR

Total RNA was extracted using TRIzol™ reagent (Invitrogen™) as previously reported.[38,39] The miRNA-210 levels in cells were measured using TaqMan® PCR kit (ThermoFisher Scientific) and normalized to U6 snRNA. Relative quantification of miRNAs was calculated using the $2^{-\Delta\Delta ct}$ method.

5.6 References

1 Giljohann, D. A. & Mirkin, C. A. Drivers of biodiagnostic development. *Nature* **462**, 461 (2009).

2 Patel, P. C., Giljohann, D. A., Seferos, D. S. & Mirkin, C. A. Peptide antisense nanoparticles. *Proc. Natl. Acad. Sci. U. S. A.* **105**, 17222-17226 (2008).

3 Seferos, D. S., Giljohann, D. A., Hill, H. D., Prigodich, A. E. & Mirkin, C. A. Nano-Flares: Probes for Transfection and mRNA Detection in Living Cells. *J. Am. Chem. Soc.* **129**, 15477-15479 (2007).

4 Zheng, D., Seferos, D. S., Giljohann, D. A., Patel, P. C. & Mirkin, C. A. Aptamer nano-flares for molecular detection in living cells. *Nano. Lett.* **9**, 3258-3261 (2009).

5 Prigodich, A. E. *et al.* Multiplexed nanoflares: mRNA detection in live cells. *Anal. Chem.* **84**, 2062-2066 (2012).

6 Halo, T. L. *et al.* NanoFlares for the detection, isolation, and culture of live tumor cells from human blood. *Proc. Natl. Acad. Sci. U. S. A.* **111**, 17104-17109 (2014).

7 Wu, X. A., Choi, C. H. J., Zhang, C., Hao, L. & Mirkin, C. A. Intracellular Fate of Spherical Nucleic Acid Nanoparticle Conjugates. *J. Am. Chem. Soc.* **136**, 7726-7733 (2014).

8 Liu, M. *et al.* Real-time visualization of clustering and intracellular transport of gold nanoparticles by correlative imaging. *Nat. Commun.* **8**, 15646 (2017).

9 Wang, S.-H., Lee, C.-W., Chiou, A. & Wei, P.-K. Size-dependent endocytosis of gold nanoparticles studied by three-dimensional mapping of plasmonic scattering images. *J. Nanobiotechnol.* **8**, 33 (2010).

10 Qing, C. *et al.* Imaging Mass Cytometry. *Cytometry Part A* **91**, 160-169 (2017).

11 Chang, Q. *et al.* Biodistribution of cisplatin revealed by imaging mass cytometry identifies extensive collagen binding in tumor and normal tissues. *Scientific Reports* **6**, 36641 (2016).

12 Ornatsky, O. *et al.* Imaging mass cytometry - elemental immunohistochemistry for multiparametric imaging and quantitation. *J. Immunol.* **196**, 69.18-69.18 (2016).

13 Gitlin, L., Karelsky, S. & Andino, R. Short interfering RNA confers intracellular antiviral immunity in human cells. *Nature* **418**, 430 (2002).

14 Yang, Y.-S. S. *et al.* High-throughput quantitation of inorganic nanoparticle biodistribution at the single-cell level using mass cytometry. *Nat. Commun.* **8**, 14069-14069 (2017).

15 Pichaandi, J. *et al.* Lanthanide nanoparticles for high sensitivity multiparameter single cell analysis. *Chem. Sci.* **10**, 2965-2974 (2019).

16 Ke, H.-L. *et al.* Hypoxia-regulated MicroRNA-210 Overexpression is Associated with Tumor Development and Progression in Upper Tract Urothelial Carcinoma. *Int. J. Med. Sci.* **14**, 578-584 (2017).

17 Agarwal, V., Bell, G. W., Nam, J. W. & Bartel, D. P. Predicting effective microRNA target sites in mammalian mRNAs. *eLife* **4** (2015).

18 Baek, D. *et al.* The impact of microRNAs on protein output. *Nature* **455** (2008).

19 Shamshirsaz, A. A., Paidas, M. & Krikun, G. Preeclampsia, hypoxia, thrombosis, and inflammation. *J Pregnancy* **2012**, 374047-374047 (2012).

20 Luo, R. *et al.* Hypoxia-inducible miR-210 contributes to preeclampsia via targeting thrombospondin type I domain containing 7A. *Sci Rep* **6**, 19588-19588 (2016).

21 Wang, F. *et al.* RNAscope: A Novel in Situ RNA Analysis Platform for Formalin-Fixed, Paraffin-Embedded Tissues. *J. Mol. Diagn.* **14**, 22-29 (2012).

22 Zhang, S., Gao, H. & Bao, G. Physical Principles of Nanoparticle Cellular Endocytosis. *ACS Nano* **9**, 8655-8671 (2015).

23 Zhao, F. *et al.* Cellular Uptake, Intracellular Trafficking, and Cytotoxicity of Nanomaterials. *Small* **7**, 1322-1337 (2011).

24 Wong, A. C. & Wright, D. W. Cellular Uptake: Size-Dependent Cellular Uptake of DNA Functionalized Gold Nanoparticles (Small 40/2016). *Small* **12**, 5591-5591 (2016).

25 Zhu, Z.-J., Ghosh, P. S., Miranda, O. R., Vachet, R. W. & Rotello, V. M. Multiplexed screening of cellular uptake of gold nanoparticles using laser desorption/ionization mass spectrometry. *J. Am. Chem. Soc.* **130**, 14139-14143 (2008).

26 Giljohann, D. A. *et al.* Gold Nanoparticles for Biology and Medicine. *Angew. Chem. Int. Ed.* **49**, 3280-3294 (2010).

27 Chithrani, B. D., Ghazani, A. A. & Chan, W. C. W. Determining the Size and Shape Dependence of Gold Nanoparticle Uptake into Mammalian Cells. *Nano. Lett.* **6**, 662-668 (2006).

28 Jiang, W., Kim, B. Y. S., Rutka, J. T. & Chan, W. C. W. Nanoparticle-mediated cellular response is size-dependent. *Nat. Nanotechnol.* **3**, 145 (2008).

29 Yuan, Y., Hilliard, G., Ferguson, T. & Millhorn, D. E. Cobalt Inhibits the Interaction between Hypoxia-inducible Factor-α and von Hippel-Lindau Protein by Direct Binding to Hypoxia-inducible Factor-α. *J. Biol. Chem.* **278**, 15911-15916 (2003).

30 Schirle, N. T., Sheu-Gruttadauria, J. & MacRae, I. J. Structural basis for microRNA targeting. *Science* **346**, 608-613 (2014).

31 Schirle, N. T. & MacRae, I. J. The Crystal Structure of Human Argonaute2. *Science* **336**, 1037-1040 (2012).

32 Elkayam, E. *et al.* The Structure of Human Argonaute-2 in Complex with miR-20a. *Cell* **150**, 100-110 (2012).

33 Bartel, D. P. MicroRNAs: Genomics, Biogenesis, Mechanism, and Function. *Cell* **116**, 281-297 (2004).

34 Oh, N. & Park, J.-H. Surface Chemistry of Gold Nanoparticles Mediates Their Exocytosis in Macrophages. *ACS Nano* **8**, 6232-6241 (2014).

35 Hurst, S. J., Lytton-Jean, A. K. R. & Mirkin, C. A. Maximizing DNA loading on a range of gold nanoparticle sizes. *Anal. Chem.* **78**, 8313-8318 (2006).

36 Brkić, J. *et al.* MicroRNA-218-5p Promotes Endovascular Trophoblast Differentiation and Spiral Artery Remodeling. *Mol. Ther.* **26**, 2189-2205 (2018).

37 Spitzer, M., Wildenhain, J., Rappsilber, J. & Tyers, M. BoxPlotR: a web tool for generation of box plots. *Nat. Methods* **11**, 121 (2014).

38 Fu, G. *et al.* MicroRNA-376c impairs transforming growth factor-beta and nodal signaling to promote trophoblast cell proliferation and invasion. *Hypertension* **61**, 864-872 (2013).

39 Ye, G. *et al.* MicroRNA 376c enhances ovarian cancer cell survival by targeting activin receptor-like kinase 7: implications for chemoresistance. *Journal of cell science* **124**, 359-368 (2011).

40. Arnett, L. P. et al. Biotinylated Lipid-Coated NaLnF4 Nanoparticles: Demonstrating the Use of Lanthanide Nanoparticle-Based Reporters in Suspension and Imaging Mass Cytometry. Langmuir 38, 2525–2537 (2022).

5.7 Appendix

List of biomarkers mentioned or used in Chapters 4 and 5:

1. **CD14 -** an important marker of immune cell activation and plays a critical role in the recognition and response to bacterial and fungal pathogens. Its expression can be used as a diagnostic tool for various diseases.
2. **CD3 and CD4 -** biomarkers of T lymphocytes, which play a critical role in the adaptive immune response.
3. **Rab7 -** a biomarker that regulates membrane trafficking and lysosomal degradation
4. **Pankeratin -** a marker of epithelial cells which comprises an array of keratins and is widely used in diagnostic applications
5. **Ki-67** –common biomarker for cancer diagnosis, as it can provide information on the growth rate of cancer cells.

Chapter 6 - Challenges and Outlook on the Application of DNA-AuNP in Imaging Mass Cytometry

6.1 Limitations of IMC

Although IMC allows for multiplexed imaging of specimens with μm resolution, and can tackle the heterogeneity of cancer cells and tissues, it has a number of disadvantages worthy of discussion. Instrumental constraints, such as cost, laser stability, signal quantification, data acquisition and processing times, hinder the broad implementation of IMC. Additionally, method-based drawbacks need to be considered when designing IMC protocols. Not only is IMC a destructive technique but it also has some of the shortcomings of immunofluorescence procedures including the availability and specificity of a variety of antibodies. Overcoming these obstacles will expand the utility of IMC and facilitate the discovery of new cytometry-based techniques.

Long acquisition times (~120 min/1 mm^2) make IMC unfeasible for analysis of large regions of interest (ROIs) not to mention a large number of sample slides. Also, the determination of ROIs in a specific slide lengthens the procedures. Tissue microarray cores (TMC), which are tube shaped sections of a tissue typically removed by a hollow needle, can be used to make smaller ROIs though with added cost.[1,2] The overall range and amount of metal-tagged antibodies for labeling slides also increases the cost.[3] Labelling large tissue sections on multiple slides while only imaging a limited number of ROIs decreases the efficiency of IMC and waste expensive antibodies. Being a destructive method, the once-analyzed ROIs can not be imaged again, however other regions in the slide are stable enough for storage and processing at later times. The aforementioned factors together with the price tag of the instrument make IMC a niche technique for multiparametric imaging.

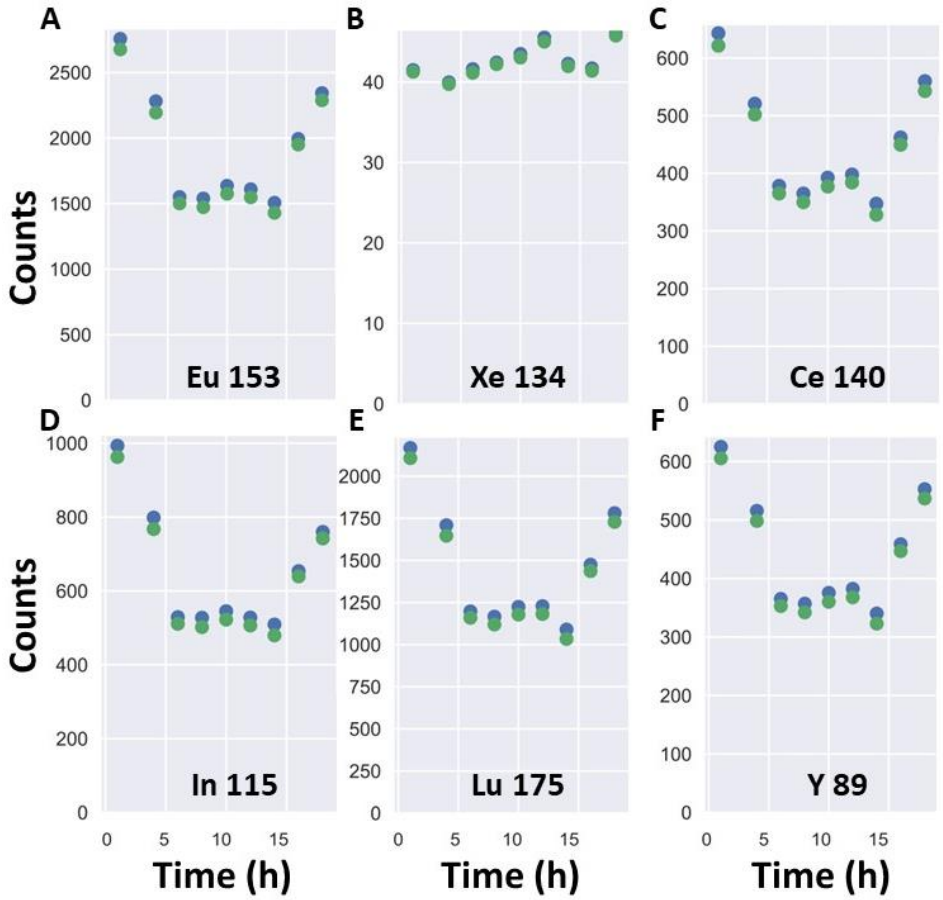

Figure 6.1. Signals from two laser-ablated spots (blue and green) in the calibration tape over the course of 20 hours for typical metals used in multiparametric screening in IMC.

While IMC is mainly used as a qualitative method, signal quantification is possible as shown in Chapter 5; however, the procedures are slow and lack robustness.[4] The implementation of a substrate (calibration tape) with known amounts of the metal isotopes as a reference is required. This method was employed in our work where the calibration tape was imaged prior to each ROI data acquisition to monitor the stability of the laser intensity over the long acquisition times.[2] Although it was observed that signal strength can be stable over the course of an experimental run (i.e. ~4-6 ROIs), the intensities between different runs can vary significantly. Hence it is desirable to establish a method of quantification by correlating and normalizing the signals from the calibration tape between different trials. On the other hand, the correlation of

signals from different isotopes with respect to laser intensity is not straight forward. Figure 6.1 shows an example of the various signals from the calibration tape over time. Alternatively, developing more stable high-power lasers may circumvent this limitation and enhance the quantification scope of IMC.

IMC has comparable constraints to fluorescence-based methods as they both rely on the same pool of antibodies. The availability and specificity of primary and secondary antibodies need to be considered before labeling highly multiplexed samples. An increased multiplexity means incubation with several antibodies, thus blocking steps during staining are crucial to prevent nonspecific interactions.[5] In Chapter 5, we showed how sequence-specific DNA-AuNP can be used for targeting nucleic acids. Conjugating gold nanoparticles with antibodies can potentially simplify staining procedures by removing the need for a secondary antibody for specific targets. Furthermore, aptamer-gold nanoparticle conjugates can add another dimension to targeting cellular components. Aptamers are short DNA sequences that have been selected to bind with high specificity and selectivity to a particular target which can be a small molecule, protein, or nucleic acid.[6] High affinity aptamers have been selected for proteins such as immunoglobulin E, thrombin, CD4 antigen, and vascular endothelial growth factor, to name a few.[7] Thus, implementation of DNA-AuNP and aptamer-AuNP in IMC methods, can alleviate the complications arising from an excess number of antibodies in multiparametric staining procedures. Although IMC is exploited for cancer research, addressing the high costs by optimizing workflows, improving data processing and acquisition times, and diversifying staining protocols with DNA and aptamer-nanoparticle conjugates can facilitate its in routine settings.

6.2 Challenges and outlook of DNA-AuNP in imaging mass cytometry

An important challenge of using AuNPs as high-mass probes in IMC arises from the intricate pathways of their uptake and excretion. Although substantial studies on the endo- and exocytosis of DNA-AuNP exist, there is no unified viewpoint. This uncertainty on the uptake and excretion pathways can blur discussions specifically when considering the utilization of DNA-AuNP in the detection of low-abundant biomarkers in cells. Establishing a solid understanding of the cellular uptake and excretion of DNA-AuNPs will enhance their potential biological sensing applications.

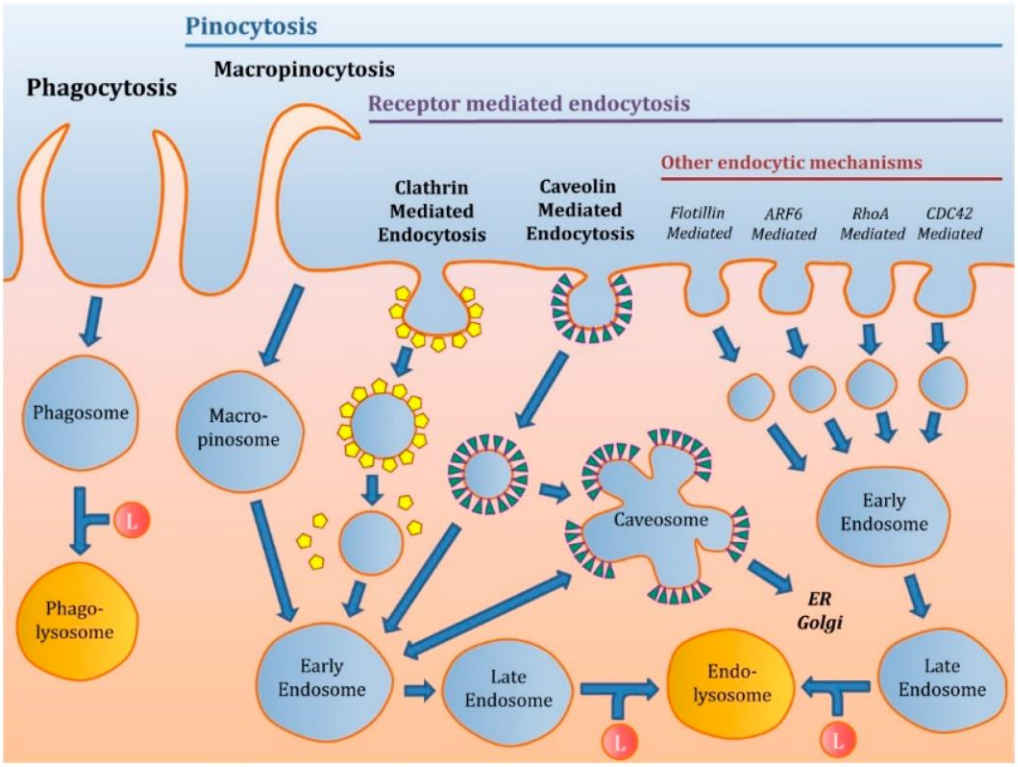

Figure 6.2. Various categories and subcategories endocytosis in cells. Reprinted with permission from reference 9.

Figure 6.2 depicts the complex nature of endocytosis by cells. Generally related or signalled by an immune response, phagocytosis describes the uptake of particulates in the micrometer range, and is not implicated in internalization of nanoparticles.[8] Conversely,

pinocytosis describe various internalization processes of particles much smaller than phagocytosis with clarithin mediated endocytosis (CME) being the most prevalent method for DNA-AuNP uptake.[9] However, size, shape, and surface charge need to be considered since they play a significant role in cell-nanoparticle interaction. While CME is the main uptake pathway for spherical DNA-AuNP, gold nanorods are internalized through micropinocytosis, which is the uptake of particles through large vacuoles.[10] Therefore for the successful implementation of AuNP as high mass probes in IMC, uptake mechanisms need to be systematically characterized for DNA, aptamer, and antibody conjugates. Not all cell lines internalize particles identically. Figure 6.3 depicts model cell lines used in research and their varying uptake mechanisms for surface functionalized gold nanorods. Human umbilical vein endothelial cells (HUVEC) and human monocyte-derived macrophages (HMDM) cells utilize caveolae mediated endocytosis and micropinocytosis respectively for the uptake of particles.[11] These cells do not distinguish between the various surface coatings of the nanorods. Conversely, the other two cell lines HeLa (cancer cells) and RAW cells (murine macrophages) employ all three pathways for internalization, with some degree of selection for the coatings of the nanorods. Therefore, uptake mechanisms for surface modified nanoparticles needs to be established for each cell line for the effective application of nanoparticles in imaging mass cytometry. Alternatively, as demonstrated in Chapter 5, careful controls using DNA-AuNP with non-targeting sequence but similar properties as the targeting DNA-AuNP are required for comparison. One way to bypass the complicated uptake pathways is by employing DNA-stabilized nanoclusters instead of the widely used 15-30 nm particles. Nanoclusters consist of 20-150 atoms and have unique optoelectronic properties.[12,13] Due to their small size (1-1.5 nm), they can permeate cell membrane after fixing thus be utilized similarly as labeled antibodies. While the extent utilization of DNA-AuNP in IMC is still in its

infancy, there is potential for broad applications because of their stability, low-cost, and tunability in surface modifications.

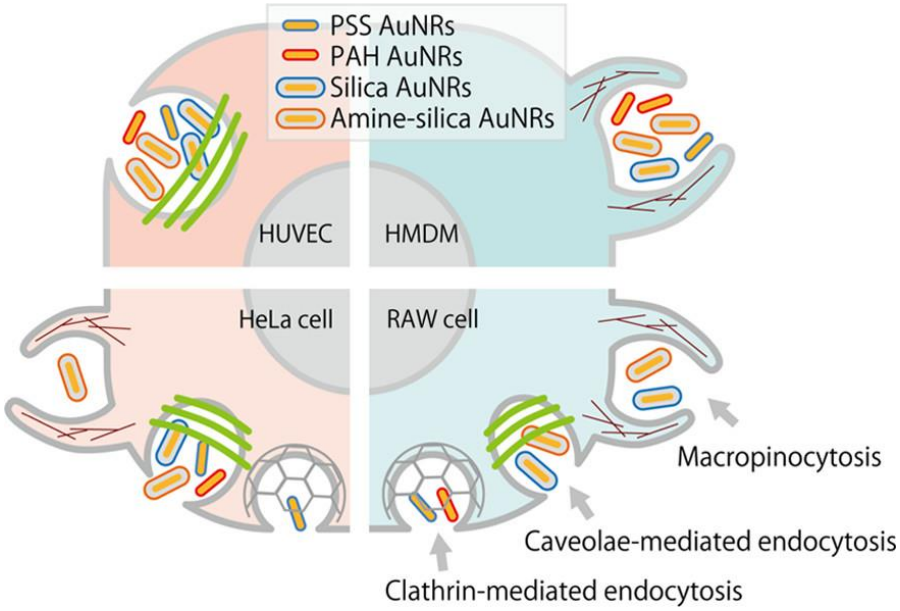

Figure 6.3. Internalization pathways of macrophage derived cells lines (blue) and human cell lines (red) for surface functionalized gold nanorods. Reprinted with permission from reference 11.

6.3 Future outlook

Similar to metal-tagged antibodies, various types of nanoparticles can be used in panels for multiparametric imaging. While gold nanoparticles are most used due to their stability and facile functionalization, other metals such as platinum, and silver can potentially be utilized as well. Reports of antibodies labeled Lanthanide, tantalum oxide nanoparticles, osmium-tagged polystyrene spheres show that high mass tags for imaging mass cytometry are rapidly developing.[14–16] Similar to panels of metal-tagged antibodies, panels of sequence-specific nanoparticles of various metals can diversify the toolbox specifically for investigating low-abundant nucleic acids simultaneously.

Nanomaterials that are detectable with multiple instruments can improve the efficiency and quality of experimental procedures. Cadmium based quantum dots, in addition to the photocatalytic capabilities discussed in Chapter 2, have absorption and emission spectra and are desirable materials for fluorescence methods. They have small sizes, that can permeate cell membranes prior to fixing, and can be functionalized with antibodies.[17] Therefore, they can be used as fluorescent tags and high mass probes simultaneously. The multifunctionality of QDs can be advantageous in samples where *in-vivo* fluorescence microscopy can be performed prior to fixing cells for IMC. In summary, conjugated nanomaterials that rival the antibodies in cost, performance, and stability can enhance the extent of implementation of IMC outside cancer research.

6.4 References

1. Eckel-Passow, J. E. *et al.* Tissue microarrays: one size does not fit all. *Diagn. Pathol.* **5**, 48 (2010).

2. Chang, Q. *et al.* Imaging Mass Cytometry. *Cytom. Part A* **91**, 160–169 (2017).

3. Schlecht, A. *et al.* Imaging mass cytometry for high-dimensional tissue profiling in the eye. *BMC Ophthalmol.* **21**, 338 (2021).

4. Chang, Q. *et al.* Biodistribution of cisplatin revealed by imaging mass cytometry identifies extensive collagen binding in tumor and normal tissues. *Sci. Rep.* **6**, 1–11 (2016).

5. Le Rochais, M., Hemon, P., Pers, J.-O. & Uguen, A. Application of High-Throughput Imaging Mass Cytometry Hyperion in Cancer Research . *Frontiers in Immunology* vol. 13 (2022).

6. Zheng, D., Seferos, D. S., Giljohann, D. A., Patel, P. C. & Mirkin, C. A. Aptamer nano-flares for molecular detection in living cells. *Nano Lett.* **9**, 3258–3261 (2009).

7. Song, K.-M., Lee, S. & Ban, C. Aptamers and Their Biological Applications. *Sensors* vol. 12 612–631 (2012).

8. Doherty, G. J. & McMahon, H. T. Mechanisms of Endocytosis. *Annu. Rev. Biochem.* **78**, 857–902 (2009).

9. Manzanares, D. & Ceña, V. Endocytosis: The Nanoparticle and Submicron Nanocompounds Gateway into the Cell. *Pharmaceutics* vol. 12 (2020).

10. Ding, L. *et al.* Size, Shape, and Protein Corona Determine Cellular Uptake and Removal Mechanisms of Gold Nanoparticles. *Small* **14**, 1801451 (2018).

11. Xiao, Y. *et al.* Effect of Surface Modifications on Cellular Uptake of Gold Nanorods in Human Primary Cells and Established Cell Lines. *ACS Omega* **5**, 32744–32752 (2020).

12. Copp, S. M. *et al.* Magic Numbers in DNA-Stabilized Fluorescent Silver Clusters Lead to Magic Colors. *J. Phys. Chem. Lett.* **5**, 959–963 (2014).

13. Tsunoyama, H. & Tsukuda, T. Magic Numbers of Gold Clusters Stabilized by PVP. *J. Am. Chem. Soc.* **131**, 18216–18217 (2009).

14. Arnett, L. P. *et al.* Biotinylated Lipid-Coated NaLnF4 Nanoparticles: Demonstrating the Use of Lanthanide Nanoparticle-Based Reporters in Suspension and Imaging Mass Cytometry. *Langmuir* **38**, 2525–2537 (2022).

15. Zhang, Y. *et al.* Tantalum Oxide Nanoparticle-Based Mass Tag for Mass Cytometry. *Anal. Chem.* **92**, 5741–5749 (2020).

16. Budzinski, L. *et al.* Osmium-Labeled Microspheres for Bead-Based Assays in Mass Cytometry. *J. Immunol.* **202**, 3103–3112 (2019).

17. Pathak, S., Davidson, M. C. & Silva, G. A. Characterization of the Functional Binding Properties of Antibody Conjugated Quantum Dots. *Nano Lett.* **7**, 1839–1845 (2007).

Epilogue

As shown in this dissertation, the underlying theme in nanomaterials research is that by shrinking a material to the nanoscale, new properties can be harvested in a range of applications. An in-depth investigation of their surface chemistry and physical and chemical properties shows the complexity and scope of nanomaterials research. Interestingly, one can interchange the two types of nanocrystals investigated - gold nanoparticles as photocatalysts, and quantum dots for imaging applications. Quantum dots may be used as high-mass probes in imaging mass cytometry where their small size can increase their internalization by cells; they can potentially be coated with oligonucleotides and probe nucleic acids in cells in a similar fashion to the DNA-gold nanoparticles. The different composition of QDs such as CdS, CdSe, CdTe, can serve as the signal for image generation, On the contrary, conjugation of the surface of gold nanoparticles with QDs may have synergistic effects where the metal surface catalyzes reactions with the hot electrons generated by the Mn-doped quantum dots. Overall, the field of nanomaterials research is the space where expertise from physics, chemistry, biology, medicine, and engineering converges and creates opportunities for highly diverse projects and applications.

List of Publications

PhD

1. **Brian Malile**., Rana Sodhi & Jennifer I.L Chen. Mn(II)-doped CdS/ZnS core/shell quantum dot film photocatalyzes reductive organic transformations with a boost in efficiency from enhanced Auger processes . *J. Mater. Chem. A* **(2022)** DOI:10.1039/D2TA06727G

2. Leigh R. Crilley, Andrea A. Angelucci, **Brian Malile**, Cora J. Young, Trevor C. Van den Boer and Jennifer I. L. Chen. "Non-woven materials for cloth-based face masks inserts: relationship between material properties and sub-micron aerosol filtration", *Environ. Sci. Nano* 8, 1603-1613 **(2021)**. DOI:10.1039/D1EN00277E

3. **Brian Malile**, Jelena Brkic, Alexandre Bouzekri, Derek J. Wilson, Olga Ornatsky, Chun Peng and Jennifer I. L. Chen. DNA-Conjugated Gold Nanoparticles as High-Mass Probes in Imaging Mass Cytometry, *ACS Appl. Bio Mater.* 2, 4316-4323 **(2019)**. DOI:10.1021/acsabm.9b00574

MSc

4. Lili Zhao, Julia Wiebe, Rabia Zahoor, Sladjana Slavkovic, **Brian Malile**, Philip E. Johnson and Jennifer I. L. Chen. Colorimetric detection of catalase and catalase-positive bacteria (E. coli) using silver nanoprisms. *Anal. Methods* **8**, 6625-6630 **(2016)**. DOI:10.1039/C6AY01453D

5. **Brian Malile** and Jennifer I. L. Chen. Factors influencing polyelectrolyte-aptamer multilayered films with target-controlled permeability for sensing applications. *Analyst* 141, pp 3794-3802. **(2016).** DOI:10.1039/C5AN02198G

BSc

6. **Brian Malile** and Jennifer I. L. Chen. Morphology-Based Plasmonic Nanoparticle Sensors: Controlling Etching Kinetics with Target-Responsive Permeability Gate. *J. Am. Chem. Soc.* 135, pp 16042-16045 **(2013)**. DOI:10.1021/ja4086269